Global and Multi-Input-Multi-Output (MIMO) Extensions of the Algorithm of Mode Isolation (AMI)

A Dissertation
Presented to
The Academic Faculty

by

Matthew S. Allen

In Partial Fulfillment
of the Requirements for the Degree
Doctor of Philosophy

George W. Woodruff School of Mechanical Engineering
Georgia Institute of Technology
April 2005

Global and Multi-Input-Multi-Output (MIMO) Extensions of the Algorithm of Mode Isolation (AMI)

Approved by:

Professor Jerry H. Ginsberg, Chair
(School of Mechanical Engineering)

Professor Laurence Jacobs
(School of Civil and Environmental Engineering)

Professor Aldo Ferri
(School of Mechanical Engineering)

Professor James Craig
(School of Aerospace Engineering)

Professor Nader Sadegh
(School of Mechanical Engineering)

Date Approved: April 13, 2005

ACKNOWLEDGEMENTS

I am deeply grateful for the many people who have supported me in this work. I would like to thank Dr. Jerry Ginsberg for the countless hours of support that he provided. I truly appreciate the insights and advice he gave regarding this research and my career in general. I would also like to thank Dr. Ferri for his support and help, as they have greatly enriched my work and my experience at Georgia Tech. I would also like to thank my thesis committee, Dr. Nader Sadegh, Dr. Laurence Jacobs, and Dr. James Craig.

I would also like to acknowledge and thank all of those who helped by providing data for validating the AMI algorithm: the Swiss Federal Laboratories for Materials Testing and Research and the Katholieke Universiteit Leuven for providing vibration data from the Z24 highway bridge, Chris Moloney (who is quite skilled with an impact hammer,) as well as Dathan Erdahl and Charles Ume for providing vibration data from microchips. I also want to thank Ben Wagner, Bassem Zaki, and the other members of my lab that have provided support. I am also grateful to the National Science Foundation, the George W. Woodruff School, and the Achievement Rewards for College Scientists foundation for the financial support that made this research possible.

I am also deeply grateful for my family, especially my wife Melissa who supported and encouraged me and has always been there for me when I have needed someone to talk to about what I was doing. Also my children, Andrew and Ivy, for helping to keep me sane. Finally, I would like to thank my Father in Heaven for the unique series of events which allowed me to come to Georgia Tech to pursue a doctorate degree, and for His help over the years.

TABLE OF CONTENTS

LIST OF TABLES

LIST OF FIGURES

SUMMARY

A wide range of dynamic systems can be approximated as linear and time invariant, for which a wealth of tools are available to characterize or modify their dynamic characteristics. Experimental modal analysis (EMA) is a procedure whereby the natural frequencies, damping ratios and mode shapes which parameterize vibratory, linear, time invariant systems are derived from experimentally measured response data. EMA is commonly applied in a multitude of applications, for example, to generate experimental models of dynamic systems, validate finite element models and to characterize dissipation in vibratory systems. Recent EMA has also been used to characterize damage or defects in a variety of systems.

The Algorithm of Mode Isolation (AMI), presented by Drexel and Ginsberg in 2001, employs a unique strategy for modal parameter estimation in which modes are sequentially identified and subtracted from a set of FRFs. Their natural frequencies, damping ratios and mode vectors are then refined through an iterative procedure. This contrasts conventional multi-degree-of-freedom (MDOF) identification algorithms, most of which attempt to identify all of the modes of a system simultaneously. This dissertation presents a hybrid multi-input-multi-output (MIMO) implementation of the algorithm of mode isolation that improves the performance of AMI for systems with very close or weakly excited modes. The algorithmic steps are amenable to semi-automatic identification, and many FRFs can be processed efficiently and without concern for ill-conditioning, even when many modes are identified. The performance of the algorithm is demonstrated on noise contaminated analytical response data from two systems having close modes, one of which has localized modes while the other has globally responsive modes. The results are compared with other popular algorithms. MIMO-AMI is also applied to experimentally obtained data from shaker excited tests of the Z24 highway bridge, demonstrating the algorithm's performance on a data set typical of many EMA applications. Considerations for determining the number of modes active in the frequency band of interest are addressed, and the results obtained are compared to those found by other groups of researchers.

CHAPTER I

INTRODUCTION

Dynamic system identification has found numerous applications in a wide range of fields in recent decades, with ever increasing interest fueled by the ready availability of powerful computers equipped with data acquisition hardware. Experimental Modal Analysis (EMA) is a specialization of system identification that seeks a vibratory model for the dynamic system under test. The vibratory characteristics of the system are described by modal parameters, i.e. a modal natural frequency, damping ratio, and mode shape. The objectives in experimental modal analysis differ from those in general system identification in that the goal is meaningful modes of vibration, rather than matching input and output data. EMA has a vital role in validating and tuning structural dynamic finite element models, especially in characterizing energy dissipation, which is generally difficult to estimate analytically. On the other hand, EMA can also be applied to obtain a purely experimental structural-dynamic model of a complex system. The effect of modifying the mass or stiffness of the structure can then be simulated [37], or the response of the system due to various applied forces studied. Recently, EMA has also been applied in novel applications, such as to detect damage in a wide variety of systems (see [23], [42], and [54] for example), or to obtain the elastic properties of composite materials [44]. As applications of EMA expand, the need for accurate algorithms capable of handling large data sets with low signal to noise ratios is apparent.

Algorithms for experimental modal analysis of linear dynamic systems can be categorized as to whether they use frequency or time domain data. Another categorization addresses the analytical representation of a response to which the measured data is fit. Single-degree-of-freedom (SDOF) techniques consider modes to act independently, whereas multiple-degree-of-freedom (MDOF) techniques allow for the modal contributions to overlap. A third descriptor pertains to the number of locations for excitation and response

measurement. Single input-single output (SISO) uses a single pair, while multiple input-single output (MISO) uses multiple excitations and measures response at one location. If the system is time-invariant, so that the principle of reciprocity applies, then single input-multiple output (SIMO) is equivalent to MISO. Multiple input-multiple output (MIMO) uses the data obtained from a multitude of excitations and response measurements. This thesis focuses on MIMO algorithms, which offer an important advantage in that they can deal with situations where two or more eigenvalues are very close or repeated. This will be explained and demonstrated throughout this thesis. Furthermore, for complex structures it may be difficult or impossible to find a single drive point that adequately excites all modes of interest. Collecting a MIMO data set can improve the chances that all modes in a frequency band of interest are adequately excited.

In the early days of experimental modal analysis (EMA), modal parameter estimation was typically performed using single-degree-of-freedom (SDOF) methods, such as peak-picking or circle-fitting. These methods consider the response in a narrow band of frequencies to be well approximated by a SDOF response. As a result, SDOF methods give accurate results, only when the data is not too noisy and the natural frequencies of the system under test are well separated. Another disadvantage is that these methods typically require significant user interaction and expertise, and some of them can be sensitive to noise. Furthermore, when modes with close natural frequencies are encountered the methods are inaccurate or fail. As a result, the modal analysis community has sought simultaneous, multi-degree of freedom (MDOF) approaches.

1.1 MDOF Modal Parameter Identification

A multitude of multiple-degree-of-freedom (MDOF) modal parameter identification algorithms have been presented in the past fifty years. Thousands of papers have been published on the subject of linear system identification. Many of the algorithms which have been most prolific in the modal analysis community are described in text books on experimental modal analysis by Ewins [24], Heylen *et al* [37], and Maia *et al* [47]. Allemang [2] showed that many of these can be described by a "matrix polynomial" model, wherein the response is

represented by a polynomial in the Laplace s variable or the discrete-time z variable whose coefficients are matrices. For example, the transfer function for a linear time invariant (LTI) system $H(s)$ can be expressed as the ratio of two polynomials in $s = i\omega$ as follows

$$H(s) = \frac{\sum_{k=1}^{n} \beta_k s^k}{\sum_{k=1}^{m} \alpha_k s^k} \tag{1}$$

where α_k and β_k are real constants. In this simple case the polynomial coefficients are scalars, whereas a SIMO or MIMO response can be represented using a polynomial with matrix coefficients. A similar relationship can be derived for the impulse response of an LTI system in terms of the z variable. One can use these mathematical representations to identify the parameters of a system by solving for the polynomial coefficients that minimize the error between the measured response and a response described by the matrix polynomial model. The modal parameters, the modal natural frequencies, damping ratios, and mode shapes, can then be determined from the polynomial coefficients. One reason for the prevalence of the matrix polynomial model for the response is that the equation becomes linear in the unknown polynomial coefficients if one clears the denominator. As a result, linear algebra can be used to solve for the parameters that best fit the response. One alternative is to find the system parameters using nonlinear optimization techniques, yet starting values are generally needed to initialize nonlinear optimization, and these methods tend to be much more computationally intense. Nevertheless, a number of nonlinear approaches have been investigated, for example, using artificial neural networks to identify the system parameters [62], yet these are not as widely used in identifying LTI systems as the linearized approaches.

Most of the parameter identification algorithms typically encountered in practice can be described by the matrix polynomial model. Table 1 lists the algorithms described by Allemang in [2], as well as some which were apparently omitted and some that have been developed recently. Those not included in [2] have been marked with an asterix, and some references are given. References for the remainder of the algorithms can be found in [2]. All of these methods identify a set of matrix polynomial coefficients using least squares. The

Table 1: Properties of some common identification algorithms, adapted from Allemang. *-Not included in Allemang. 1-The types of inputs allowed when using SSI-DATA are somewhat different than those used in the other algorithms.

Algorithm	**Domain**	**Class**	**I / O**	**Name**
LSCE / CEA	time	LS	SIMO	Least Squares Complex Exponential
PTD / PRCE	time	LS	MIMO	Polyreference Time Domain - Polyreference LSCE
ITD	time	LS	SIMO	Ibrahim Time Domain
MRITD	time	LS	MIMO	Multireference ITD
DSPI*	time	LS	MIMO	Direct System Parameter Identification [47]
ARMA / ARMAV*	time	LS	SIMO	Autoregressive Moving Average [47] [39]
ERA	time	Subspace	MIMO	Eigensystem Realization Algorithm
SSI-DATA*	time	Subspace	MIMO[1]	Stochastic Subspace Identification [77] [18] [57]
RFP / OP	frequency	LS	SIMO	Rational Fraction Polynomial / Orthogonal Polynomial
pRFP*	frequency	LS	MIMO	Polyreference RFP [74]
PFD / FDPI	frequency	LS	MIMO	Polyreference Frequency Domain / F.D. Direct System Parameter Ident.
SFD / MRFD	frequency	LS	MIMO	Simultaneous FD / Multireference F.D.
pLSCF / Polymax	frequency	LS	MIMO	polyreference Least Squares Complex F.D. [36] [56]
ERA-FD*	frequency	Subspace	MIMO	Eigensystem Realization Algorithm F.D. [47]
SSI-FD*	frequency	Subspace	MIMO	Stochastic Subspace Identification F.D. [76]

subspace methods differ somewhat in that they apply singular value decomposition to the data matrices before applying least squares to estimate the matrix polynomial coefficients. As a result of the singular value decomposition step, the subspace methods are generally considered to be more computationally intense than the least squares methods.

Both time and frequency domain algorithms have been included in Table 1. While data acquisitions systems usually measure the time response of a system, it is often the case that a large quantity of time data is condensed using spectral averaging to yield a relatively compact set of frequency response functions. As a result, frequency response functions are

generally considered as the primary data for modal parameter estimation. Most of the time domain methods listed in Table 1 process impulse response functions, which are typically found by applying an inverse fast Fourier transform to the frequency response functions. In general, the data can be transferred fairly easily between time and frequency domains, so one typically consider the merits of the identification algorithm to be more important than the domain to which it applies. However, there are important cases when one might be limited to only one domain, such as in stepped sine testing, or when the details of the signal processing are significant. Discussion of all of the relative merits of time and frequency domain algorithms is beyond the scope of this thesis.

Considering that all of these methods are based on a similar mathematical model, and that the method used to solve that mathematical model is quite similar, one might expect all of these algorithms to yield the same result. While this is sometimes the case when comparing many of these algorithms, it is important to note that changes in the details of the implementation can affect an algorithm's performance significantly. For example, the matrix polynomial model is typically ill conditioned in the frequency domain due to the inclusion of high powers of the Laplace variable in the polynomial (recall that $s = i\omega$.) As a result, the computational efficiency and performance of frequency domain algorithms can depend upon the strategy employed for overcoming this difficulty. The rational fraction polynomial (RFP) algorithm of the early 1980's used orthogonal polynomials to reduce ill conditioning. The LSCF algorithm, which has been acclaimed recently, offers greatly improved performance in many cases, due primarily to a different strategy for overcoming numerical ill conditioning. Hence, one cannot completely ignore the small differences between the algorithms. It is also worth noting that very many variations to each of these algorithms have been presented. For example, Pintelon *et al* present a survey of SISO frequency domain algorithms in [59], each of which uses the same matrix polynomial model as the RFP algorithm.

1.2 Stabilization Diagram Approach

Although a variety of MDOF algorithms are available, in practice all of these are typically applied in the same way. The common approach is to process all of the measured data to estimate the parameters of all of the modes in a frequency band of interest simultaneously. This approach ignores the frequency-domain decoupling of modes upon which legacy SDOF algorithms depended. Furthermore, the number of modes to be identified is not typically known a priori so one might not know how many modes to fit. In most cases non-physical or computational modes are identified together with the true modes of the system, so that even if the number of modes to be fit were known, a higher order fit is often needed to obtain good estimates of the parameters of the modes of interest. The common approach in such a situation is to apply the MDOF algorithm at a number of model orders, and then plot the resulting eigenvalues on a stabilization diagram. A stabilization diagram charts the eigenvalues as a function of the model order. Modes that have similar modal parameters over a range of model orders are assumed to be true modes, while the remaining modes are discarded. Figure 1 presents a sample stabilization diagram from Peeters and De Roeck [55] created from experimentally measured vibration data from an antennae. The Instrumental Variables algorithm was used to find the modal parameters of the system for model orders ranging from 0 to 60, following which the resulting natural frequencies (horizontal axis) were plotted versus model order (vertical axis). In order to simplify interpretation of the stabilization diagram, various symbols were used to convey how well each mode identified resembles the nearest mode found at the next lowest model order, as described in the figure caption. The diagram also includes two zoom views highlighting pairs of close modes.

One potential shortcoming of the stabilization diagram approach is that it might be difficult to discern computational modes from true modes on the stabilization diagram, as noted by Auweraer *et al* [75] and Doebling, Alvin and Peterson [19]. Van Der Auweraer *et al* [73] [75] and Peeters *et al* [56] found this to be one of the most important problems faced by test engineers, particularly when the data sets being analyzed were noisy or the systems heavily damped.

A number of researchers have attempted to simplify or automate the process of selecting

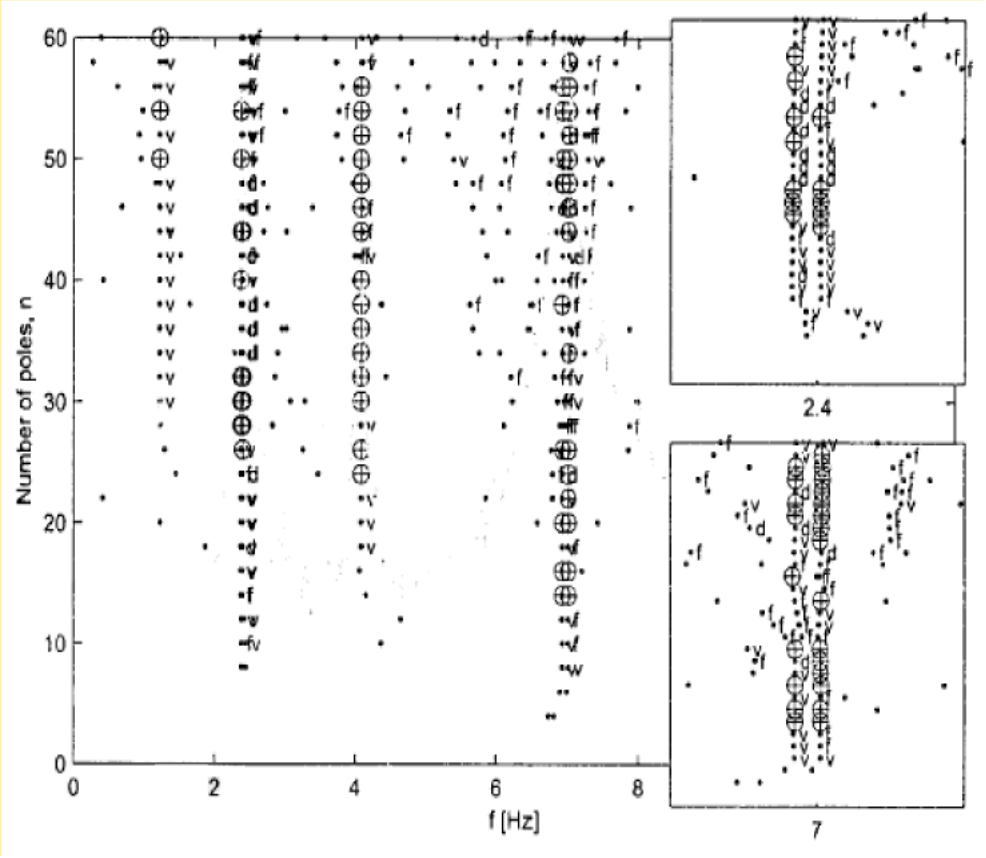

Figure 1: Sample Stabilization Diagram from Peeters and De Roeck generated using the Instrumental Variables algorithm. The symbols used are: '.' for a new pole; '.f' for a pole with stable frequency; '.d' for a pole with stable frequency and damping; '.v' for a pole with stable frequency and vector; '⊕' for a stable pole. Two zooms are included that concentrate on the close modes around 2.4 and 7 Hz.

the true system modes from a stabilization diagram. For example, Peeters and De Roeck [55] simplified the stabilization diagram in Figure 1 by marking modes for which the natural frequency, damping ratio, or mode vector were similar to the nearest mode at the next lowest model order. Verboven *et al* [78] [79] used a similar approach, employing fuzzy logic to automatically distinguish computational modes from true modes for an airplane slat track. Goethals and De Moor [33] found that energy could be used to distinguish many of the spurious modes. Researchers have also developed algorithms that tend to give stabilization diagrams that are easier to interpret. For example, the Stochastic Subspace Identification (SSI) [55] and the Least Squares Complex Frequency domain (LSCF) [15] [36] [56] [73] [75] algorithms have been shown to yield stabilization diagrams which are easier to interpret

than legacy algorithms, such as the Least Squares Complex Exponential (LSCE) or the Frequency-domain Direct Parameter Identification (FDPI) algorithms. The SSI and LSCF algorithms will be discussed further and applied to synthetic data in Chapter 3.

Another difficulty with a stabilization diagram approach is that there can be significant variation in the modal parameters estimated from one model order to the next, so that even when true modes can be identified on a stabilization diagram, it may be difficult to tell which model order results in accurate estimates of their modal parameters. Furthermore even if an algorithm yields modal parameters that are consistent from one model order to the next, it might be that there is a constant bias error relative to the true modal parameters. For example, the authors found this to occur when applying the SSI algorithm to noise contaminated analytical data in [4]. Considering that the eigenvalues and mode vectors of a structure generally change in proportion to the amount of damage present [38] [46], it is evident that accuracy is important to detect damage early in condition monitoring applications. High accuracy might also be needed in applications involving inverse methods, such as force identification, or in determining accurate material properties using EMA techniques. In view of all of these potential difficulties, one can see why Allemang said that, "The estimation of an appropriate model order is the most important problem encountered in modal parameter estimation." ([1] vibration course notes pg. 6-8)

1.3 The Algorithm of Mode Isolation

The Algorithm of Mode Isolation (AMI) offers an alternative to conventional MDOF methods in which the number of modes active in a given frequency band is determined together with the parameters of those modes. AMI begins by identifying modes one at a time, and then subtracting their contribution from the data. In this process the importance of each mode to the fit is clearly visible. The number of true modes in the data set is taken to be the number of modes that must be fit to the data to reduce it to noise. An iterative procedure then refines the initial estimate. The resulting MDOF fit does not introduce any spurious or computational modes.

This simple approach is numerically efficient, so many input and output sensors can be

processed simultaneously. Comparisons of AMI with other simultaneous MDOF algorithms [3], [4], [5], [6], such as the data-driven stochastic subspace algorithm (SSI), the poly-reference Least Squares Complex Frequency Domain (pLSCF) algorithm and the Rational Fraction Polynomial algorithm (RFP or Orthogonal Polynomial algorithm OP,) using noise-contaminated data have shown that AMI performs favorably. Because AMI is based on a pole-residue representation of the transfer function, there is no theoretical upper limit to the number of modes that can exist in the data set being processed. On the other hand, many frequency domain algorithms are based on a rational polynomial model that is ill conditioned at high model order.

The general concept of mode isolation was first suggested by Kirshenboim [41], and seems to have been implemented as part of the Modent package [68]. More recently, Joh and Lee [40] suggested a similar approach for identifying the parameters of rotordynamic systems. The first detailed investigation of the methodology was presented by Drexel and Ginsberg [21], in which it was dubbed the Mode Isolation Algorithm (MIA), and then subsequently the Algorithm of Mode Isolation (AMI). Recently, Yin and Duhamel [81] reported using a similar SISO technique, although they solved for the modal parameters using sets of two and three points around each resonance peak in order to match the number of equations to the number of unknowns, whereas AMI forms an overdetermined least squares problem using a number of points around each peak. While the references to AMI's methodology are sparse in the literature, a few researchers have reported trying similar procedures in communications with the authors. The initial incarnation of the Algorithm of Mode Isolation presented by Drexel and Ginsberg [21] was a SISO algorithm applicable to undamped modal analysis. This was later expanded to state space modal analysis in [20] and [22]. The preceding algorithms all used an iterative, nonlinear least squares routine for SDOF parameter fitting, resulting in a computationally intense algorithm. In [32], Ginsberg *et al* presented a non-iterative, linear least squares routine for SDOF parameter fitting that was incorporated into AMI in [3], [30] and [31].

1.4 Contributions of this Dissertation

This dissertation presents:

- Global (SIMO and MIMO) extensions of the Algorithm of Mode Isolation, a
- Hybrid, MIMO extension to the Algorithm of Mode Isolation, and a
- Detailed evaluation of the performance of these extensions of AMI on experimental and noise contaminated analytical data.

The significance of global curve fitting will be illustrated in Section 1.4.1. The need for a hybrid identification scheme when dealing with modes whose natural frequencies are very close will then be addressed in Section 1.4.2. The proposed extensions to AMI will be thoroughly evaluated on experimental data and noise contaminated analytical data in subsequent chapters. Some of the reasons for choosing each particular data set will be enumerated in Section 1.4.3.

1.4.1 Global Modal Parameter Identification

This thesis presents global SIMO and MIMO extensions of AMI, whereas previous implementations of AMI were local algorithms. The global / local classifications describe the way in which SIMO, MISO or MIMO data is processed. The modal identification algorithms of interest seek to identify complex eigenvalues (λ_i) or poles (p_i) as well as mode shapes. Eigenvalues are global properties of a structure, meaning that in principle each mode should have the same frequency of vibration and decay rate at every point on a structure. (In analytical work this is obvious, though due to measurement errors it must be imposed as a constraint in experimental work.) Mode vectors on the other hand are considered local properties of a structure. Each element of a mode vector is determined based on the amplitude and phase of vibration at a specific point on the structure.

With this in mind, any SISO algorithm could be used as a SIMO algorithm by simply applying the algorithm at every measurement point. In ideal circumstances, the analysis at each point would result in the same set of eigenvalues. The residues obtained at each

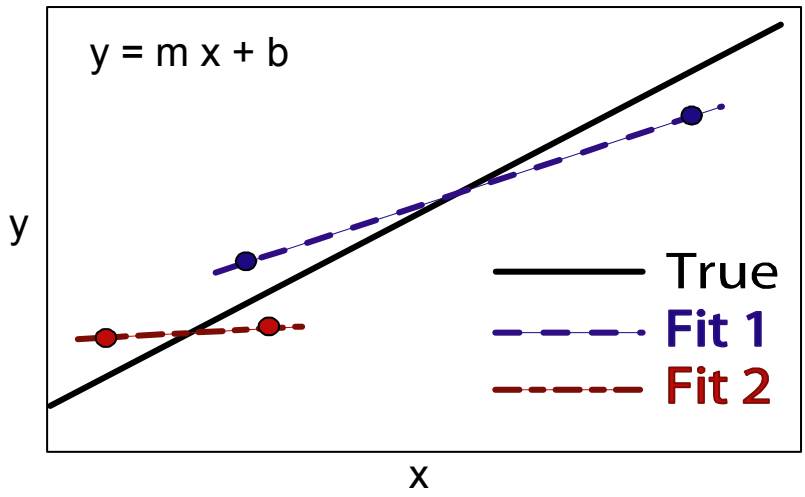

Figure 2: Example of global and local fitting. The solid line indidcates the true linear function while the dashed lines are two independent fits to two data points each. A fit to all four data points simultaneously yields the true linear function.

measurement point could then be collected and scaled to form mode vectors. Similar steps could be used to extend SISO to MIMO. In practice however, the eigenvalues obtained at each point will be different and must be processed in some way (usually averaged) to obtain a consistent, global set. SIMO or MIMO algorithms thus derived from SISO ones are considered local or non-global. When a system has modes with close natural frequencies, the scatter in the eigenvalues from one measurement point to the next might be more than their separation, so that one might not know to which modal parameters to average to obtain a global set. This is compounded by the fact that the signal to noise ratio tends to vary dramatically from one point to the next. On the other hand, a global algorithm considers all data simultaneously, estimating the eigenvalues that simultaneously best fit the response at all measurement points. Often an algorithm is not considered SIMO or MIMO unless it is global, and hence algorithms are not always explicitly designated as global or local in the literature. Global algorithms are generally preferred in practice because data from more than one sensor are often available.

To illustrate the difference between global and local fitting, consider the simple example of finding the slope and y-intercept of a line from measured data. Figure 2 shows four

noise-contaminated experimental data points defining a linear function (solid line), each contaminated by constant amplitude noise. The local approach to parameter estimation involves fitting a subset of the total data set, and then averaging the resulting parameters. The dashed lines represent local fits to two data points each. It is clear that averaging the slope or y-intercept obtained by local fitting does not necessarily yield a good estimate of the true parameter. On the other hand, a fit to all four data points simultaneously yields a good estimate of the true parameters.

A similar situation often occurs in EMA. Some measurements will typically yield accurate estimates of the modal parameters, while other measurements, such as those taken near nodes of a structure, may be dominated by noise. This will be evident in Chapter 3 when processing data from a cantilevered frame structure. Another important advantage of the global approach is that it allows for a significant reduction in user interaction. In Chapter 2, tools for handling multiple FRFs simultaneously will be presented, greatly reducing the user interaction involved in the identification and validation process when many measurements are available. The global algorithms presented herein are applied to various systems in Chapters 3 and 4, processing as many as 243 FRFs simultaneously. In these applications, it will be noted that there can be situations in which simultaneously fitting the response at all measurement points might not be ideal, such as when the system being investigated has modes that are localized in their displacement patterns.

1.4.2 Hybrid Extension to AMI

This thesis also presents a hybrid identification scheme which improves the robustness of AMI when dealing with systems having modes with close natural frequencies. This is needed because a simple global implementation of AMI can encounter difficulty when applied to systems having close natural frequencies. The subtraction stage is based upon the assumption that SDOF fits to FRF data in a narrow band around the peaks will give an adequate approximation of the individual modes of the system. If the resonant peaks for two modes having comparable magnitude merge, an SDOF fit to the merged peak does not give a good approximation of either mode. In such a situation one might subtract countless

modes from a narrow frequency band without reducing the data to noise. On the other hand, if poor approximations of closely spaced modes are accepted in the subtraction phase, a divergent situation may result when the modal parameters are refined in the isolation phase.

This thesis addresses these difficulties by allowing for either a single or multi-mode fit to each set of peak data. The algorithm considers each peak in the FRF data, and applies either an SDOF fit if a single mode is dominant, or an MDOF fit if multiple close modes are dominant. The procedure represents a hybrid approach because it combines the conventional simultaneous, MDOF viewpoint with AMI's concept of sequentially subtracting modal contributions from the data set. It will be shown that when the rank of the FRF matrix in the vicinity of each peak is considered, a robust and semi-automatic algorithm can be created. Furthermore, the algorithm assures that rank-one residue matrices are found for each mode, so that a consistent modal model is always obtained.

1.4.3 Evaluation of AMI

Synthetically generated data from two simple systems will be used to test AMI in Chapter 3. The impulse response for each system was found analytically, contaminated with noise, and then transferred to the frequency domain using a Fast Fourier Transform, in order to mimic a real experiment. The first system consists of an L-shaped frame structure formed by joining two cantilevered beams at their free ends. This system exhibits a few features of interest. First, it has modes with a wide range of damping ratios, resulting in some of the modes being well represented in the FRFs while others are almost dominated by noise. The response in the frequency range of interest also contains a pair of modes whose natural frequencies are separated by less than their average half power bandwidths, so that only one peak is visible in the vicinity of these modes. The displacement patterns of this pair of modes are localized, so that excitation applied on one span of the frame tends to excite only one mode in the pair. As a result, only one mode of the pair is visible in any particular FRF. The second system to which AMI was applied also contains modes with close natural frequencies, however the modes in this second system are globally active so that both modes

appear simultaneously in many of the FRFs. This second system consists of a rectangular plate with simple supports on all sides. The aspect ratio of the plate was chosen to result in three pairs of natural frequencies that are separated by 2%, 3% and 4% of their half power bandwidths. For reference, the pair of close modes in the Frame system were separated by 85% of their half power bandwidth. In summary, these two test systems provide a test of AMI's ability to identify modes with close natural frequencies in two distinct scenarios.

1.5 Other Related Algorithms

Before proceeding, it is worth noting that a few other algorithms have been presented in the literature that also avoid the use of a stabilization diagram. In [7] [8], Balmès describes the IRDC algorithm, a two stage algorithm in which the modes of a system are estimated and then refined using an "ad-hoc" Jacobian based optimization scheme. He recommends initializing the estimates for the system's modes using SDOF methods such as peak picking or circle fit. The algorithm then solves for the residues that best fit the response using least squares. These residues are in turn used in a Jacobian based optimization scheme to arrive at improved estimates for the system's eigenvalues. The process continues until the modal parameters converge. The similarities with the AMI algorithm are apparent, the primary difference being that the AMI algorithm uses mode isolation to improve the modal parameters estimated initially using low order fits, whereas the IRDC uses a Jacobian based scheme. Balmès lists the desire to exclude computational modes from the identification process and the ability to include parameter constraints in the optimization process as justification for the procedure.

The Synthesize Modes and Correlate (SMAC) algorithm provides a user driven approach in which the modes of a system are estimated and improved iteratively. The SMAC algorithm was described initially in [50], and further developed in [51]. As the name of the algorithm indicates, the basic idea behind the SMAC algorithm is to iteratively determine the parameters of the modes whose reconstructions best correlate with the data, using the concept of a modal filter. The algorithm is inherently SIMO, and requires that the modes of interest be sampled with a fine enough spatial resolution so as to be distinguished based

on the linear independence of their mode vectors. As a result, the data set must contain at least as many outputs as there are modes in the frequency band of interest. The algorithm starts by guessing a value for the natural frequency and damping ratio of a mode of the system. A measure of the correlation of that SDOF response with the data is constructed and the procedure repeats for an array of natural frequencies spanning the range of interest. The modes whose responses best correlate with the data are stored, and their parameters are then tuned to maximize the correlation between the reconstructed and measured response for each individual mode. A semi automatic version of the algorithm was presented in [52] and applied to experimental data in [49]. The authors indicate that this automatic version is able to process 90% of the modes in a frequency band of interest automatically, so that the user need only process 10% of the modes manually. This algorithm is similar to AMI in that one is attempting to isolate modes in the response, the primary difference being that AMI isolates modes in the frequency domain whereas the SMAC algorithm attempts to isolate modes spatially. Both algorithms also provide a method capable of identifying the modes of a system without a stabilization diagram, and are applicable to systems having a large number of modes and/or measurement points. Apparently, a MIMO formulation of the SMAC algorithm is under development at Sandia National Laboratories.

1.6 Organization of the Dissertation

The following chapter presents the previous SISO algorithm of mode isolation and discusses the creation of a global, hybrid, MIMO implementation of AMI. In chapter 3 the revised algorithm is applied to noise-contaminated analytical response data from two prototype systems having modes with close natural frequencies. The global SIMO-AMI and global, hybrid, MIMO-AMI algorithms are applied to these systems and the results are compared with those obtained by other conventional algorithms. Chapter 4 presents the application of SIMO and MIMO-AMI to data from the Z24 highway bridge [42] [43] [54]. The results are compared with those found by other researchers using a variety of algorithms, and the relative merits of the SIMO and MIMO algorithms are compared. Chapter 5 presents conclusions and recommendations for future research.

CHAPTER II

GLOBAL & HYBRID-MIMO IMPLEMENTATIONS OF AMI

This chapter begins by presenting the mathematical structure upon which AMI is based. Once this foundation has been established, the original SISO-AMI algorithm presented by Drexel and Ginsberg [21] and further developed by Zaki [82] and Ginsberg and Allen [30] [31] will be presented. The extension of this algorithm to a global SIMO/MISO and global, hybrid, MIMO algorithm will then be discussed.

It is assumed that the system dynamics can be represented by the familiar second order matrix differential equation

$$[M]\{\ddot{q}\} + [C]\{\dot{q}\} + [K]\{q\} = \{F\} \tag{2}$$

where $\{q\}$, $[M]$, $[C]$, and $[K]$ are the generalized coordinate vector, and symmetric mass, damping and stiffness matrices respectively each of dimensions $N \times N$. Alternatively, these same equations of motion can be expressed in symmetric state space form as follows:

$$[S]\{\dot{x}\} = [R]\{x\} + \{Q\} \tag{3}$$

where $\{x\}$, $[S]$, $[R]$ and $\{Q\}$ can be defined as follows

$$\{x\} = \begin{Bmatrix} \{q\} \\ \{\dot{q}\} \end{Bmatrix} \qquad \{Q\} = \begin{Bmatrix} \{0\} \\ \{F\} \end{Bmatrix}$$
$$[S] = \begin{bmatrix} -[K] & [0] \\ [0] & [M] \end{bmatrix} \qquad [R] = \begin{bmatrix} [0] & -[K] \\ -[K] & -[C] \end{bmatrix}. \tag{4}$$

The following definitions can also be used

$$\{x\} = \begin{Bmatrix} \{q\} \\ \{\dot{q}\} \end{Bmatrix} \qquad \{Q\} = \begin{Bmatrix} \{F\} \\ \{0\} \end{Bmatrix}$$
$$[S] = \begin{bmatrix} [C] & [M] \\ [M] & [0] \end{bmatrix} \qquad [R] = \begin{bmatrix} -[K] & [0] \\ [0] & [M] \end{bmatrix}. \tag{5}$$

The general non-symmetric state space form, used in many system dynamics and controls texts, can be obtained by multiplying both sides of eq. (3) by $[S]^{-1}$, provided that $[S]$ is invertible. A set of outputs $\{y\}$ is then defined from linear combinations of the states and inputs, resulting in the following set of equations

$$\begin{aligned} \{\dot{x}\} &= [A]\{x\} + [B]\{u\} \\ \{y\} &= [C]\{x\} + [D]\{u\} \end{aligned} \tag{6}$$

where $\{u\} = \{Q\}$ is the vector of forces or inputs. AMI is valid for any of the descriptions in eqs. (2), (3) or (6).

The data analyzed in MIMO-AMI consists of the frequency response of N_o outputs or measurement degrees-of-freedom (DOF) to harmonic forces at N_i input degrees of freedom denoted $P_1 ... P_{N_i}$. (The input and output degrees of freedom could be interchanged by exploiting reciprocity.) The SISO, SIMO and MISO AMI algorithms each process the appropriate subset of this MIMO data set. For brevity, only measurement of a MIMO data set will be discussed. A MIMO data set consists of the standard collection of FRFs describing the response at each of the outputs to harmonic forces applied at each of the inputs individually. Specifically, the kth data set is a column vector of dimensions $(N_o \times 1)$ at each frequency, describing the response at all measurement points due to a force vector $\{F\}$ that is zero everywhere except the P_kth generalized coordinate or drive point, where a unit force is applied. A column of responses is collected for $k = 1..N_i$, resulting in the frequency response function matrix $[H(\omega)]$, of dimensions $(N_o \times N_i)$ at each frequency point. A number of well established methods exist for collecting such a data set [1], [60]. For any of the models in eqs (2) through (6), provided that the eigenvalues are all underdamped in which case they occur in complex conjugate pairs, the frequency response function matrix can be related to the modal properties by

$$[H(\omega)]_{N_o \times N_i} = \sum_{r=1}^{N} \left(\frac{[A_r]}{i\omega - \lambda_r} + \frac{[A_r^*]}{i\omega - \lambda_r^*} \right) \tag{7}$$

$$[A_r] = \{\psi_r\} \left[L_{P_1,r} \ldots L_{P_{N_i},r} \right] \tag{8}$$

where ω is the frequency, and λ_r and $[A_r]$ are respectively the eigenvalue and residue matrix

of the state-space pole-residue model. The eigenvalue is related to the "undamped" natural frequency ω_r and damping ratio ζ_r by: $\lambda_r = -\zeta_r\omega_r \pm i\omega_r\left(1-\zeta_r^2\right)^{1/2}$. The complex residue matrices returned by AMI have dimensions $N_o \times N_i$, where N_o and N_i respectively denote the number of outputs (or measurement points) and the number of inputs (or drive points.) The residue matrices to be identified must be rank-one, so they can be decomposed into a mode shape $\{\psi_r\}$ and row vector of modal participation factors $\left[L_{P_1,r}\ldots L_{P_{N_i},r}\right]$ as shown in eq. (8), where $P_1 \ldots P_{N_i}$ denote the indices of the input or drive points. For the systems described by eq. (2) and applying the normalization described in [29], the residue can be described in terms of the displacement portion of the state space mode vector $\{\phi_r\}$ as follows

$$[A_r] = \lambda_r \{\phi_r\} \left[\phi_{P_1,r} \ldots \phi_{P_{N_i},r}\right]. \tag{9}$$

At this point it should be noted that in practice, the variables that are measured are not necessarily the generalized coordinates $\{q\}$ of the system. For example, only a finite number of measurements are taken from continuous systems, which have an infinite number of degrees of freedom. Similarly, when a system is modeled discretely, the physical displacements that are measured are linear combinations of the underlying discrete variables. These situations can be represented by defining measurement degrees of freedom $\{y\}$ such that

$$\{y\} = [B]\{q\} \tag{10}$$

where $[B]$ can be non-square. If the system is also excited at the same measurement degrees of freedom $\{y\}$ or some subset thereof, the forces $\{F\}$, associated with the generalized coordinates, are related to the forces $\{u\}$ by

$$\{F\} = [B]^T \{u\}. \tag{11}$$

Taking the Fourier transforms of these definitions and substituting into eq. (7) results in an FRF matrix $[H_y(\omega)]$, in terms of the measurement degrees of freedom, satisfying

$$\{Y(\omega)\} = [H_y(\omega)]\{U(\omega)\} \tag{12}$$

$$[H_y(\omega)] = [B][H(\omega)][B]^T \tag{13}$$

where $\{Y(\omega)\}$ and $\{U(\omega)\}$ denote the Fourier transform of the responses at the measurement degrees of freedom and the forces applied at the measurement degrees of freedom respectively. From this, it is evident that the same number of modes appears in any given frequency band, regardless of which set of FRFs are processed. Furthermore, the pole-residue model in eq. (7) remains valid if the eigenvectors observed at the measurement degrees of freedom $\{u_r\} = [B]^T \{\phi_r\}$ replace the eigenvectors in terms of the generalized coordinates $\{\phi_r\}$.

2.1 Previous, Local, SISO AMI algorithm

The local AMI algorithm sequentially processes each of the N_0 FRFs corresponding to a SIMO data set. The FRF in focus is denoted $H_{jP}(\omega)$ where j and P denote the indices of the measurement and drive points for this FRF. Two processes are applied to this data, both of which use current estimates of the eigenvalues and residue factors to subtract estimated modal contributions from the original data. The term "subtraction residual", denoted as $Y_{j,k}(\omega)$, refers to the data obtained by subtracting from $H_{jP}(\omega)$ estimated contributions for modes 1 to k, where the modes are numbered in the sequence in which they are detected. This data may be evaluated incrementally, such that

$$\begin{aligned} Y_{j,0}(\omega) &= H_{jP}(\omega) \\ Y_{j,k}(\omega) &= Y_{j,(k-1)}(\omega) - \left[\frac{A_{jP,k}}{i\omega - \lambda_k} + \frac{A^*_{jP,k}}{i\omega_m - \lambda^*_k}\right]. \end{aligned} \tag{14}$$

In the Subtraction Phase modes are identified one at a time and their contribution to the FRF is subtracted until all significant modes have been removed. These operations may be summarized by a sequence of algorithmic steps:

S.1 Pick a generalized coordinate j and initialize the subtraction residual $Y_{j,0}(\omega)$ to be the FRF values for this coordinate at a discrete set of frequencies. Initialize the mode number as $k = 0$.

S.2 Identify the frequency range of the most dominant mode in the subtraction residual by searching for $\max(Y_{j,k}(\omega))$. Use an SDOF fit of the data in this frequency range

to estimate the most dominant mode's properties. (This step uses the linear least-squares procedure presented by Ginsberg *et al* [32].) Increment k by one, and assign the identified modal parameters as λ_k and $A_{jP,k}$.

S.3 Form subtraction residual data $Y_{j,k}(\omega)$ according to eq. (14).

S.4 Decide whether $Y_{j,k}(\omega)$ contains the contribution of another mode. If so, return to Step S.2. If $Y_{j,k}(\omega)$ consists solely of noise, then set the initial estimate for the number of modes to be $N = k$, and proceed to the Isolation Phase.

The Isolation Phase has the primary purpose of accounting for the fact that more than one mode might contribute to an FRF, even in the frequency range of a resonance. It uses current estimates for the modal parameters to isolate the contribution of a specific mode. This requires forming an "isolation residual", denoted $X_{j,k}(\omega)$, in which current estimated contributions of all modes other than number k are subtracted from $H_{jP}(\omega)$ according to

$$X_{j,k}(\omega) = H_{jP}(\omega) - \sum_{\substack{n=1 \\ n \neq k}}^{N} \left[\frac{A_{jP,n}}{i\omega - \lambda_n} + \frac{A^*_{jP,n}}{i\omega - \lambda^*_n} \right] \tag{15}$$

The estimated modal properties required to begin the isolation process are those at the end of the Subtraction Phase, and the sequence in which the modes are isolated matches that in which the modes were identified in the Subtraction Phase. The steps required to carry out these operations are:

I.1 Initialize the mode number $k = 0$.

I.2 Increment k by one, and form isolation residual data $X_{j,k}(\omega)$ according to eq. (15). For this, use the latest values for λ_k and $A_{jP,k}$.

I.3 Apply the linear least-squares SDOF fit to $X_{j,k}(\omega)$ in order to obtain refined estimates of λ_k and $A_{jP,k}$. Retain the previous values for convergence tests.

I.4 If $k < N$, return to Step I.2. If $k = N$, compare the new values and old values of all λ_k and $A_{jP,k}$. If these values have not converged, return to Step I.1. (Iterating until the real and imaginary parts of λ_k and $A_{jP,k}$ change by less than 0.01% yields good results.)

I.5 Use the converged set of values for all λ_k and $A_{jP,k}$ to form subtraction residual $Y_{j,N}(\omega)$, which accounts for all modes identified thus far.

I.6 Decide whether $Y_{j,N}(\omega)$ contains the contribution of a (previously unidentified) mode. If not, cease processing of the FRF for the jth generalized coordinate, and return to Step S.1 to process another set of FRF data.

I.7 This step is reached if there is evidence of an additional mode in $Y_{j,N}(\omega)$. Apply the linear least squares SDOF fit to this data in order to obtain initial estimates of λ_{N+1} and $A_{jP,(N+1)}$.

I.8 Increment N by one and return to Step I.1.

All of the preceding operations are straightforward, except for Steps S.4 and I.6, which require a decision as to whether a residual FRF contains the contribution of a mode. If all of the modal contributions have been subtracted, the residual FRF should appear to be incoherent. The most recent procedure requires that the user visually search plots of the data to determine if there is some degree of coherence, e.g. several points form a noticeable peak in a Bode magnitude plot and a regular arc in a Nyquist plot.

2.2 Global, SIMO-AMI

The operations described previously of subtracting and isolating modal contributions need not be limited to a single FRF. The realization that the entire set of FRF data could be processed simultaneously using the same approach described above leads to a global extension of the algorithm of mode isolation. The details of the implementation will be addressed in this section.

The SISO AMI algorithm begins with a single FRF, identifies a frequency interval surrounding the peak in the magnitude FRF, and then processes the FRF data in this frequency interval to obtain an estimate for the eigenvalue and residue of the mode active at the peak. Processing a number of FRFs simultaneously requires a comparable strategy for identifying peak data in all of the FRFs in a logical manner. A dilemma that can arise is illustrated in Figure 3, which displays 99 magnitude FRFs measured in impact tests of the Z24 highway

bridge test described in Chapter 4. Inspection of Figure 3 reveals that the dominant mode in the data is either in the vicinity of 4 Hz or 10 Hz. The data at other frequencies is more difficult to interpret. One can imagine that considering all of the FRFs simultaneously could be quite cumbersome. It would be much more convenient to locate the frequency intervals surrounding each mode on a single FRF that is representative of all of the data. The composite FRF $H_c(\omega)$, defined as the average of the magnitude of the FRFs for all response points, can be used for this purpose. It is defined mathematically as follows,

$$H_c(\omega) = composite([H(\omega)]) = \frac{1}{N_o N_i} \sum_{k=1}^{N_i} \sum_{j=1}^{N_o} |H_{jP_k}(\omega)| . \tag{16}$$

Figure 4 shows a composite FRF of the data in Figure 3. The composite FRF gives a good global picture of the information contained in the individual FRFs. For example, all of the modal peaks seen in Figure 3 are evident in Figure 4. Note that it is difficult to find a single FRF out of the set in Figure 3 that gives as good a representation as the composite does of all of the modes of the structure. One reason for this is that noise in the individual magnitude FRFs is canceled when averaging them to form the composite FRF. These observations support the use of a composite FRF for monitoring the mode subtraction and isolation processes. The composite FRF defined in eq. (16) is a well known mode indicator function (see [63] [64],) and is commonly used in experimental modal analysis.

The global AMI algorithm uses a composite FRF only for monitoring the progress of the subtraction stage and for identifying the data to be fit around each peak. Once the frequency interval containing a mode has been determined, the entire set of FRFs must be processed in order to determine the eigenvalue and mode vector for the mode active in the frequency band of interest. A computationally efficient, global algorithm is derived in the following subsection for this purpose. Data from all FRFs in the frequency interval surrounding the peak in focus are processed by the algorithm, which returns the eigenvalue and residue matrix that best fit the response in a least squares sense.

These simple changes result in a global, SIMO version of AMI. The performance of this algorithm is described in Chapters 3 and 4 for an analytical frame structure and for experimental data taken from the Z24 highway bridge. This approach requires far less

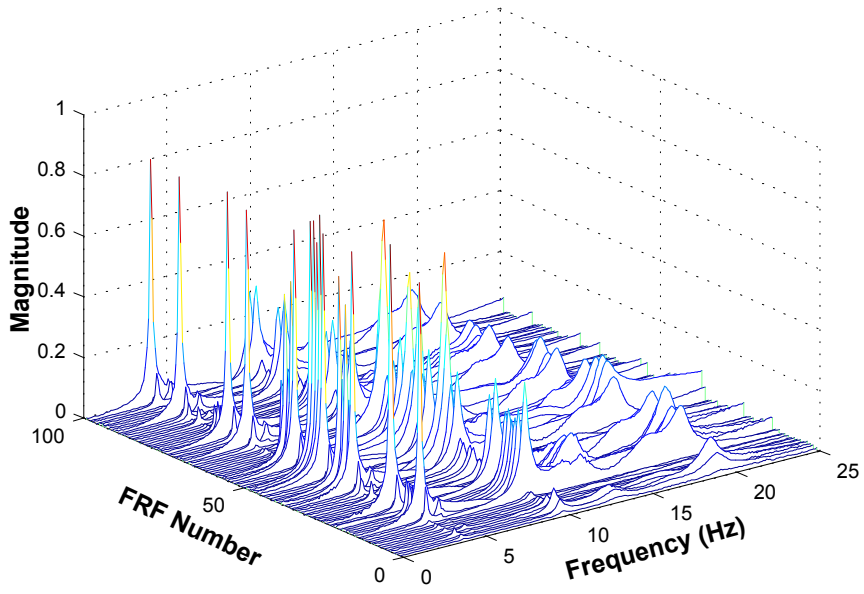

Figure 3: Plot of the 96 magnitude FRFs comprising the drop-test data set for the Z24 bridge, discussed in Chapter 4.

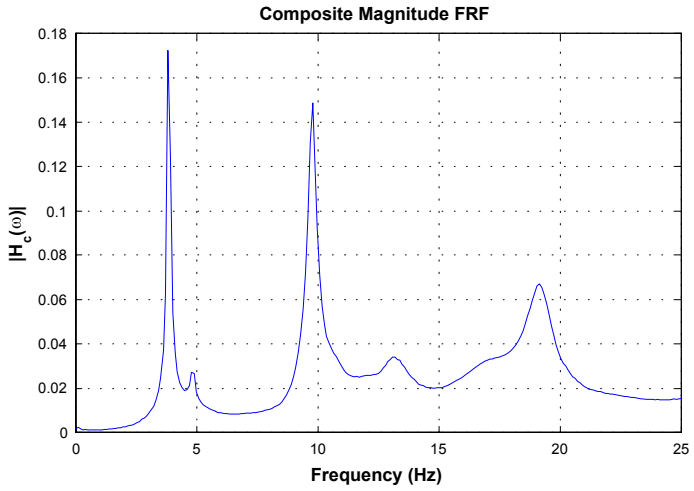

Figure 4: Composite magnitude FRF created from the Z24 drop-test FRFs in the preceeding figure.

user interaction than the SISO approach when identifying a system with a large number of FRFs. Furthermore, the decision regarding when to stop looking for modes is much clearer in the global approach because the FRF data for all measurement points is considered simultaneously.

This extension of AMI is dubbed AMI-SIMO, as it is a global or true-SIMO algorithm.

This eliminates the need for a global mode vector fit after the eigenvalues are identified, as described by Zaki [82], and the difficulty which can arise in determining the global eigenvalues using the local AMI algorithm [3].

2.2.1 Global, SIMO, SDOF Fitting Algorithm

This section describes the global, common-denominator MIMO fitting algorithm used in the global SIMO and MIMO extensions to the Algorithm of Mode Isolation. Allen and Ginsberg presented a SIMO-SDOF algorithm in [4], which was achieved by expanding the data set and vectorizing the SDOF algorithm in [32]. The SIMO-SDOF algorithm in [4] was found to be similar to a continuous time implementation of the LSCF algorithm presented by Guillaume *et al* in [35], [36] and [73], although Guillaume *et al* implemented two features that are attractive for application in AMI. First, they included an extra numerator term in the rational expression of the transfer function. This allows for modeling out of band effects, as described by Formenti and Richardson [28]. Second, Guillaume *et al* formed the normal equations for the least squares problem directly, resulting in a fast, memory saving implementation. The algorithm presented herein incorporates both of these features while following the derivation in [4] rather than that presented by Guillaume *et al*. This change in the derivation, coupled with the restriction that the weighting function be the same for all measurement points, allows for further computational savings. Furthermore, the algorithm derived here allows for an arbitrary number of extra numerator terms to be included in the fit, whereas the derivations in [36] and [73] included only one extra term when the full denominator was found. Inclusion of extra numerator terms in the SDOF fit was found to improve the results for some problems.

The response in eq. (7) for a SIMO data set can be expressed as a ratio of polynomials in $(i\omega)$ with real coefficients as follows:

$$\{H_P(\omega)\} = \frac{\sum_{k=1}^{N_n} \{B_k\} (i\omega)^k}{\sum_{k=1}^{N_d} a_k (i\omega)^k} \tag{17}$$

When SIMO data is used, the FRF data $\{H_P(\omega)\}$ and the vectors of numerator coefficients $\{B_k\}$ both have dimensions of $N_o \times 1$, where N_o is the number of outputs or measurement

points. MIMO data can also be fit to this model by recognizing that the denominator of the FRF matrix in eq. (7) is the same for every column. Hence the columns of $[H(\omega)]$ can be stacked as if they resulted from a SIMO experiment. In this case the vectors of FRF data and numerator coefficients both have dimensions of $N_o N_i \times 1$. This approach is called a "common denominator" approach to MIMO system identification. The model identified using this approach is not necessarily minimal, yet it will be shown in subsequent sections that it can be reduced to a minimal one and also used to create a metric that can reveal modes with close natural frequencies.

The orders of the numerator and denominator polynomials will be left arbitrary in the derivation that follows. Note that for a proper fit to N modes, such as in eq. (7), $N_d = 2N$ and $N_n = 2N - 1$. The numerator order can be increased with the denominator order held constant to account for out of band effects, [65] [67]. This is done by setting $N_n = 2N - 1 + N_{ex}$ where N_{ex} is the number of extra terms desired. The polynomials $(i\omega)^k$ will be written as functions of frequency $\Omega_k(\omega) = (i\omega)^k$, as done in [36] and [73]. Doing so allows the algorithm presented here to also be applied to a discrete-time model like those of the LSCF or LMS Polymax® algorithms, where $\Omega_k(\omega) = \exp(-i\omega k T_s)$ with T_s being the sample time. Other possibilities for $\Omega_k(\omega)$ are Forsythe orthogonal polynomials, as used in the Rational Fraction Polynomial (RFP) algorithm [28], or Chebychev polynomials [34]. For generality, a scalar, frequency dependent weighting function $W(\omega)$ is introduced. This could be used, for example, to implement Sanathanan and Koerner's iterative method [59] [69]. In matrix form, the result of clearing the denominator of eq. (17) at a specific frequency can be expressed as

$$\left[W(\omega)\{H_p(\omega)\}[\Omega_0(\omega)\ \cdots\ \Omega_{N_d}(\omega)] \vdots -W(\omega)[\Omega_0(\omega)[I_{N_o}]\ \cdots\ \Omega_{N_n}(\omega)[I_{N_o}]]\right]\{\alpha\beta\} = \{0\} \tag{18}$$

where

$$\begin{aligned}\{\alpha\beta\} &= \left[a_0\, a_1\ \cdots\ a_{N_d}\ \{B_0\}^T\ \{B_1\}^T\ \cdots\ \{B_{N_n}\}^T\right]^T \\ &= \left[\{\alpha\}^T\ \{\beta\}^T\right]^T\end{aligned} \tag{19}$$

and $[I_{No}]$ is an $N_o \times N_o$ identity matrix. An overdetermined set of equations can be formed

by recognizing that $\{\alpha\beta\}$ are common factors at all frequencies, and then stacking block rows of eq. (18). Each block row has N_o rows. If data for N_f frequencies is included an overdetermined linear system $[J]\{\alpha\beta\} = \{0\}$ results, where the Jacobian matrix $[J]$ has dimensions $(N_o N_f) \times (N_d + N_o N_n)$. The name 'Jacobian' for the matrix $[J]$ comes from the derivation of the linear least squares algorithm [61].

Because the Jacobian matrix is complex, the equations $[J]\{\alpha\beta\} = \{0\}$ are complex even though $\{\alpha\beta\}$ is real. A real system of equations is needed to force $\{\alpha\beta\}$ to be real. This can be obtained by separating each equation into real and imaginary parts and requiring that both be satisfied. Forming the normal equations for the linear least squares problem as $\mathrm{Re}\left\{[J]^H [J]\right\}\{\alpha\beta\} = \{0\}$ yields the same result, where $(.)^H$ denotes the Hermitian. Because the Jacobian matrix $[J]$ can be quite large and quite sparse if many frequencies and/or outputs are included, a much more efficient algorithm results if the normal equations $\mathrm{Re}\left\{[J]^H [J]\right\}\{\alpha\beta\} = \{0\}$ are formed directly, rather than forming $[J]$ and evaluating $\mathrm{Re}\left\{[J]^H [J]\right\}$. The normal equations are

$$\mathrm{Re}\left\{[J]^H [J]\right\}\{\alpha\beta\} = \begin{bmatrix} [A_{11}] & [A_{12}] \\ [A_{12}]^H & [A_{22}] \end{bmatrix}\{\alpha\beta\} = 0 \tag{20}$$

where

$$[A_{11}] = \mathrm{Re}\left(\sum_{j=1}^{N_f} |W|^2 \left(\{H_P\}^H \{H_P\}\right) \begin{Bmatrix} \Omega_0^* \\ \vdots \\ \Omega_{Nd}^* \end{Bmatrix} \begin{bmatrix} \Omega_0 & \cdots & \Omega_{Nd} \end{bmatrix}\right) \tag{21}$$

$$[A_{12}] = -\mathrm{Re}\left(\sum_{j=1}^{N_f} |W|^2 \begin{Bmatrix} \Omega_0^* \\ \vdots \\ \Omega_{Nd}^* \end{Bmatrix} \begin{bmatrix} \{H_P\}^H \Omega_0 & \cdots & \{H_P\}^H \Omega_{Nn} \end{bmatrix}\right) \tag{22}$$

$$[A_{22}] = \mathrm{Re}\left(\sum_{j=1}^{N_f} |W|^2 \begin{Bmatrix} \Omega_0^* [I_{N_o}] \\ \vdots \\ \Omega_{Nn}^* [I_{N_o}] \end{Bmatrix} \begin{bmatrix} [I_{N_o}]\Omega_0 & \cdots & [I_{N_o}]\Omega_{Nn} \end{bmatrix}\right) \tag{23}$$

or equivalently,

$$[A_{22}] = \mathrm{Re}\left(\sum_{j=1}^{N_f} |W|^2 \left(\left\{\begin{array}{c} \Omega_0^* \\ \vdots \\ \Omega_{Nn}^* \end{array}\right\}\left[\begin{array}{ccc} \Omega_0 & \cdots & \Omega_{Nn} \end{array}\right] \otimes [I_{N_o}]\right)\right) \tag{24}$$

In the preceding $\otimes$ denotes the Kronecker product, defined as follows, where C_{ij} is the ijth element of $[C]$,

$$[C] \otimes [D] = \left[\begin{array}{ccc} C_{11}D & C_{12}D & \cdots \\ C_{21}D & C_{22}D & \cdots \\ \vdots & \vdots & \ddots \end{array}\right]$$

Note that in the first block row of eq. (20) the partition $[A_{11}]$ multiplies the denominator coefficients $\{\alpha\}$, while the partition $[A_{12}]$ multiplies the numerator coefficients $\{\beta\}$. Further computational savings result from a two-step solution procedure in which the denominator coefficients are found first. This is done by using the upper partition of eq. (20) to solve for $\{\beta\}$

$$\{\beta\} = -\left[A_{22}\right]^{-1}\left[A_{12}\right]^H \{\alpha\} \tag{25}$$

which is simplified by the identity $([C] \otimes [D])^{-1} = [C]^{-1} \otimes [D]^{-1}$ [9]. Use of this identity requires computation of the inverse of a relatively small N_n square matrix, rather than a much larger $N_o N_n$ matrix. Substitution of eq. (25) into the lower partition of eq. (20) results in

$$\left[[A_{11}] - [A_{12}]\left[A_{22}\right]^{-1}\left[A_{12}\right]^H\right]\{\alpha\} = [M]\{\alpha\} = \{0\}. \tag{26}$$

An additional constraint must be imposed in order to find a solution for the coefficients $\{\alpha\}$. One common approach, the least squares solution (LS), is to constrain the highest coefficient $a_{N_d} = 1$. Another alternative, the so called mixed least squares - total least squares solution (LS-TLS) is presented in [73] as $\{\alpha\} = \{v_{\min}\}$ where $\{v_{\min}\}$ is the eigenvector corresponding to the minimum eigenvalue of $[M]$. The authors have found a slight reduction in bias in some cases when using this mixed LS-TLS solution rather than the LS solution. For the applications presented in this thesis, the LS-TLS algorithm is used. Also, only a single mode is fit ($N = 1$) so that $N_d = 2$ and $N_n = 1 + N_{ex}$ with $N_{ex} = 1$ or 2 typically.

Inspection of the modal representation of the frequency response in eq. (7) reveals that this global SIMO-AMI algorithm could also be used to process data from MIMO experiments by simply vectorizing the FRF matrix. A set of $N_i N_o$ FRFs from a MIMO experiment would then be treated as if they resulted from a SIMO experiment having $N_i N_o$ outputs. Such an approach has been termed a "common-denominator" approach [73]. Unfortunately, this simple approach suffers from a number of drawbacks. First, the residue matrix identified using this approach can have a rank greater than one, and hence cannot always be described by a mode shape and modal participation vector according to the definition in eq. (8). Thus, some loss in quality might be observed when reducing the pole-residue model to a model in terms of modal parameters. The most important drawback of the common denominator approach is that it can fail to accurately identify modes whose natural frequencies are separated by less than their average half power bandwidth. The global algorithm in SIMO form suffers from this same limitation. The data sets to which the SIMO-AMI algorithm is applied in the Chapters 3 and 4 have modes that are close, yet distinct enough to be identified. One the other hand, the SIMO approach fails to identify pairs of close eigenvalues for the simply supported plate system in Chapter 3. The Hybrid, MIMO-AMI algorithm presented in the following section overcomes these difficulties.

2.3 Hybrid, MIMO-AMI

This section describes the global, MIMO-AMI algorithm. The procedural steps will be described along with the pertinent details of the implementation.

2.3.1 Subtraction Phase

As described in the previous sections, AMI is a two-stage process beginning with the subtraction stage in which modes are sequentially identified and subtracted from the experimental data. The algorithm successively considers peaks in the composite FRF (defined in eq. (16),) determining the number of modes contributing to the response and estimates for their parameters. In the SISO and SIMO versions of AMI, modes were identified and subtracted one at a time. The hybrid MIMO-AMI algorithm preserves the idea of subtracting modal contributions from the data. However, it allows for the possibility that

more than one mode might contribute significantly to a peak as a consequence of proximity of natural frequencies. In such situations, groups of modes are simultaneously identified and subtracted from the data.

To begin identifying and subtracting modes, data in a frequency interval surrounding the highest peak of the composite FRF is selected. In the most basic approach a user could manually set frequency bands around peaks of interest in the composite FRF, but such an approach requires an expert user and significant user interaction. Instead, an automatic procedure was used for the problems in this thesis, in which the frequency band is set by including only data for which the composite FRF exceeds a specified fraction of the peak value. This fraction is called the peak selection parameter α, so the selection criterion is

$$H_{\mathrm{c}}(\omega) > \alpha * \max\left(H_{\mathrm{c}}(\omega)\right) \tag{27}$$

For example, $\alpha = 0.707$ corresponds to using all points within the half-power bandwidth. Setting $\alpha = 0.5$ has worked well for many of the problems addressed in this thesis. For some systems, visual inspection might reveal that the frequency points selected using $\alpha = 0.5$ are not concentrated around the peak of interest. For example, data encompassing a number of visually distinct peaks might be selected when using this procedure. When this occurs, a larger peak selection parameter might be needed, resulting in fewer frequency points being selected, so that modes can be identified and subtracted in small groups. This procedure may also give undesirable results when the data is very noisy, so that the peak of interest stands out only slightly above the noise. In such a case a large band of noisy data surrounding the peak of interest may be selected by the algorithm if the peak selection parameter is too small.

The peak data that fits the condition of eq. (27) is processed by the common-denominator, SDOF algorithm, described previously, which returns the eigenvalue and residue matrix for the mode identified. As noted previously, this algorithm processes the FRFs for all $N_i N_o$ input-output combinations globally, as if they resulted from a SIMO experiment with $N_i N_o$ outputs. As a result, the algorithm identifies a $N_o \times N_i$ residue matrix $[A_{\mathrm{fit}}]$ which can have a rank greater than one, but no larger than $\min(N_i, N_o)$. This residue matrix is

decomposed via singular value decomposition as follows

$$[A_{\text{fit}}]_{N_o \times N_i} = [U]_{N_o \times N_i} [S]_{N_i \times N_i} [V]^H_{N_i \times N_i} \tag{28}$$

where $[U]$, and $[V]$, are orthonormal matrices satisfying $[U]^H [U] = [V]^H [V] = [I]_{N_i}$ and $[S]$ is a diagonal matrix whose diagonal entries, the singular values S_k, are in descending order (i.e. $S_1 \geq S_2 \geq \ldots$). The rank of the matrix $[A_{\text{fit}}]$ can be determined by counting the number of singular values of magnitude comparable to the first. The relative magnitude of each singular value is described numerically by its singular value ratio SR_k, defined as

$$SR_k = S_k / S_1 \tag{29}$$

where S_k denotes the kth singular value of the residue matrix. The smallest singular value ratio is then the reciprocal of the condition number of the matrix, a value often used to assess numerical conditioning (i.e. "rcond.m" in Matlab). When $SR_k \ll 1$ for $k > 1$, indicating that a single mode is present, the residue matrix returned by the common denominator algorithm is reduced to rank one by retaining only the part of the SVD which corresponds to the first singular value as follows

$$[A_{\text{fit,R1}}] = \{U_1\} S_1 \{V_1\}^T \tag{30}$$

where $\{U_1\}$ and $\{V_1\}$ denote the first left and right singular vectors respectively. The measured FRF is then compared to an FRF model for the mode, constructed using this rank-one residue and the identified eigenvalue in eq. (7). The agreement is evaluated, as will be described in Section 2.3.1.1, and if the agreement is deemed acceptable, the mode is retained and its FRF model is subtracted from the FRF data forming a set of "subtraction residual" FRF data $[(H_{\text{sub}}(\omega))_1]$ as follows

$$[(H_{\text{sub}}(\omega))_1] = [H_{\text{meas}}(\omega)] - \left(\frac{[A_1]}{i\omega - \lambda_1} + \frac{[A_1^*]}{i\omega - \lambda_1^*} \right) \tag{31}$$

$$[(H_{\text{sub}}(\omega))_s] = \left[(H_{\text{sub}}(\omega))_{s-1}\right] - \left(\frac{[A_s]}{i\omega - \lambda_s} + \frac{[A_s^*]}{i\omega - \lambda_s^*} \right) \tag{32}$$

where s indexes the subtraction step. The mode subtraction procedure is then applied to the highest peak of this new residual. The subtraction process continues in this manner

until a composite FRF of the subtraction residual shows no evidence of additional modes, at which point the algorithm proceeds to the isolation stage, described subsequently.

When the peak data contains the response of more than one mode, the number of singular value ratios SR near one suggests the number of modes active at the peak. In such situations, an MDOF fit of the indicated model order is performed using a MIMO-MDOF algorithm, which returns the eigenvalues and rank-one residue matrices of the identified modes. (The algorithm used for these MDOF fits will be described in Section 2.3.3.) The modal parameters identified by the MIMO-MDOF algorithm are used to reconstruct the response due to these modes using eq. (7). Their response is then compared to the residual FRF data as described in Section 2.3.1.1. If the comparison is deemed acceptable the modal parameters are stored and their contributions to the FRFs are subtracted from the residual FRF data, bringing the next highest peak in the composite FRF into dominance. If inadequate agreement is obtained using both SDOF and MDOF methods, the estimated modal parameters are discarded and the subtraction phase either ceases or proceeds to a different peak in the composite FRF.

Two difficulties can arise during this subtraction process. First, the composite FRF of the subtraction residual might show a peak in the frequency interval of a previously identified mode. (Due, for example, to systematic errors in the data, inaccuracy of the initial estimates of the modal parameters, or narrow-band noise.) As modes are removed from the data set, this peak may come into dominance again, so that one might erroneously attempt to identify additional modes in this frequency band. To avoid this scenario the data within the frequency interval fit by AMI is not included in subsequent searches for additional modes. One can verify that the appropriate number of modes has been identified at each peak after the mode isolation phase has been completed, by subtracting all identified modal contributions from the measured data and searching for additional modes. The second difficulty that can arise is a situation in which the singular values do not clearly indicate the number of modes active at the peak under consideration. For example this is the case if all of the singular value ratios SR_k are near unity. In this case one does not definitively know the number of modes present at the peak under consideration. The only recourse

in that event is to try fitting an increasing number of modes. At each model order, the reconstructed FRFs are compared to the residual FRFs and the lowest order that results in adequate agreement is selected. This will be demonstrated when processing the Z24 data in Chapter 4.

2.3.1.1 Assessing the Quality of Fit using Composite FRFs

The steps described in the preceding use a composite FRF to select frequency intervals to be searched for modes. Composite FRFs also are used to compare the subtraction residual FRFs to the FRFs reconstructed from the parameters of the mode(s) under consideration. The use of composite FRFs expedites the assessment because visually examining plots of each individual FRF would be quite tedious. Two types of composites are employed. The magnitude composite, defined in eq. (16), is a standard way of displaying FRF data, and provides the first means for comparison. It is also helpful to have a comparison that includes the phase of the responses, such as a Nyquist plot, when working with noisy data. One reason for this is that both close modes and noise can be manifested as peaks on a magnitude FRF. Close modes are more easily distinguished from noise features on a Nyquist plot, where modes tend to look like circles or arcs while noise tends to show an irregular shape. Unfortunately, there does not seem to be a standard definition of a composite FRF that retains phase information. The composites formed by eq. (16) can not be used to create a Nyquist plot because they contain no phase information, while simple addition of FRFs can lead to cancellation of some modes' contributions, depending on their spatial phase. For example, adding FRFs for a symmetric structure would tend to reinforce symmetric modes while annihilating antisymmetric modes. For this reason a Nyquist composite FRF was defined in [6] as a weighted sum of the FRFs using the elements of the identified residue vector $\{(A_{\text{fit}})_r\}$ as weights. Use of the residue vector for mode r tends to reinforce mode r in the sum. The Nyquist composite FRF data $(H_{\text{cn}})_r(\omega)$ for a

MIMO data set is defined as follows

$$\begin{aligned}(H_{\mathrm{cn}})_r(\omega) &= tr\left([(A_{\mathrm{fit}})_r]^H * [H(\omega)]_{N_o \times N_i}\right) \\ &= \sum_{k=1}^{N_i} [(A_{\mathrm{fit}})_r](:,k)^H * [H(\omega)](:,k)\end{aligned} \tag{33}$$

where $tr()$ denotes the trace, $[(A_{\mathrm{fit}})_r]$ is the current estimate of the residue matrix for the mode in focus and $[H(\omega)]$ is the FRF data to be condensed. The notation $[X](:,k)$ signifies the kth column of matrix $[X]$. The data $(H_{\mathrm{cn}})_r(\omega)$, which is termed a "Nyquist Composite," can be plotted in the complex plane. Clearly the Nyquist composite FRF is dependent on the residue matrix used in forming it, and hence is only meaningful for a single mode. When multiple modes are identified at a single peak, a composite Nyquist FRF is created for each individual mode. The motive is to evaluate how well the FRFs reconstructed using the parameters of each mode match the measured FRFs. Towards this end, eq. (7) is used to construct an FRF model for each mode, which is condensed according to eq. (33), resulting in a "fit" Nyquist composite FRF. This is compared to a Nyquist composite FRF of the isolation residual $[(H_{\mathrm{isol}}(\omega))_s]$ for the same mode, defined as follows

$$[(H_{\mathrm{isol}}(\omega))_s] = [H_{\mathrm{meas}}(\omega)] - \sum_{\substack{r=1 \\ r \neq s}} \left(\frac{[A_r]}{i\omega - \lambda_r} + \frac{[A_r^*]}{i\omega - \lambda_r^*}\right) \tag{34}$$

where s is the index of the mode being isolated and $[H_{\mathrm{meas}}(\omega)]$ is the measured set of FRFs. The summation extends over all modes identified. Examples of the comparison between the Nyquist composite of the "fit" FRF and the isolation residual may be seen by considering the right panes of Figure 17 for an example that will be explored later.

It is also useful to have a quantitative metric expressing how well the reconstructed FRFs agree with the residual FRFs near the peak in focus. Towards this end, an FRF Reduction Factor RF is defined according to

$$RF = \frac{\max\left(composite\left([H_{\mathrm{meas}}(\omega)]\right)\right)}{\max\left(composite\left([H_{\mathrm{meas}}(\omega)] - [(H_{\mathrm{fit}})_k(\omega)]\right)\right)}. \tag{35}$$

where the FRF matrix reconstructed from the mode or modes identified at the kth peak (or kth step of the subtraction stage) is designated $[(H_{\mathrm{fit}})_k(\omega)]$. This metric is constructed

from data in a frequency band that is twice as wide as that used in the fit in order to quantify how well the fit can be extrapolated. Values greater than unity indicate that the FRFs would be reduced by subtracting the contribution of the mode under consideration. Typically, values greater than 3 indicate a good fit. The reduction factor and singular value ratio metrics can be combined to automate the subtraction phase of AMI. This was done when MIMO-AMI was applied to analytical, noise contaminated data in Chapter 3. The details and shortcomings of the automatic procedure will be described in Chapter 3.

2.3.2 Mode Isolation Stage

Once all of the modes of the system have been approximated, the estimate for each mode is refined through an iterative procedure to account for the possibility of overlapping contributions from other modes. Previous versions of AMI isolated individual modes in each step. In the hybrid approach either single modes or groups of closely spaced modes found simultaneously during the subtraction stage are "isolated." At this stage the algorithm proceeds through the groups of modes in the same sequence in which they were identified. First, the contributions of all modes except for those in focus are subtracted from the FRFs forming an isolation residual. This is similar to the isolation residual in eq. (34), although in this case the summation excludes all modes identified at the peak under consideration. This residual then predominantly contains the contributions of the modes in focus. Processing it with the same parameter identification scheme used in the subtraction phase yields improved estimates of the mode or modes in focus. Specifically, if the isolation residual contains the contribution of a single mode, the common-denominator SDOF algorithm is used and the resulting residue is reduced to rank-one using the SVD as described previously. When multiple modes are present, the MIMO-MDOF algorithm is used. A cycle through all groups of modes constitutes one iteration. Computations cease when the largest change in any eigenvalue or any element of any residue matrix falls below 0.001%. Typically only a few iterations are required.

2.3.3 MIMO, MDOF Fitting Algorithm

The subtraction and isolation phases require a MIMO-MDOF algorithm to treat groups of modes with close natural frequencies. Several MIMO, frequency domain algorithms have been presented in the literature. Many are common-denominator algorithms, such as that presented in Section 2.2.1, which work well when identifying distinct modes, but might miss very closely spaced modes or yield a poor fit for close modes after their residue matrices are reduced to rank-one, see [36], [73] and [74]. A few algorithms directly identify a consistent modal model, i.e. one that has rank-one residue matrices. Such a result is obtained when a right matrix fraction polynomial model is fit to the data [36], [74], though such a model requires that the number of modes estimated be an integer multiple of the number of inputs. Another alternative, the Frequency Domain Direct System Parameter Identification (FDDSPI) algorithm (also called Poly-Reference Frequency Domain (PRFD) in [2]) has the same limitation. The frequency domain subspace algorithm (SSI-FD) presented by Van Overschee and De Moor in [76] offers an attractive alternative, in which the number of modes estimated is not required to be a multiple of either the number of inputs or outputs. Van Overschee and De Moor present two subspace algorithms in [76], a "simple" algorithm that suffers from ill-conditioning in the data matrices for high model order, and an algorithm in which the ill-conditioning is reduced using Forsythe orthogonal polynomials. Because AMI only needs to simultaneously identify a few modes, the simple algorithm was implemented. This simple SSI-FD algorithm was found to be surprisingly fast when fitting a small amount of data with a low order fit, and ill conditioning was not encountered.

2.4 Summary

Three incarnations of the Algorithm of Mode Isolation were presented in this Chapter. The previous, local, SISO implementation was presented first. It can be used for SIMO data by processing the FRFs for a SIMO data set sequentially. A global, SIMO implementation of AMI, which processes all SIMO FRFs simultaneously, was then presented. This global, SIMO algorithm is applicable to a wide range of systems, as illustrated in Chapters 3 and 4, but it can encounter difficulty in some situations where modes have very close natural

frequencies. For this reason, a hybrid, implementation of AMI was presented that identifies groups of very close modes simultaneously. Hybrid AMI is most robust when it is applied to a MIMO dataset because the rank information contained in the FRF matrix alleviates the ambiguity associated with modes having similar eigenvalues. Nevertheless, Hybrid AMI can also be applied to SIMO or SISO data.

Because MIMO-AMI employs an MDOF identification scheme when modes are close, there exist, at least theoretically, systems to which MIMO-AMI would offer no advantage over conventional methods. For example, suppose the separation between each natural frequency and its neighbors is less than 50% of the average half-power bandwidth. A composite FRF for such a system might show only one broad peak, so that the hybrid algorithm would be required to process the FRF data encompassing all of the modes of the system simultaneously. This is the typical MDOF approach. Such a situation can occur in the very high frequency range of built-up systems, but that is not where EMA is usually performed. In the lower frequency regime only a few modes are likely to be clustered in a narrow frequency interval. In such cases the fact that AMI only processes peak FRF data significantly enhances its computational efficiency and its robustness in the presence of noise.

CHAPTER III

ANALYTICAL TEST PROBLEMS

This chapter describes the application of AMI to synthetic data from two prototype systems. The first, a cantilevered frame, contains modes that have moderately close natural frequencies, are weakly excited, and are localized in their displacement patterns. The global SIMO and MIMO-AMI algorithms are applied to data for this system in Sections 3.1.1 and 3.1.2 respectively, demonstrating the advantages of the MIMO algorithm. The modal parameters found by AMI are compared with those found by the Stochastic Subspace Identification Algorithm (SSI.) Section 3.1.3 demonstrates that exponentially windowing the impulse responses prior to FRF creation can improve the accuracy of the modal parameters identified by AMI. The selection of the optimum exponential window for this purpose is discussed. The application of AMI to a second prototype system, a simply supported plate, is presented in Section 3.2. This second system contains modes with very close natural frequencies that are globally active. The Hybrid, MIMO-AMI algorithm is applied to synthesized data from this system, demonstrating the ability of the MIMO-AMI algorithm to detect and identify modes with close natural frequencies. For comparison, the Poly-reference Least Squares Complex Frequency domain algorithm is applied to the plate data in Section 3.2.1.

3.1 Cantilevered Frame System

No single test problem can capture every difficulty that could occur in a real experiment. The intent of this first problem is to capture the effect of varying noise levels, weakly excited and localized modes, and close modes. It has been used to assess previous implementations of AMI [3], [20], [22]. The parameters of an exercise offered by Ginsberg [29] were adjusted to obtain a system in which a pair of modes have close natural frequencies. The problem consists of two orthogonal cantilevered beams, welded at their free ends, as depicted in

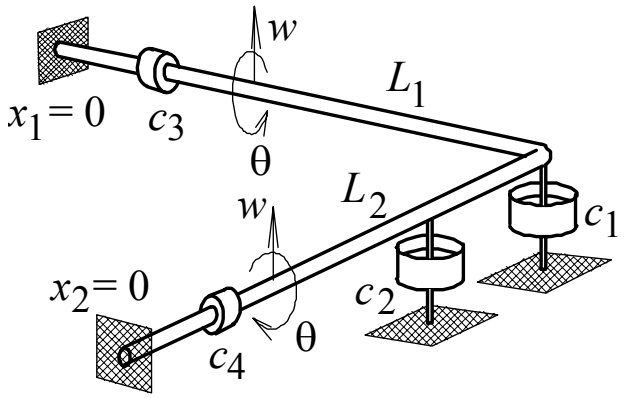

Figure 5: Schematic of Cantilevered Frame System.

Figure 5. Their junction has the effect of coupling the out-of-plane flexural displacement w and torsional rotation θ. Each beam had a solid circular cross section with 100 mm radius, modulus of elasticity $E = 70 \times 10^9$ Pa, modulus of rigidity $G = 26.32 \times 10^9$ Pa, and 2700 kg/m^3 density. The span lengths were set at $L_1 = 4$ m, $L_2 = 3.85$ m. Two transverse dampers, $c_1 = c_2 = 155.88$ N-s/m, oriented out-of-plane were placed at $x_1 = 4$ m and $x_2 = 3$ m. In addition, two torsional dampers, $c_3 = c_4 = 77.94$ N-s-m/rad, were placed at $x_1 = x_2 = 1$ m.

The span lengths were selected because they lead to two modes having close natural frequencies and modal patterns that are localized to one span, as will be seen. This occurs because $L_2 = L_1$ gives a symmetric system, so that setting L_2 slightly different from L_1 represents a small deviation from symmetry of a system consisting of weakly coupled components. As described by Pierre, Tang, and Dowell [58], one cause of mode localization is weak coupling between two energy depositories that deviate slightly from perfect symmetry. In the present system, the energy depositories are the individual spans, and the coupling is provided by their welded connection. (An evaluation of the natural frequencies as a function of L_1 with $L_1 + L_2$ held fixed would show veering of the eigenvalue loci, which often accompanies mode localization, as shown by Chen and Ginsberg [16].) Because the modes having close natural frequencies also have regions of low modal response, the selected values of L_1 and L_2 lead to a strong test of AMI's capabilities.

To construct an analytical model of the system the transverse deflection and torsional

rotation of each beam were represented by Ritz series, with the associated Ritz coefficients serving as generalized coordinates for the system. The expansions for beam $n = 1$ or 2 are given by

$$w(x_n, t) = \sum_{j=1}^{N_R} \left(\Psi_w^{(n)}\right)_j \left(q_w^{(n)}\right)_j$$
$$\theta(x_n, t) = \sum_{j=1}^{N_R} \left(\Psi_\theta^{(n)}\right)_j \left(q_\theta^{(n)}\right)_j \tag{36}$$

A similar model was constructed by Zaki [82] using monomial functions, but they lead to numerical problems due to ill-conditioning when the series length is increased beyond $N_R = 5$. For that reason, the eigenfunctions of a clamped-free beam were used in the following as the basis functions for both beams. These are

$$\begin{aligned}\left(\Psi_w^{(n)}\right)_j &= \sin\left(\alpha_j \frac{x_n}{L_n}\right) - \sinh\left(\alpha_j \frac{x_n}{L_n}\right) \\ &\quad -R_j\left[\cos\left(\alpha_j \frac{x_n}{L_n}\right) - \cosh\left(\alpha_j \frac{x_n}{L_n}\right)\right] \\ R_j &= \frac{\sinh(\alpha_j) + \sin(\alpha_j)}{\cosh(\alpha_j) + \cos(\alpha_j)}\end{aligned} \tag{37}$$

$$\left(\Psi_\theta^{(n)}\right)_j = \sin\left[\frac{(2j-1)\pi x_n}{2L_n}\right] \tag{38}$$

The response data presented here were obtained by truncating each series at $N_R = 11$. Bernoulli-Euler beam theory gives functionals describing the kinetic and strain energy in terms of w and θ, while the Rayleigh dissipation function depends on w and θ at the dashpot locations. Substitution of eqs. (36) into those expressions yields quadratic sums in the generalized coordinates or velocities. A similar operation applied to the virtual work yields the generalized forces. Lagrange's equations then lead to a set of $4N_R$ ordinary differential equations for the Ritz series coefficients.

The Lagrange equations do not couple the motion of the two beams. That effect is described by constraint conditions enforcing continuity of transverse displacement, and of

Table 2: Eigenvalues for First 11 Modes of Frame Structure

Mode	ω_r	$\zeta_r * 100$	$\zeta_r \omega_r$
1	68.008	0.9653	-0.66
2	265.91	0.06169	-0.16
3	386.32	0.12491	-0.48
4	829.45	0.03220	-0.27
5	1033.8	0.07676	-0.79
6	1697.0	0.03599	-0.61
7	1937.9	0.16103	-3.12
8	2479.7	0.75799	-18.80
9	2511.0	0.72183	-18.13
10	2995.7	0.17847	-5.35
11	3380.0	0.15417	-5.21

rotation about the axis of each beam. It is required that

$$\begin{aligned} w(x_1 = L_1) &= w(x_2 = L_2) \\ \left.\frac{\partial w}{\partial x_1}\right|_{x=L_1} &= -\theta|_{x_2=L_2} \\ \left.\frac{\partial w}{\partial x_2}\right|_{x_2=L_2} &= \theta|_{x_1=L_1} \end{aligned} \tag{39}$$

Substitution of the Ritz series into the preceding leads to three algebraic constraint equations that supplement the $4N_R$ Lagrange equations. The unknowns are the Ritz series coefficients and three Lagrange multipliers. An elimination process based on solving the constraint equations for three generalized coordinates reduces the system to a set of $4N_R - 3$ differential equations. These equations may be solved through a state-space formulation for $8N_R - 6$ eigenvalues. Heavy damping would lead to overdamped modes marked by pairs of real eigenvalues. The more usual case is underdamped modes, which correspond to pairs of complex conjugate eigenvalues. This was the situation for all modes of the present system, so there were $4N_R - 3 = 41$ complex modes. The identification was focused on a band of frequencies containing only the lowest 11 modes. The natural frequencies, damping ratios and decay constants for these modes are shown in Table 2.

One can anticipate that the FRFs will exhibit mode coupling whenever the frequency difference $\omega_{r+1} - \omega_r$ is less than $-\operatorname{Re}(\lambda_{r+1}) - \operatorname{Re}(\lambda_r)$. This is the case for modes 8 and 9. Also notable is the wide range of damping ratios, which will be seen to significantly affect the data analysis.

The present work assesses AMI's performance when applied to synthetic FRF data describing the transverse displacement and torsional rotation at four locations on each beam: $x_1 = 1$, $x_2 = 2$, $x_3 = 3$, and $x_4 = 4$ m on beam 1 and $x_5 = 1$, $x_6 = 2$, $x_7 = 3$, and $x_8 = 3.85$ m on beam 2. Both beams have the same displacement at their junction. As a result, the data to be synthesized consists of fifteen impulse responses: seven displacements and eight rotations, which were grouped to form a vector according to

$$\{y(t)\} = [w_1\ w_2\ w_3\ w_4\ \theta_1\ \theta_2\ \theta_3\ \theta_4\ w_5\ w_6\ w_7\ \theta_5\ \theta_6\ \theta_7\ \theta_8]^{\mathrm{T}} \tag{40}$$

The twenty-one lowest eigenvalues and associated mode functions obtained from the Ritz series analysis of the system were used to construct the impulse response resulting from excitation at one meter from the clamped support of the first beam, and then a second impulse response resulting from excitation at one meter from the clamped support of the second beam. ($P_1 = 1$, $P_2 = 9$, see eqs. (7) and (40).) Both impulse responses were obtained analytically by employing a modal transformation that led to a set of uncoupled equations for the modal generalized coordinates. The impulse response of a modal coordinate has the general form $\xi_k = C_k \exp(\lambda_k t)$, where λ_k are the modal eigenvalues and the participation factors C_k depend on the modal coefficients for the drive point. The modal coordinates were evaluated at a uniform increment of time at a fixed sampling rate Δt within a window $0 \leq t \leq t_{\max}$, based on sampling criteria discussed later. The state-space modal transformation then yielded a data set describing the history of the unconstrained set of Ritz series coefficients. Values of the full set of Ritz series coefficients were then obtained from the solution of the constraint equations. Finally, the impulse responses of the $\{y\}$ variables were obtained by synthesizing the Ritz series, eqs. (36). The same procedure when applied to the state-space eigenvector lead to the displacement pattern in any mode. Details of each step of this analysis are provided by Ginsberg [29].

In the applications that follow, the data were contaminated by either Gaussian or uniformly distributed noise, as will be discussed for each case. FFT processing of the noise contaminated impulse response data for each input-output pair then yielded the noise-contaminated FRF matrix $[H(\omega)]$.

3.1.1 SIMO-AMI (Applied to first drive point)

For the first test, SIMO-AMI was applied to the set of 15 responses for an impulse excitation at the first drive point $P_1 = 1$. The impulse response of each element of $\{y(t_n)\}$ was contaminated by white noise that was scaled relative to the peak magnitude of that variable, according to

$$y_j(t_n)_{\text{corrupt}} = y_j(t_n) + \alpha \max_n (y_j(t_n))\, r_{jn} \tag{41}$$

where $-1 < r_{jn} < 1$ is a uniformly distributed random number and α is a constant that scales the random value to the required fraction of signal amplitude (0.02 for the data analyzed here). The noise contaminated impulse responses were then transformed to frequency response functions (FRFs) via a Fast Fourier Transform (FFT). It is important to note that $\alpha = 0.02$, does not correspond to a signal to noise ratio of 50 (34 dB) for each mode. All modes are not excited equally, so the signal to noise ratio varies from mode to mode. Furthermore, the amplitude of the noise is scaled based on the maximum response amplitude, which occurs early in the time record. The amplitude of the response, and hence the signal to noise ratio, is lower for the rest of the time record. Signal to noise ratios ranging from 60 dB to negative were observed in the FRFs in the vicinity of the modes. These observations will be important when evaluating the accuracy of the modal parameters identified in this and subsequent sections.

The sampling rate was set by the Nyquist criterion for the highest natural frequency, which required

$$\Delta t < \pi / \max(|\text{Im}(\lambda_k)|). \tag{42}$$

The time window in which the impulse responses were sampled was set such that the slowest decaying complex modal coordinate reduced to an amplitude not exceeding 10% of its maximum. This was attained if

$$t_{\max} > \ln(0.1) / \min(|\text{Re}(\lambda_k)|). \tag{43}$$

The values that were used were $t_{\max} = 14.2$ sec. and $\Delta t = 0.217$ ms, which corresponds to 2^{16} time values for each displacement variable. Because of the large range of modal decay

constants for the modes of interest, this resulted in all of the modal coordinates except those for modes 2 and 4 being reduced to 0.1% or less of their initial amplitudes. A prohibitively large data set would have been needed to satisfy both the Nyquist criterion and a more stringent leakage requirement for all of the modes simultaneously. In Section 3.1.3 various exponential windows will be applied to the data, illustrating the effect of leakage on the modal parameters for modes 2 and 4.

Eleven modes are present in the frequency band of interest (0 to 3800 rad/s), but the high frequency modes (8-11) were barely visible in the noise-contaminated displacement data, an example of which was shown in [3]. In contrast, the higher frequency modes are fairly well represented in the rotation data, as typified by Figure 6. Only a single peak is evident in the vicinity of modes 8 and 9.

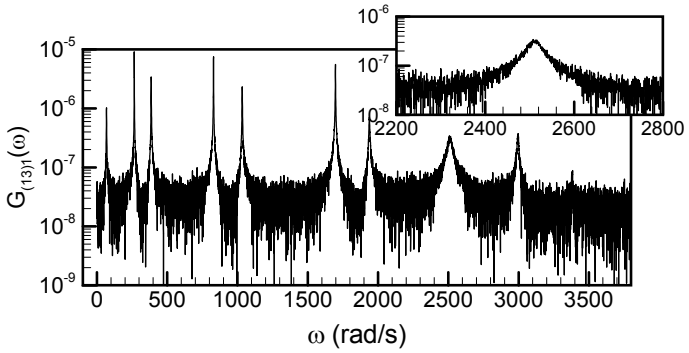

Figure 6: Noisy rotation FRF for 65k point data set at $x = 2$ m on beam 2.

As a reference for the results that follow, the peak-picking and half-power bandwidth methods were applied to the composite FRF. Because no peak is evident in the composite FRF in the vicinity of mode 8, it was missed by the peak picking method. The average of the absolute value of the errors in the real and imaginary parts of the eigenvalues for the first seven modes were 10% and 0.039% respectively. These were dominated by errors in modes 1 and 4 because of the coarseness with which the FRF was sampled in the vicinity of these peaks. Without these modes, the average errors drop to 2.3% and 0.010%. For modes 9-11 the average errors were 11% and 0.025%.

The initial FRFs processed by AMI were created with an impulse response of length

65,536 samples. The FRFs for frequencies from 0 to 3800 rad/s (i.e. the first 8589 data points in each 32,769 point FRF) were analyzed with SIMO-AMI with the peak selection parameter α equal to 0.707, (see eq. (27).) After each subtraction step, composite FRFs were formed to assess the quality with which the identified mode matched the data. To this end, the identified modal properties were utilized to synthesize individual FRFs. Composites of both the residual FRFs and the synthesized FRFs were then constructed according to eq. (16) and compared.

The procedure for each subtraction step is summarized as follows. The algorithm begins by fitting a mode to the data surrounding the peak in the composite FRF, $H_{\mathrm{c}}(\omega)$ in eq. (16), formed from the residual FRF data. The parameters for the identified mode are used to synthesize the FRFs. The synthesized FRFs are compared with the residual FRFs by comparing a composite FRF, $H_{\mathrm{c}}(\omega)$ in eq. (16), and a Nyquist composite FRF, $(H_{\mathrm{cn}})_r(\omega)$ in eq. (33), of each. If the agreement is deemed acceptable, the modes are accepted and subtracted from the residual FRF data and a new subtraction step begins. If unacceptable agreement is obtained, the algorithm either proceeds to a different frequency interval or the subtraction phase ceases. This is illustrated for the last few subtraction steps on the frame data in Figure 7. Each row of panes displays the data at a single subtraction step. The pane on the left shows a composite FRF formed from the residual FRFs at the current subtraction step and a composite FRF formed from the synthesized or 'fit' FRFs for the mode identified in the current subtraction step. The pane on the right shows Nyquist composite FRFs of the same, both of which are created using the residue for the mode identified in the current subtraction step in eq. (33).

The plots in Figure 7 show that the identified modes fit the residual data well for subtraction steps eight through ten. The agreement in steps one through seven was even better. As shown in Figure 7, no peak was visible in the composite FRF at step 11, so subtraction ceased with ten modes identified. Comparison of the parameters of the identified modes with the analytical ones reveals that mode 8 was not identified.

After subtraction, AMI proceeds to the mode isolation stage. Four iterations were performed on this data, at which juncture the maximum change in either eigenvalues or

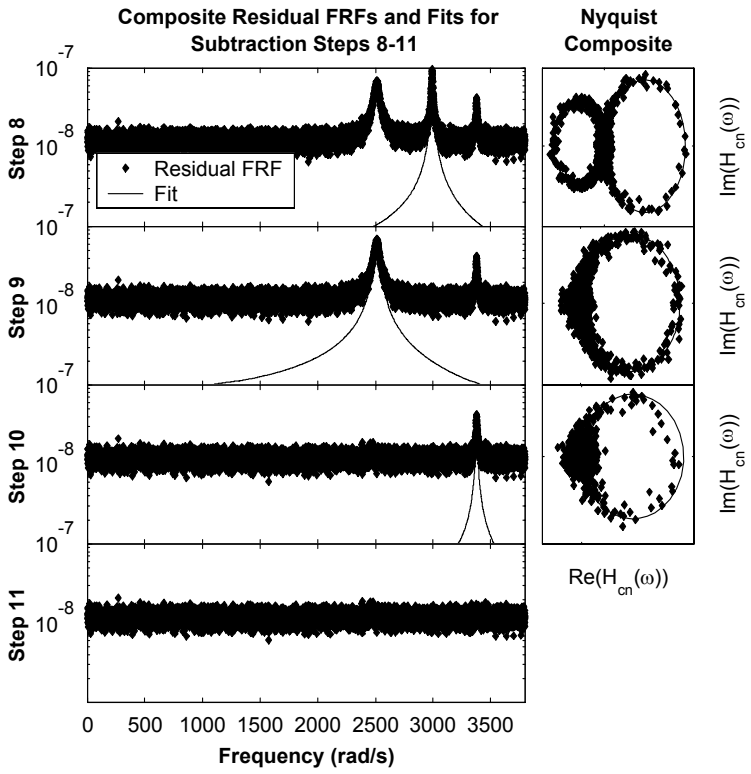

Figure 7: SIMO-AMI applied to 65k point Frame data set. LEFT: Composite residual FRF (.) and composite fit (-) for subtraction steps 8-11. RIGHT: Nyquist composite plots of residual data (.) and fit (-) for subtraction steps 8-11.

residues was 0.001%. Figure 8 shows a composite FRF of the data, AMI's fit and the difference between the two. The latter is comparable to the noise level (10^{-8}).

Table 3 shows the percent errors in the eigenvalues obtained by both the global SIMO-AMI algorithm and previously reported results [3] of the local, SISO AMI algorithm. In all of the following tables error is defined as: $e_{pct} = (identified - true) * 100/true$, and the percent errors in the imaginary parts have been multiplied by 1000. The presence of mode 8 in the data has adversely affected the estimation of mode 9 because AMI is trying to fit a single mode to the response of two modes. Even then, the estimate of the ninth eigenvalue is reasonable considering the noise. For the other modes the errors for the SISO and SIMO algorithms are comparable, though the global algorithm is more accurate on average, especially for the lower frequency modes. Both algorithms are about 2 orders of magnitude more accurate than the peak picking method for the first seven modes. The non-global,

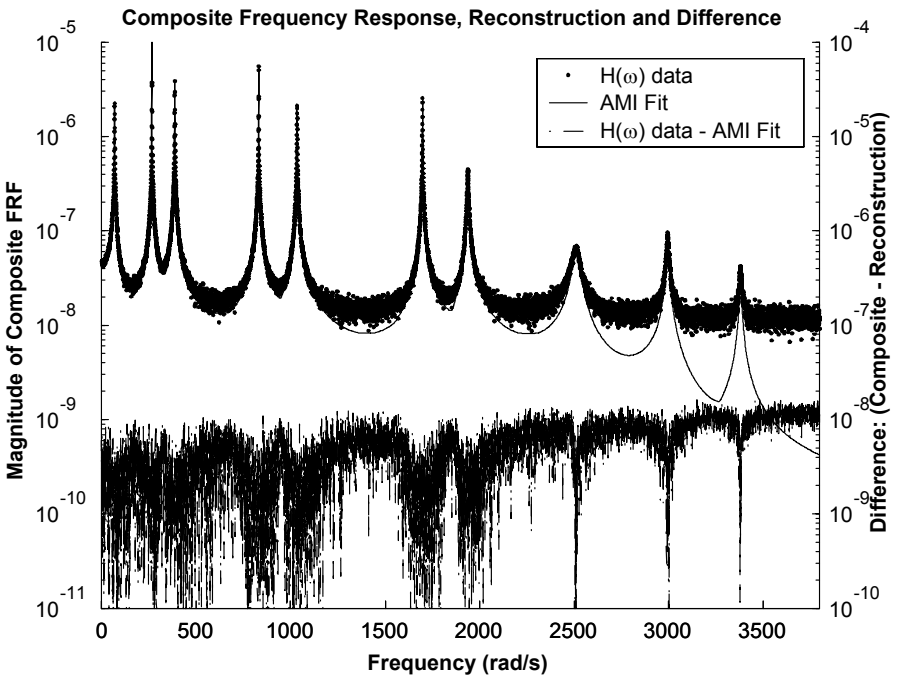

Figure 8: SIMO-AMI results for 65k point frame data set. Composite of FRF data and AMI reconstruction - left vertical axis. Composite of (FRF data minus AMI Reconstruction) - right vertical axis.

SISO AMI algorithm identified the highly localized mode 8, albeit with considerable error, and it did as well as the SIMO algorithm for modes 9-11. The success of the SISO AMI algorithm in identifying mode 8 can be attributed in part to the localized nature of modes 8 and 9. While mode 9 is the dominant mode of the pair in most of the FRFs, there were a few FRFs in which mode eight dominated the response. SISO AMI was able to identify mode 8 in these FRFs, while identifying mode 9 in many of the other FRFs, resulting in estimates of the parameters of both modes. In contrast, the global SIMO algorithm attempts to identify modes from all FRFs simultaneously. Because the global effect of mode 8 is small, it falls below the noise threshold in the composite FRF, and hence was not identified by SIMO-AMI. This difficulty is exacerbated by the fact that when globally fitting mode 9 in the subtraction phase, some of the contribution of mode 8 is mistakenly attributed to mode 9, so that when mode 9 is subtracted from the data set, the amplitude of the response in the vicinity of mode 8 is further reduced.

A significant advantage of the global algorithm is that user interaction and processing

Table 3: Percent Errors in Eigenvalues From Global and Non-Global AMI for 65k sample data set

	SIMO-AMI (Global)		SISO AMI (Non-Global)	
Mode	**Re**	**Im*1000**	**Re**	**Im*1000**
1	0.04%	0.01%	0.11%	-0.22%
2	0.01%	-0.01%	-0.06%	-0.10%
3	-0.07%	0.07%	-0.22%	-2.05%
4	0.04%	0.01%	0.01%	-0.03%
5	0.05%	0.03%	0.08%	-0.28%
6	0.08%	-0.02%	-0.13%	-0.07%
7	0.17%	-0.97%	1.72%	-1.30%
8	missed	missed	-21.71%	-450.32%
9	9.85%	19.34%	3.82%	7.51%
10	4.61%	-1.67%	5.23%	-6.60%
11	27.97%	2.92%	8.15%	-9.75%

time were greatly reduced. Also, with the SISO algorithm it was often difficult to tell when to stop looking for modes. In many of the FRFs it was not possible to identify all of the modes, because the contributions of some of the modes were at or near the noise threshold. As a result, the user had to determine by trial and error when all possible information had been extracted from each FRF, and it was difficult to be sure that all modes had been identified in at least one FRF. In contrast, when using the global algorithm there was no ambiguity concerning when to stop looking for modes, as illustrated by Figure 7. When step eleven was reached there was clearly no indication of a mode with a global effect.

The mode vectors found by AMI-SIMO agree very well with the analytical mode vectors. Figure 9 shows the imaginary parts of the AMI mode shapes compared with the analytical mode functions for modes nine through eleven. The agreement is very good, though the displacement patterns are under sampled. For modes 1-7 the agreement was even better. Because of the relatively light damping of the system, the analytical mode functions are almost purely imaginary, so the real parts are not shown. The MAC, which gives a numerical indication of the linear dependence of two vectors, is commonly used for comparing analytical mode vectors with those obtained experimentally. The MAC between

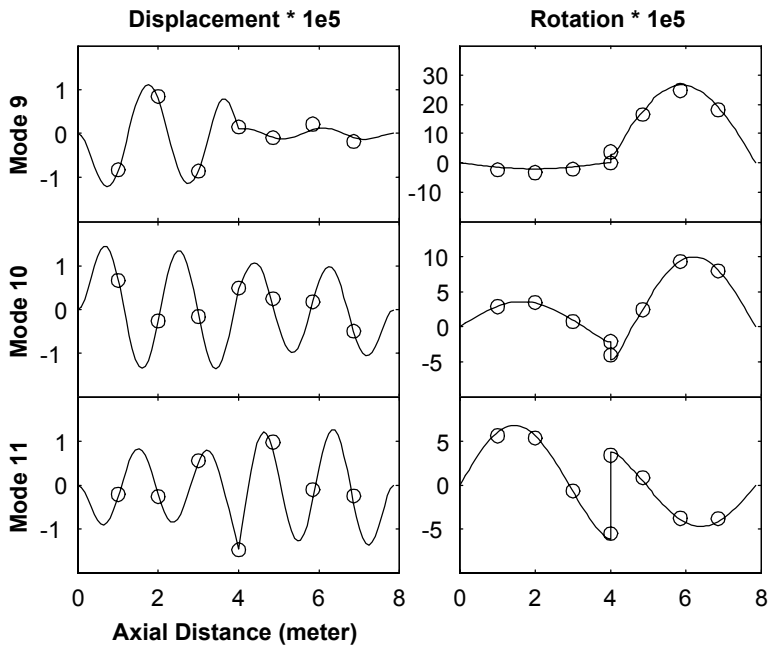

Figure 9: SIMO-AMI results for 65k point frame data. Imaginary parts of AMI mode shapes (o) and analytical mode functions (-) for modes 9-11.

mode vectors m and n is defined as

$$MAC = \frac{\{\psi_m\}^H \{\psi_n\} \{\psi_n\}^H \{\psi_m\}}{\{\psi_m\}^H \{\psi_m\} \{\psi_n\}^H \{\psi_n\}}. \tag{44}$$

Its value can range from zero, indicating no correlation, to one, indicating perfect linear dependence of the vectors. Because the displacement and rotation portions of the mode vectors represent fundamentally different variables, and are scaled differently as evidenced in Figure 9, the MACs between the analytical and experimental mode vectors were calculated using the displacement and rotation parts separately. For the displacement portion of the mode vectors, the MAC between experimental and analytical mode vectors was above 0.999 for modes 1-7. For modes 9-11 the values were 0.960, 0.971 and 0.966. The MACs for the rotation portions of the mode vectors were even higher.

3.1.1.1 SSI Applied to SIMO Frame Data

The Stochastic Subspace Identification algorithm of Van Overschee and De Moor [77] was also used to process the noise contaminated analytical data for the L-shaped frame. The SSI algorithm was included in the software tools supplied with [77] implemented in the

function "subid.m." The algorithm was explored extensively by the author in order to assure that good results were obtained. For more detail, see [18] or [77]. SSI begins by arranging the data into a large Hankel matrix. The R-factor in a QR decomposition of this Hankel matrix is found, following which a singular value decomposition of the R-factor is computed. The Hankel matrix has $2N_{br} * N_o$ rows, where the number of block rows N_{br} in the Hankel matrix is a user specified parameter, and the number of columns must exceed the number of rows. The algorithm used in this work required the Hankel matrix to be formed in memory. Good results could be obtained using the limited memory available only if the impulse responses were truncated. As a result, only the first 8192 points of the time domain impulse response were processed. The algorithm documentation suggested a formula for determining the number of block rows to use: $N_{br} = 2 * (maxorder) / (\#outputs)$, where $maxorder$ is the maximum model order to be estimated and $\#outputs$ is the number of outputs. For 11 modes and 15 outputs as in this problem, $N_{br} = 3$. Trial and error indicated that the algorithm performed poorly unless many more block rows ($N_{br} \geq 32$) were used. Analyses were performed on a machine with 768 Megabytes of RAM. The memory available in Matlab limited the number of block rows to slightly over 64.

In [4] the effect of the number of block rows used in SSI was explored in detail. The variation of the eigenvalues as a function of model order for a fixed number of block rows was also presented. It was found that for $N_{br} \geq 16$ very clear stabilization diagrams were obtained, though many more block-rows were needed to obtain accurate results, especially for the damping ratios. The close modes 8 and 9 were distinctly identified only for $N_{br} \geq 32$. This is illustrated in Figures 10 and 11, which show the stabilization diagrams for 16 and 32 block rows. The composite FRF is overlaid for reference. The stabilization diagram for 16 block rows shows modes that are consistently identified from one model order to the next, and few spurious poles are visible. However, only one mode has been identified near 2500 rad/s, where modes 8 and 9 are situated. The stabilization diagram for 32 block rows correctly identifies two modes in the vicinity of 2500 rad/s, yet it is not significantly clearer than the stabilization diagram for 16 block rows. In [4], Allen and Ginsberg noted that SSI's results tended to exhibit a bias error that was essentially constant with model

order in SSI's results, suggesting that a convergent stabilization diagram is not necessarily an indication of accurate results. In what follows, only the results for $N_{br} = 64$ will be presented, which were the best results obtainable by the algorithm with the limited memory available. A stabilization diagram for $N_{br} = 64$ is shown in Figure 12. As shown in [4], the spurious poles are easily identified as they have higher damping ratios than the true poles. Note that the model order plotted is the number of underdamped modes in the SSI fit, or 1/2 the size of the state space $[A]$ matrix.

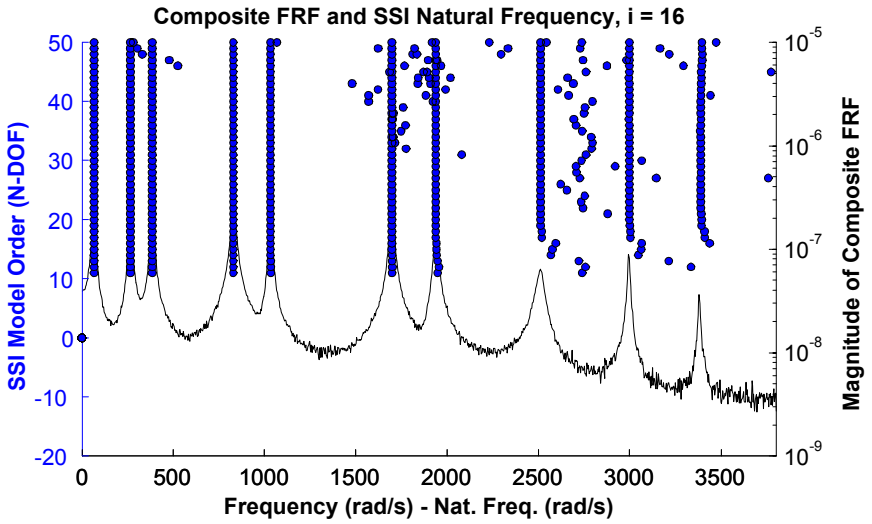

Figure 10: SIMO Frame Data: Stabilization diagram for SSI algorithm with 16 block rows and composite FRF. SSI fit the time domain data directly; the compoiste FRF is shown only for reference.

SSI identified all modes in the frequency range of interest, including the highly localized, weakly excited mode 8, but doing so required that the model order exceed 20. Recall that 21 modes were used to construct the analytical impulse response, and that the time domain data processed by SSI was not filtered to limit the effect of modes outside of the band of interest. Table 4 shows the error in the real and imaginary parts of the eigenvalues found by both SIMO-AMI and SSI. (Errors in the natural frequency and damping ratio are comparable to the errors in the imaginary and real parts respectively.) Both algorithms are quite accurate for the first 7 modes, where the FRFs are quite clean, with SIMO-AMI's errors usually being significantly less than SSI's. However, SSI identified mode 8, and more

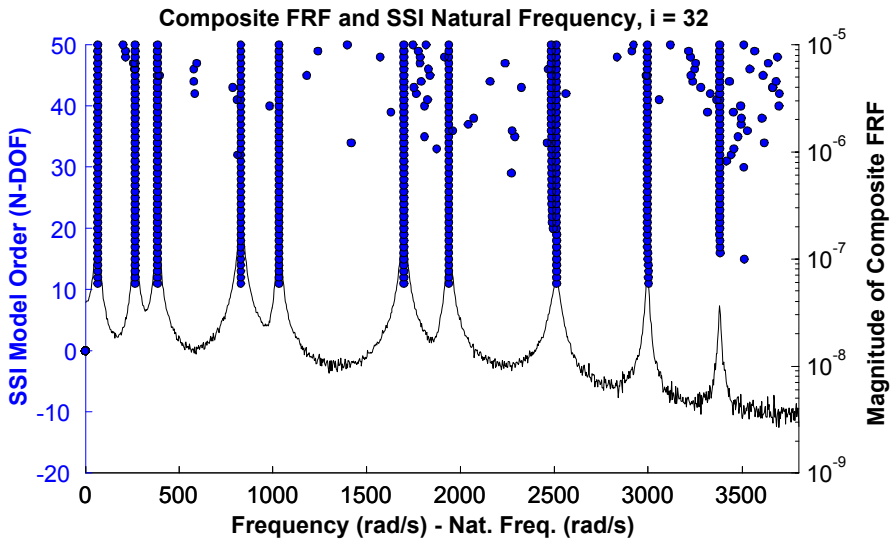

Figure 11: SIMO Frame Data: Stabilization diagram for SSI algorithm with 32 block rows and composite FRF.

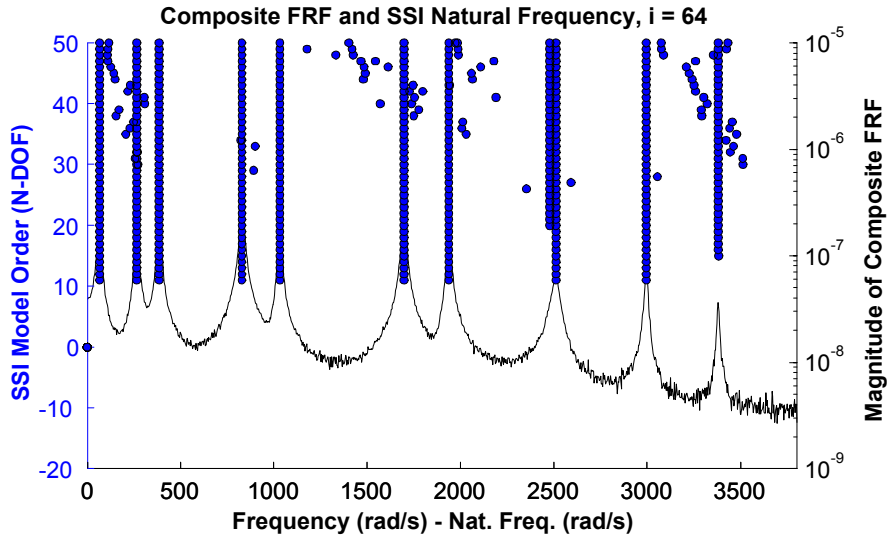

Figure 12: SIMO Frame Data: Stabilization diagram for SSI algorithm with 64 block rows and composite FRF.

accurately identified the real parts of the 9th and 10th eigenvalues, and both parts of the 11th eigenvalue. When compared to the peak picking method, SSI's eigenvalues were an order of magnitude more accurate on average, though the errors for some of the specific modes were comparable between the two methods.

Table 4: Errors in Eigenvalues, SIMO-AMI and SSI

	SIMO-AMI (65,536 Points)		SIMO-AMI (8,192 Points)		SSI ($i = 64$) $N = 21$ modes	
Mode	**Re**	**Im*1000**	**Re**	**Im*1000**	**Re**	**Im*1000**
1	0.04%	0.01%	0.04%	0.08%	-0.24%	5.79%
2	0.01%	-0.01%	-0.27%	-0.39%	-3.27%	-0.71%
3	-0.07%	0.07%	-0.03%	0.20%	0.23%	0.002%
4	0.04%	0.01%	0.05%	-0.08%	-1.51%	-0.36%
5	0.05%	0.03%	0.29%	0.15%	-1.07%	-0.55%
6	0.08%	-0.02%	0.33%	-0.01%	1.96%	0.35%
7	0.17%	-0.97%	-0.34%	-0.38%	1.59%	0.34%
8	missed	missed	52.37%	-26.87%	13.16%	111.48%
9	9.85%	19.34%	1.21%	5.54%	-0.14%	-3.93%
10	4.61%	-1.67%	0.74%	1.41%	0.92%	7.03%
11	27.97%	2.92%	5.15%	-3.95%	10.22%	16.45%

SSI's mode shapes appeared visually very similar to those presented in Figure 9. Although mode eight was identified by SSI, it's mode vector only resembled the analytical mode in the rotation portion. Note that the SSI algorithm is output-only, so the mode vectors returned by SSI are not scaled according to the definition used in deriving eq. (7). The MAC gives an indication of the correlation between two vectors that is independent of the scaling of the individual vectors. The MACs between the unscaled displacement mode vectors found by SSI and the analytical ones were above 0.999 for modes 1-7. For modes 8-11 the values were 0.208, 0.942, 0.988 and 0.988. For the rotation portions the MAC values were above 0.999 for all modes except mode 8, for which the MAC value was 0.971.

3.1.1.2 Analysis of Truncated Data Set with SIMO-AMI

As discussed earlier, SSI processed only the first 8192 samples of the noise contaminated impulse response. In contrast, the FRFs that AMI processed were obtained from an FFT applied to 65,536 samples of the noisy impulse response. The longer time record processed by AMI was selected to reduce leakage in the FFT for the slowly decaying, low frequency modes. However, the high frequency modes (8-11) have much larger real parts (see Table 1,) and thus decay quickly. The consequence is that use of a time record long enough to allow the low frequency modes to decay amplifies the effect of noise in the FFT for the high frequency modes, because at later times their contributions have decayed to below the noise

floor. To ascertain the degree to which AMI was handicapped relative to SSI by using data from a long time window, FRFs resulting from an FFT applied to the first 8192 samples of the impulse response, denoted 'short record FRFs' in the following, were also processed by AMI. This allows for the performance of the algorithms to be compared on the exact same data set, and hence is intended to provide a more fair comparison. Some leakage was present in the FRFs processed by AMI. At the end of the record the impulse response had decayed on average to only 40% of it's initial amplitude. In the full 65,536 sample record the response decayed to 5% of it's initial amplitude on average. As expected, the noise above 2000 rad/s is less severe for the short record FRFs.

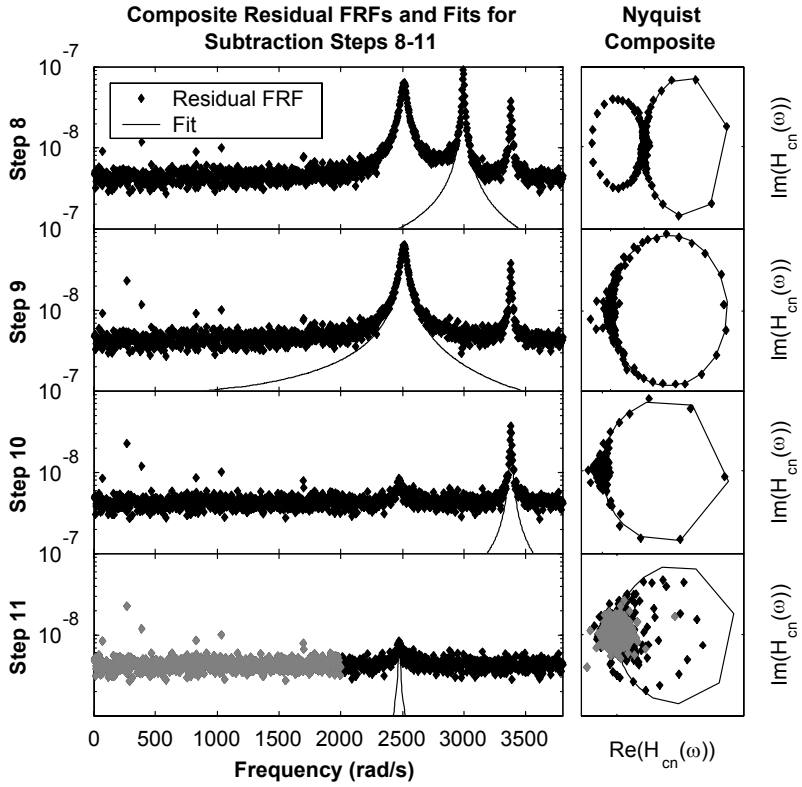

Figure 13: SIMO-AMI Subtraction steps 8-11 for short record (8192 samples) frame data set. LEFT: Composite residual FRFs (.) and fits (-). RIGHT: Nyquist composite plots of residual FRF data (.) and fits (-). The data shown in gray in the bottom panes was ignored in Step 11.

The last four subtraction steps for AMI on the short record FRFs are shown in Figure 13. Figure 7 described the same operation for the original FRFs. After the tenth subtraction

step a number of peaks are still evident in the data. Each of the peaks below 2000 rad/s is the result of small errors in fitting previously identified modes. Experience has shown that it is advisable to disregard these fitting errors during the subtraction stage, as they will usually disappear after mode isolation and refinement. One way of doing this is to zero the FRF data near each mode's resonant peak immediately after it is identified and subtracted from the data, as discussed in Chapter 2. This was not done here, although attempts at fitting any of the peaks below 2000 rad/s resulted either in unstable modes or modes that when subtracted from the data set did not reduce the magnitude of the FRF data within the fit band. For these reasons, all of the data below 2000 rad/s was neglected during the 11th subtraction step, bringing the peak near 2500 rad/s into dominance. This peak is outside of mode nine's half-power bandwidth (Step 9 in Figure 13,) suggesting that is it indeed due to a distinct mode. The data near 2500 rad/s is fit with only fair accuracy, though the Composite Nyquist plot (or alternatively a standard Nyquist plot for a well chosen response point) shows a definite arc, indicative of a true mode. After this mode is subtracted the data appears totally incoherent, so AMI proceeds to mode isolation. Convergence is obtained after 29 iterations. The errors in the resulting eigenvalues are shown in Table 4. Eigenvalues eight through eleven have improved considerably when compared to the results of processing the full 65,536 sample record. On the other hand, the errors in the real parts of modes 1-7 have increased, though they remain smaller than those for SSI.

Mode vectors 9-11 obtained from the short record FRFs appeared similar to those shown in Figure 9. As observed with SSI, the eighth mode vector found by AMI only resembles the analytical mode vector in the rotation portion. The MAC values for the displacement portions of modes 1-7 were all above 0.999, as they were when the 65,536 sample record was processed. For modes 8-11 the values improved considerably. The MAC values for modes 8-11 were 0.274, 0.966, 0.988 and 0.972 respectively for the displacement portions and 0.957, 0.998, 1.000 and 0.998 respectively for the rotation portions.

3.1.1.3 Monte Carlo Simulations - SIMO Frame Data

The results described thus far are for a single noise profile only. A Monte Carlo simulation was performed in order to obtain a characterization of the results that is independent of the random noise sequence applied to the impulse response. Towards this end, thirty normally distributed, zero-mean noise profiles were created, scaled to have a standard deviation equal to 1% of the maximum impulse response, and stored to disk so that the same noise profile could be used for both AMI and SSI. In this study SSI was applied as described previously to the first 8192 samples of the impulse response, with 64 block rows in the Hankel matrix. In each case, SSI used a model order of 42 (21 modes). Use of larger model orders did not result in a noticeable improvement. AMI processed FRFs derived from only the first 8192 samples of the impulse response.

A few initial trials indicated that when AMI was applied to the Monte Carlo data with $\alpha = 0.707$, (see eq. (27)), the data selected for fitting mode 9 fell in a frequency band that overlapped the band for mode 8. This led to a divergent situation when the algorithm proceeded to mode isolation. The divergence was recognizable by modes eight and nine converging towards nearly equal eigenvalues, with equal and opposite residue vectors that steadily increased in magnitude. Experimentation revealed that using $\alpha = 0.75$ reduced the frequency interval for each fit sufficiently to avoid this problem. This allowed the Monte Carlo simulations to be performed automatically by AMI.

The percent errors in the natural frequencies and damping ratios obtained in each trial are plotted in Figure 14. The distribution of these errors illustrates the bias and scatter of the algorithms. The scatter is characterized by the width of the distributions, higher scatter indicating that larger errors are possible for any single experiment. The center of the distributions defines the bias. A bias different from zero represents the average error obtained when the experiment is repeated a number of times. For modes 8-11 the algorithms gave comparable results, except that AMI shows a large bias error in the damping ratio for mode 8. AMI's estimates of the natural frequencies and damping ratios of modes 1-7 show much less scatter than SSI's. The bias errors of the two algorithms are comparable for modes 1-7, even though the FRFs processed by AMI showed considerable leakage error in

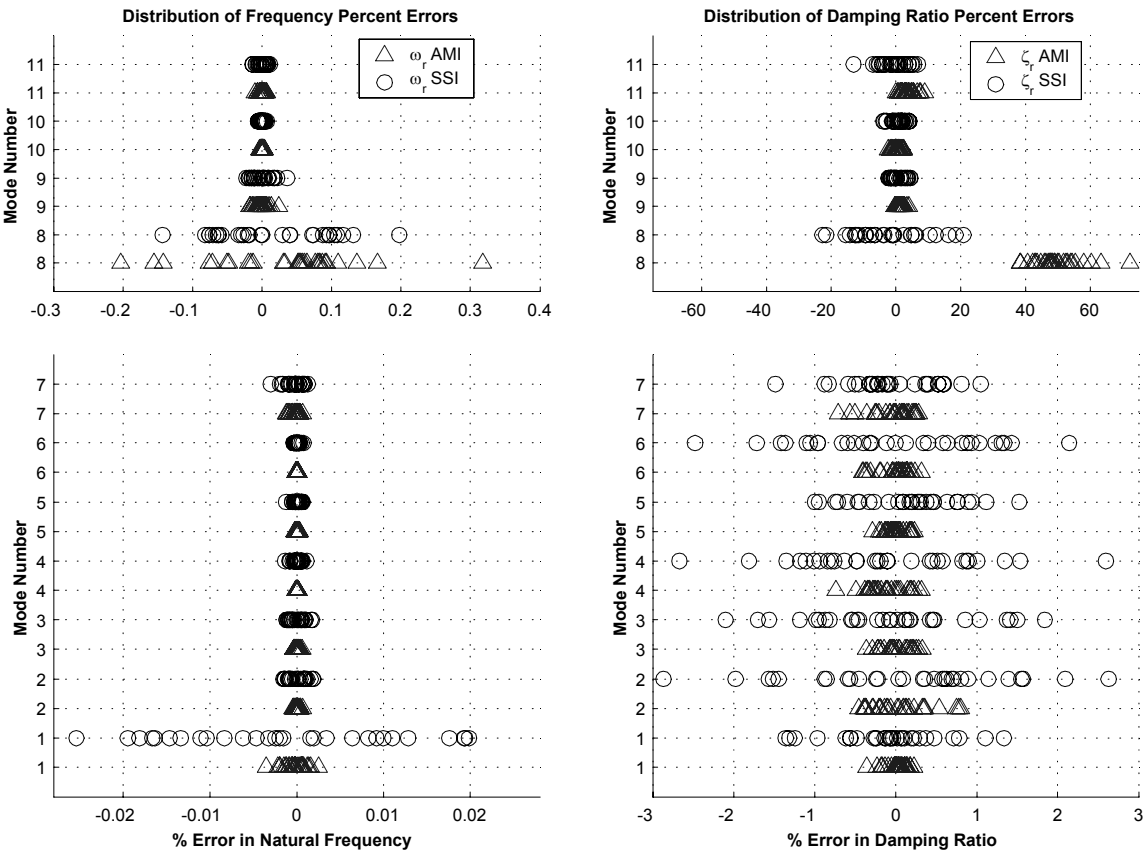

Figure 14: Monte Carlo Simulation Results for 8192 sample data from frame structure: Percent errors in Natural Frequency (left) and Damping Ratio (right) for SIMO-AMI (triangles) and SSI (circles) for each of thirty trials.

the peaks of these modes. On average, the standard deviations of SSI's estimates for the damping ratios of modes 1-7 were 6.7 times higher than the standard deviations of AMI's estimates.

The MACs between the analytical and experimental mode vectors for AMI and SSI had similar means and standard deviations for modes 8-11. For modes 1-7 AMI's displacement and rotation MACs had respectively 2.3 and 4.6 times higher standard deviations than SSI's on average, though all individual MACs for both algorithms were above 0.9995.

As reported in [4], when using the SSI algorithm, a very clear stabilization diagram is also obtained with 32 block rows in the data Hankel matrix. A Monte Carlo simulation using 32 block-rows in the SSI algorithm was also performed. The standard deviations of the natural frequencies and damping ratios of modes 1, 2, and 8 for the 32 block-row

case were more than twice those for the 64 block row case. The natural frequencies and damping ratios for most of the other modes had similar means and standard deviations for 32 and 64 block rows.

3.1.2 MIMO-AMI (Applied to data from two drive points)

Inspection of the mode functions for modes 8 and 9 of the frame system reveals that these modes are localized in their displacement portions to the second and first spans of the frame respectively. Thus, a single excitation applied to either span does not adequately excite both modes 8 and 9. As a result, excitation at two or more different points is needed to characterize both modes. This section presents the results of applying MIMO-AMI to data from the frame system for excitation at two drive points ($P_1 = 1$, $P_2 = 9$, see eqs. (7) and (40).) The data set used in the Monte Carlo simulations in the previous section, corresponding to excitation at the first drive point P_1, was augmented to include the response of the system for excitation at the second drive point P_2 as well. The combined data set was then processed using MIMO-AMI. The result of processing the data for the first of thirty noise profiles with AMI will be demonstrated, following which the results of a Monte Carlo simulation will be presented comparing the performance of MIMO-AMI and SSI. As was done in the previous section, the impulse responses were truncated to a length of 8192 samples to facilitate comparison with SSI.

Representative FRFs for this truncated, MIMO data set are shown in Figures 15 and 16. The high frequency modes (8-11) are fairly well represented in the rotation data, as typified by Figure 15, whereas their peaks are much smaller in the displacement FRFs, of which Figure 16 is typical. A single peak is evident in the vicinity of modes 8 and 9 in Figure 15, but the peak could be mistaken for the shoulder of an anti-resonance in Figure 16.

3.1.2.1 MIMO-AMI Results

After each mode is fit in the subtraction phase, the reduction factor RF is found according to eq. (35) in order to assess how well the FRFs reconstructed from the modal parameters identified in that subtraction step compare to the residual FRFs. Modes 1-7 yielded

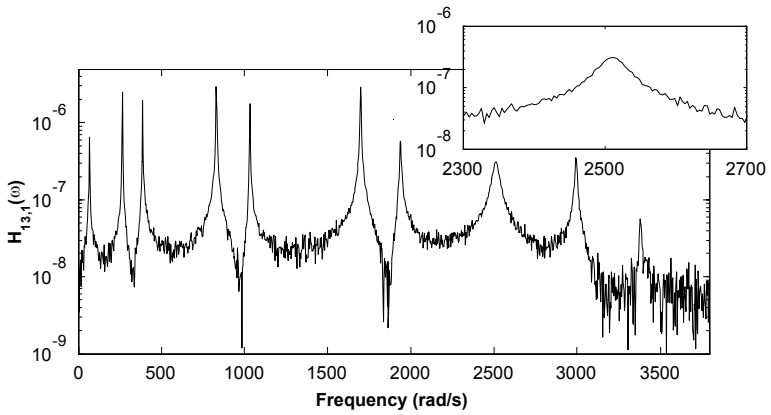

Figure 15: MIMO frame data: Noisy rotation FRF at 2 m from clamped support on beam 2.

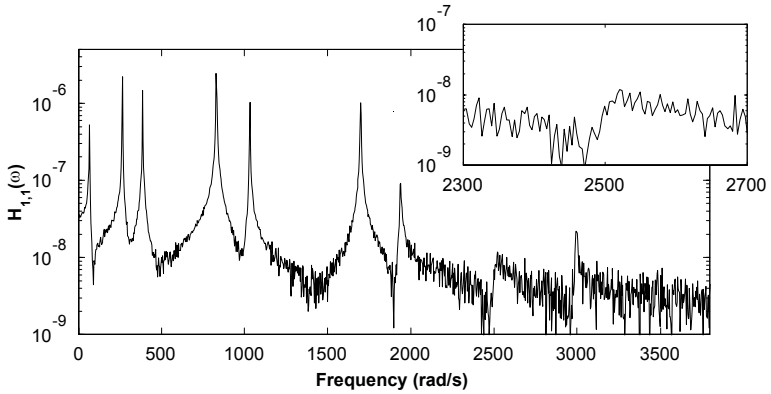

Figure 16: MIMO frame data: Noisy displacement FRF at 1 m from clamped support on beam 1.

reduction factors ranging from 45 to 385, indicating a very good fit to the data. For each of these modes, the second singular value ratio SR of the residue matrix was small, indicating that the residue matrix obtained from the SDOF fit was effectively rank-one.

The left panes in Figure 17 display the composite of the residual FRFs for subtraction steps 8 to 11. Composites of the FRFs constructed from the modal parameters identified in each subtraction step are also shown. On the right, composite Nyquist plots of the residual data and fit are shown. Mode 10 was identified in the eighth step with $RF = 5.9$ and $SR_2 = 0.03$. In the ninth step, an SDOF fit to the peak in focus resulted in $RF = 1.2$ and $SR_2 = 0.78$. (This is the peak where analytical modes 8 and 9 are situated.) Use

of the full rank residue when synthesizing the model resulted in a larger reduction factor. These indicators suggest that an additional mode is present at the peak. Two singular value ratios were found to be greater than 0.25, so a 2-DOF fit was attempted. Application of a 2-DOF fit using the SSI-FD algorithm resulted in $RF = 3.6$ for an FRF constructed from the two modes that resulted. Composite Nyquist plots are also shown in the right panes of Figure 17 for this subtraction step. The definition of the composite Nyquist data uses the residue matrix for a specific mode. Each mode identified at subtraction step nine has a distinct residue matrix, so a composite Nyquist plot was created for each. These are shown in the right panel in Figure 17 (solid lines,) where they are compared to the isolation residual FRF of the data, formed by subtracting from the measured FRF the contribution of all identified modes except for the mode in focus (see eq. (34)). Both the reconstructed and residual FRFs were condensed using the residue matrix for the mode in focus in eq. (33). This resulted in a reconstructed and residual Nyquist composite FRF for each mode. The Nyquist composites the tenth mode identified were multiplied by -1 and plotted in gray to aid in distinguishing them from those for the ninth. The composite magnitude plot reveals that the data has been reduced to noise in the vicinity of these modes, so use of an even higher-order fit is not warranted. Subtraction step ten led to identification of another mode, with $RF = 3.8$ and $SR_2 = 0.03$. As step 11 is initialized, the residual FRF obtained by subtracting the contribution of the modes identified in steps one through ten appears in the last pane of Figure 17. The data has been reduced to noise. Attempts to extract additional modes from this data result in modes with reduction factors below 1.0.

AMI next proceeds to the mode isolation stage. After three iterations in mode isolation the maximum change in either eigenvalues or residues was less than 0.001%. The eigenvalues and mode shapes found by AMI compared very well with the analytical ones.

3.1.2.2 Monte Carlo Simulations - MIMO Frame Data

A Monte Carlo Simulation was also performed for the MIMO data set, as described in Section 3.1.1.3. The errors in the natural frequencies and damping ratios obtained in thirty trials of MIMO-AMI and SSI are shown in Figure 18. The bias errors in Figure 18

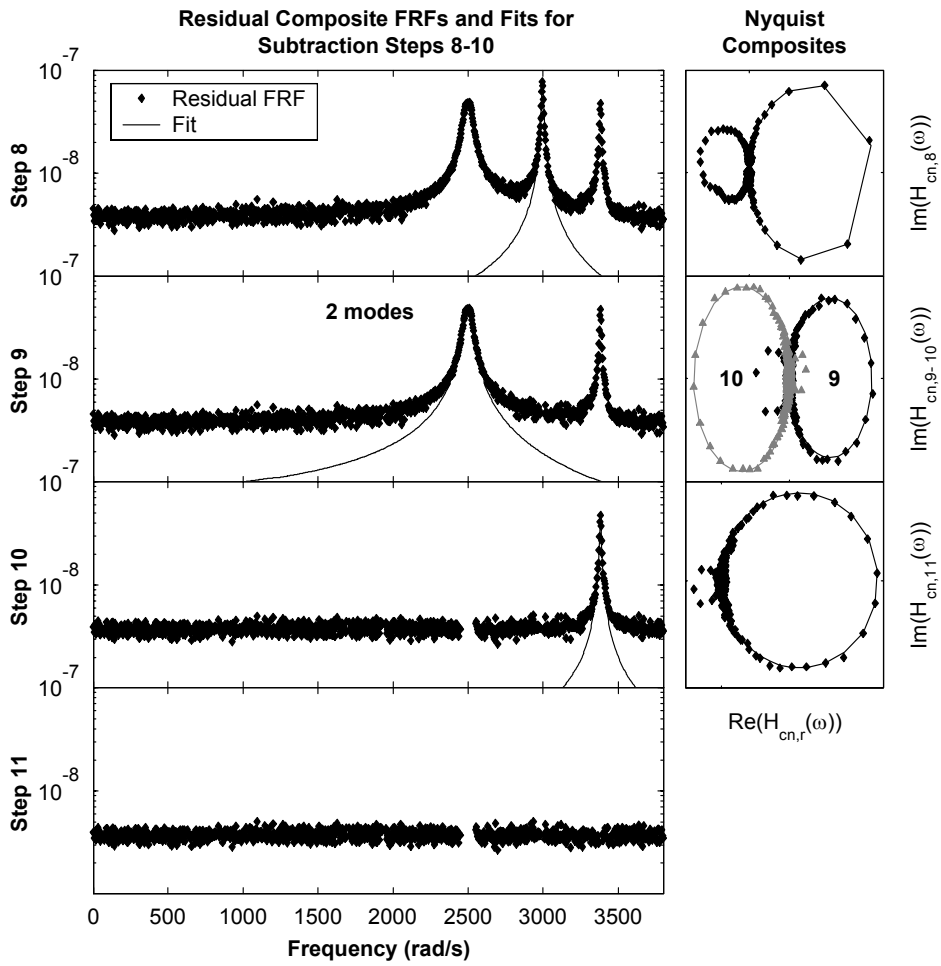

Figure 17: MIMO-AMI subtraction steps 8-11 for short-record frame data. Left: composite residual FRFs (.) and composite fits (-). Right: Composite Nyquist plots of residual data (.) and fit (-). Each composite Nyquist plot was created using the residue matrix for the mode in focus.

are generally smaller than the trial to trial scatter. Comparison of the results of MIMO-AMI with those presented in Figure 14 for SIMO-AMI show that the MIMO algorithm results in much more accurate results for the parameters of mode 8. This is due primarily to the fact that the additional input excites mode 8 much more effectively than the original input applied in the SIMO analysis. The parameters of the other modes show modest improvements.

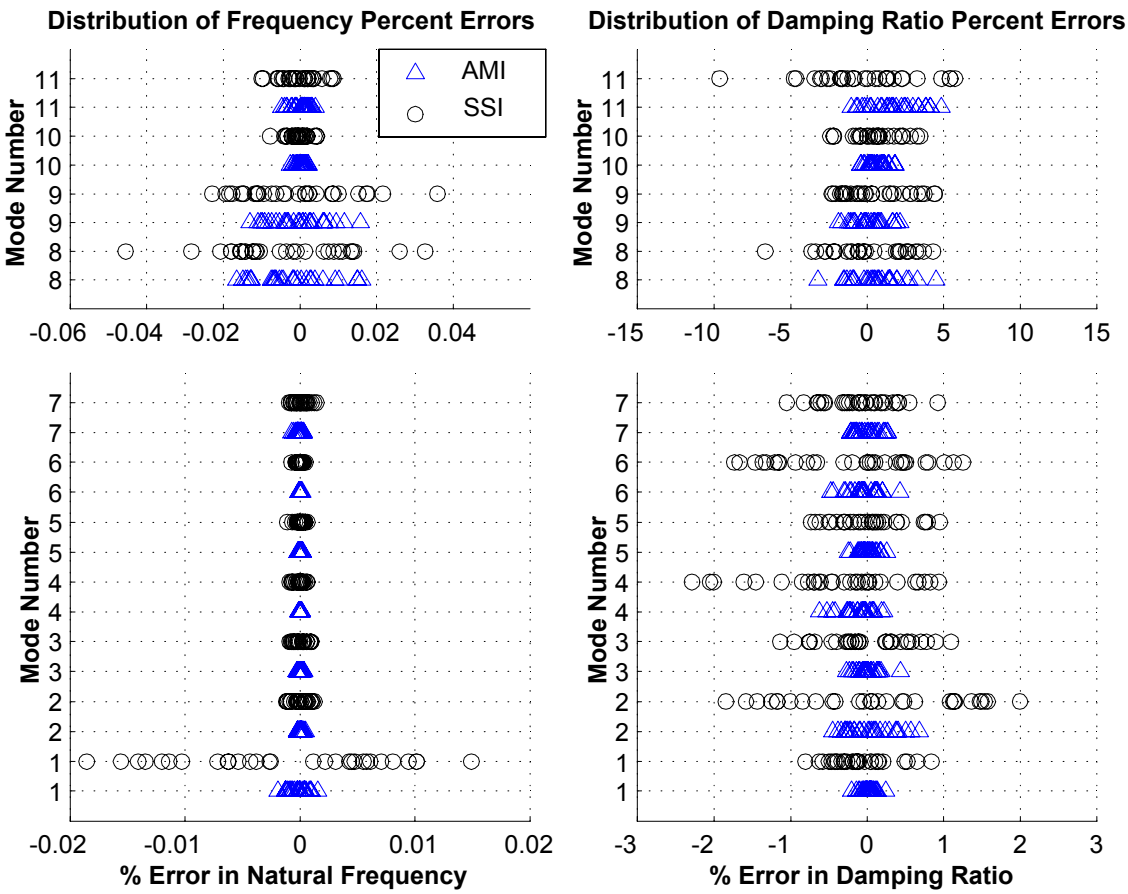

Figure 18: Result of Monte Carlo Simulation for Frame structure. Errors in Natural Frequencies and Damping Ratios for thirty trials of MIMO-AMI and SSI.

3.1.2.3 SSI Results

It was not possible to adequately process all of the MIMO data for the L-shaped frame using SSI because of the limited computer memory available. Furthermore, the SSI algorithm is formulated to process MIMO data in which the inputs are white, persistently exciting, and applied simultaneously, so there is no straightforward way of globally processing multiple sets of impulse responses using SSI. However, it is common to apply the SSI algorithm to simultaneously acquired subsets of a larger data set. For example, when the response of a structure at a large number of points is measured, it is common to successively collect a small subset of the measurements to minimize the number of sensors needed. Each patch of measurements is typically processed independently when the SSI algorithm is applied to

such a data set. The eigenvalues obtained from each patch are then averaged to obtain a global set. For example, this approach was used in [48]. In accord with this practice, SSI was applied to the set of all responses for each of the drive points separately. The application of SSI to data for the first drive point was presented in the previous section, in which sample stabilization diagrams were presented. The second drive point gave similar results.

Because the data from each drive point was processed independently, SSI gave two estimates for each eigenvalue for each trial in the Monte-Carlo experiment. A consequence of the localized nature of mode vectors 8 and 9 is that they were excited much more effectively, and thus were identified much more accurately, in the data sets for the second and first drive points, respectively. Standard practice would be to average the eigenvalues from each data-set, resulting in averaged eigenvalues for modes 8 and 9 that were less accurate than the estimates from a well chosen drive point. An experienced analyst might take note of the weak excitation of modes 8 and 9 in the first and second drive points, respectively, and choose to discard the estimates of each eigenvalue from the data set in which it was weakly excited. Correspondingly, in the results presented herein, SSI's eigenvalues from each drive point were averaged for all modes except 8 and 9. For modes 8 and 9 the eigenvalues from the drive point in which the mode was most strongly excited were retained. The resulting errors in the natural frequencies and damping ratios in each trial are plotted in Figure 18. It should be noted that simply averaging the results from each drive point for all of the modes resulted in 2-3 times greater scatter in the natural frequencies and damping ratios for modes 8 and 9 than that shown in Figure 18.

3.1.2.4 Discussion of Results

Overall, the results of the SSI algorithm compare quite well with those of the AMI algorithm for many of the modes. AMI results in considerably less scatter in the damping ratios for modes 1-7. AMI also gives much more accurate results for the natural frequency of mode 1 and somewhat more accurate results for the natural frequencies of modes 8-11. The results for most of the other modes are comparable. The AMI algorithm required significantly

less computation time than the SSI algorithm, and did not require the use of a stabilization diagram.

As mentioned earlier, when applying the SSI algorithm a key issue was using a large enough number of block rows in SSI's Hankel matrix. However, because the computational burden increases with the number of block rows squared, one might be reluctant to increase the number of block rows if it appears that adequate results have been obtained. It was noted earlier that clear stabilization diagrams were obtained from SSI when 16 or more block rows were used, although 32 block rows were needed to accurately distinguish modes 8 and 9, whose natural frequencies differ by less than their average half power bandwidth. The AMI algorithm showed less scatter in the identified natural frequencies and damping ratios, when compared to SSI applied using 64 block rows, the maximum allowable under the constraints of available memory. Finally, one should note that the fact that a clear stabilization diagram is obtained from SSI does not necessarily imply that good results have been obtained. The results obtained here suggest that the best practice might be to create a stabilization diagram for an increasing number of block rows, though this would increase the computational burden dramatically.

3.1.3 Application of Exponential Window to Frame Data:

In the preceding sections, AMI has been applied to FRFs created from truncated impulse responses (the first 8192 samples of the 65,536 sample responses). As discussed previously, this was done in order to obtain a one-to-one comparison with the SSI algorithm, because SSI was not able to process the full-length impulse responses using the limited computer memory available. However, truncating the impulse response resulted in significant leakage in the frequency response functions to which AMI was applied. Table 2 shows the modal decay constants for the first eleven modes of the frame. The decay constants for modes 7-11 are much larger than those for modes 1-6, indicating that the high frequency modes decay much more quickly than the low frequency modes. As a result, only the first six modes suffered from leakage, as the higher frequency modes had decayed sufficiently even within the truncated (8192 sample) record that leakage was not significant for them. Monte

Carlo simulations revealed that this leakage had a relatively small effect on the natural frequencies and damping ratios identified by AMI. However, some of the modal parameters were adversely affected by leakage in the FRFs, most notably the mode vector scaling. On the other hand, more accurate modal parameters were obtained for the high frequency modes when the data set was truncated. This was the case because the structure's response at high frequencies decays quickly, leaving only noise at those frequencies at late times. As a result, the noise level at high frequencies reduced when the data set was truncated.

These observations lead one to ask if better estimates of the parameters of the high frequency modes could be obtained by reducing the contribution of the late time data to the FFT. This could be accomplished without introducing leakage into the FRFs by using an exponential window. An exponential window is chosen because it's effect on the modal parameters can be completely accounted for; the exponential factor of the window simply adds to the modal decay constant. Specifically if an exponential window having an exponential window factor of a is used, which corresponds to multiplying the original response by $w(t) = \exp(at)$, the eigenvalues $\hat{\lambda}$ of the windowed response are given by

$$\hat{\lambda} = \lambda + a \tag{45}$$

where λ is the eigenvalue of unwindowed response. Thus the true eigenvalues can be found by subtracting the window factor from the eigenvalues identified from the windowed response. Note that for a typical exponentially decaying window, the factor a should be real, whereas the eigenvalue is complex, hence only the real part of the eigenvalue is affected by the window. The exponential window has no effect on the modal residue.

While exponential windowing has long been applied in signal processing, there are apparently no published results discussing the effect an exponential windowing has in decreasing the noise in FRF measurements, or discussing how windowing affects the accuracy of the identified modal parameters. In 1977, Brown and Halvorsen [11] presented the impact test for modal analysis, apparently including a discussion of exponential windowing. Later, Taber *et al* [72] discussed the application of exponential windowing to force and response signals for burst excitation. Their methods were also applied by [17]. Flaudung studied

impact excitation for modal analysis extensively at the University of Cincinnati in the late 1990's. Fladung and Rost [26] [27] discussed how to determine the optimum exponential factor to avoid leakage. They applied the rational fraction polynomial algorithm to estimate modal parameters from windowed responses and demonstrated that accurate modal parameters could be obtained from relatively short, exponentially windowed time responses. They also suggested using an exponential window that decays at approximately the same rate as the data to reduce noise, however they gave no explanation for this criteria. Cafeo and Tretheway [12] investigated the length of the time window needed to accurately estimate the modal parameters of simple systems using the least squares complex exponential algorithm in the absence of noise. Recently, Schwarz and Richardson [70] stated that "exponentially windowing is an effective way of reducing the noise in [FRF] measurements," although they gave no explanation or reference.

In light of the absence of such a study in the literature, this section presents the results of an investigation aimed at determining the optimum exponential factor to use in reducing noise, and quantifying the effect of the exponential window on the accuracy of the modal parameters identified. The following fourteen exponential factors were used in this study, [-0.049 -0.098 -0.16 -0.21 -0.26 -0.32 -0.37 -0.42 -0.49 -0.54 -0.75 -1.25 -2.0 -4.0]. For each exponential window a Monte Carlo simulation was performed consisting of thirty trials. In each trial the impulse response was contaminated with Gaussian white noise having a standard deviation of 1% of the maximum impulse response, as in the previous sections. The full, 65,536 sample impulse response was then windowed using an exponential window, following which the FFT yields the windowed frequency response function. MIMO-AMI was then applied to the windowed FRFs to estimate the parameters of the first eleven modes, as described in Section 3.1.2. These were corrected using eq. (45) and stored. This procedure was repeated for thirty different random noise sequences, and for each of the exponential factors listed previously.

Figures 19 and 20 show some typical results. In each figure the percent error in the damping ratio estimated in each of the thirty Monte Carlo trials is plotted versus the normalized exponential factor. The exponential factor has been normalized by dividing it

by the decay constant of the mode in focus, giving a normalized measure of the amount of damping that the exponential window has added to the mode in focus. For example, a normalized exponential factor of two indicates that the exponential factor is twice the modal decay constant, so that the decay constant identified from the windowed response should be three times the original value (see eq. (45).) Figure 19 shows that for mode 2, the errors in the damping ratio estimate became more widely scattered as the normalized exponential factor increased beyond one. For this mode, there was little change in the damping ratio estimate for exponential factors less than one. Vastly different behavior was observed for mode 11, for which the standard deviation of the errors in the damping ratio estimate remained essentially constant, while the mean error or bias of the estimate decreased with increasing exponential factor.

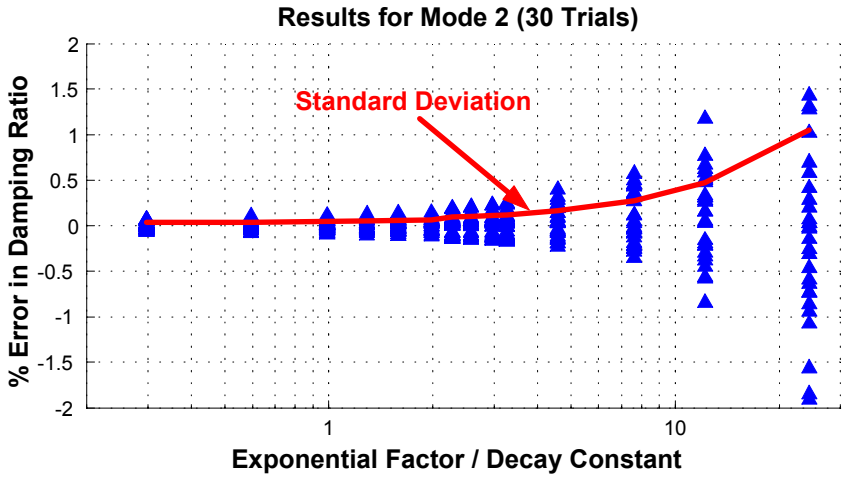

Figure 19: Percent error in MIMO-AMI's estimate of the damping ratio for mode 2 versus exponential window factor for thirty random noise profiles.

These alternate trends are typical of all of the modes, as illustrated in Figures 21 and 22. The left pane in Figure 21 shows the bias in the damping ratio error (i.e. the mean of the error over all 30 Monte Carlo trials) versus the normalized exponential factor; the right pane displays the associated standard deviation. Figure 22 presents the mean and standard deviation of the errors in the natural frequency estimate.

Figure 21 shows that the damping ratio errors of modes 8-11 behaved as illustrated in Figure 20, with the bias in the damping ratio error decreasing considerably with increasing

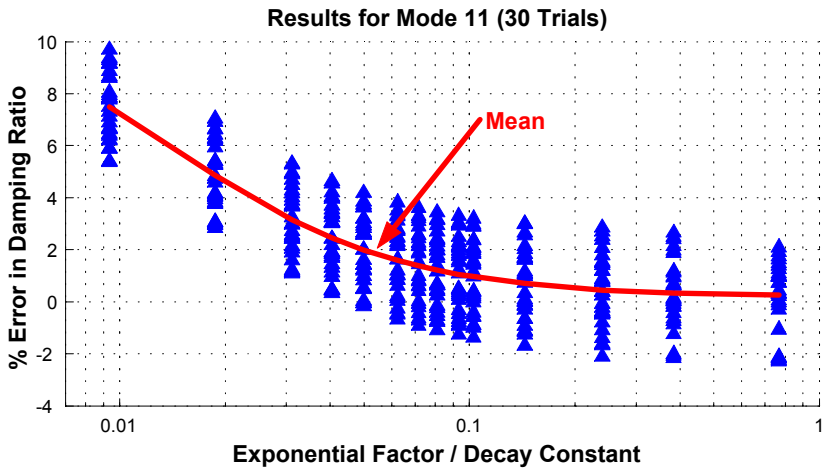

Figure 20: Percent error in MIMO-AMI's estimate of the damping ratio for mode 11 versus exponential window factor for thirty random noise profiles.

exponential factor, while the magnitude of the scatter remained constant. The damping ratio estimates for modes 1-7 had small bias errors, but the scatter in their errors became greater as the exponential factor became larger than the modal decay constant, as illustrated in Figure 19. Essentially the same phenomena are observed in Figure 22 for the bias errors in the natural frequency estimate.

3.1.3.1 Discussion

The presence of bias in the eigenvalue estimates is not surprising. This is a common phenomena in identification due to squaring of the data in the least squares solution, as discussed by Pintelon and Schoukens [60]. A number of algorithms have been suggested for eliminating this bias [14] [35]. One should also recall that because a Hybrid approach was employed to fit the data at the resonant peaks, modes 8 and 9 were identified simultaneously using the frequency domain subspace algorithm while the remaining modes were identified individually using the common-denominator, least-squares / total-least-squares algorithm described in Chapter 2. The frequency domain subspace algorithm was formulated to yield asymptotically unbiased estimates of the system parameters so long as the disturbing noise obeys the proper assumptions [76]. When comparing the least squares and subspace algorithms, one should note that a reduction in bias error often comes at the expense

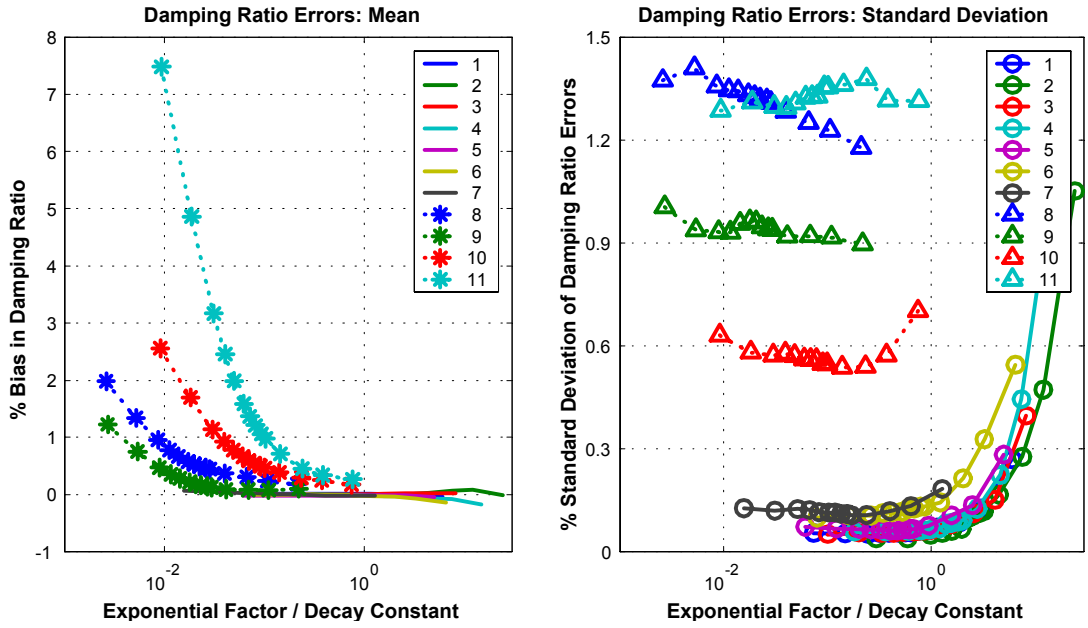

Figure 21: Mean and Standard Deviation of the Errors in the Damping Ratio Estimate Over 30 Trials.

of increased scatter error [60]. The data in Figures 21 and 22 show that modes 8 and 9 exhibited different behavior than the rest of the modes. In some other studies not presented here, the author found that when the subspace algorithm was used to identify the parameters of the distinct modes as well (modes 1-7 and 10-11), the modal parameters showed significantly more scatter than when the least squares algorithm was used. On the other hand, the different behavior of modes 8 and 9 could also be due in part to the closeness of the natural frequencies of these modes.

The bias errors in least squares identification are typically inversely proportional to the signal to noise ratio of the data. As a result, one might expect the bias errors for modes 1-7 to be small relative to those for modes 8-11, reflecting the difference in their signal to noise ratios. The fact that the bias errors for modes 8-11 decrease with increasing exponential factor suggests that the exponential window has increased the signal to noise ratio for these modes.

Variance errors are also typically inversely proportional to the signal to noise ratio of the data. These were observed to remain essentially constant for modes 8-11, while increasing

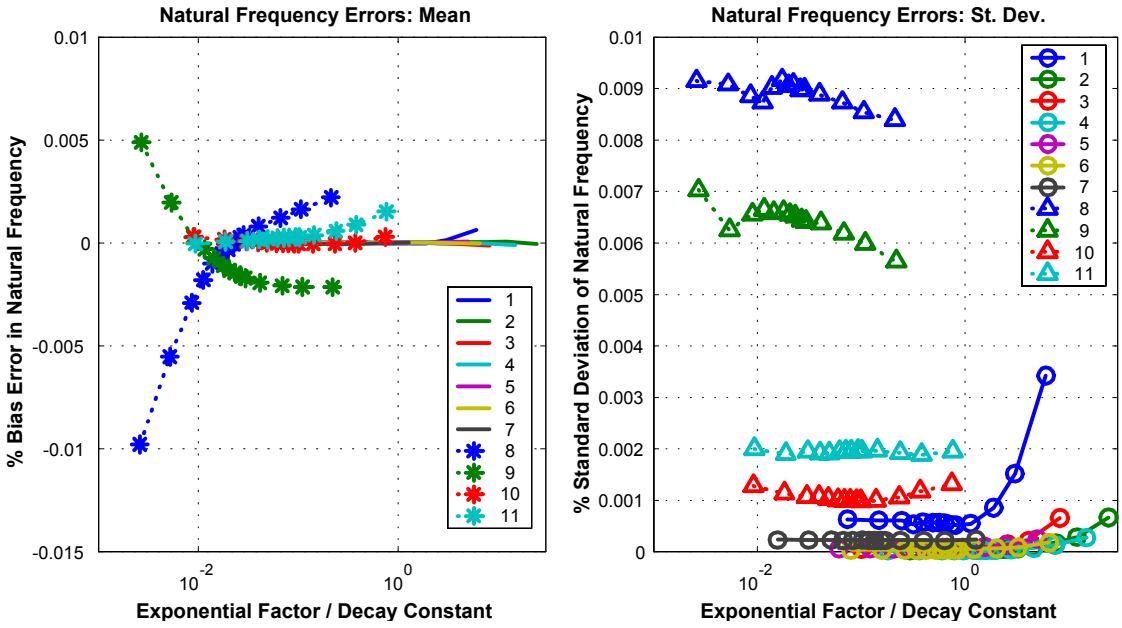

Figure 22: Mean and Standard Deviation of the Errors in the Natural Frequency Estimate Over 30 Trials.

sharply for modes 1-7. The differing behavior for these two groups of modes might be explained in part by the fact that the fixed frequency resolution of the FRFs results in the frequency dependence of the modes at the low end of the spectrum being much more coarsely sampled.

These observations lead one to question whether a correlation can be discovered between the signal to noise ratio of the data in the vicinity of each mode, and the bias and variance errors observed in Figures 21 and 22. The exponential window affects the signal to noise ratio of each mode in two competing ways. The exponential window adds damping to the system thereby reducing the height of the peak response for each mode in the FRFs, yet it also reduces the amplitude of the noise in the FRFs. As a result the signal to noise ratio could increase or decrease when an exponential window is applied, depending on the relative importance of each of these effects.

Figure 23 shows the signal to noise ratio for each mode versus the normalized exponential factor. The signal to noise ratio was determined as follows. An FFT applied to the Gaussian noise signals alone (described in Section 3.1.1.3) confirmed that in the frequency

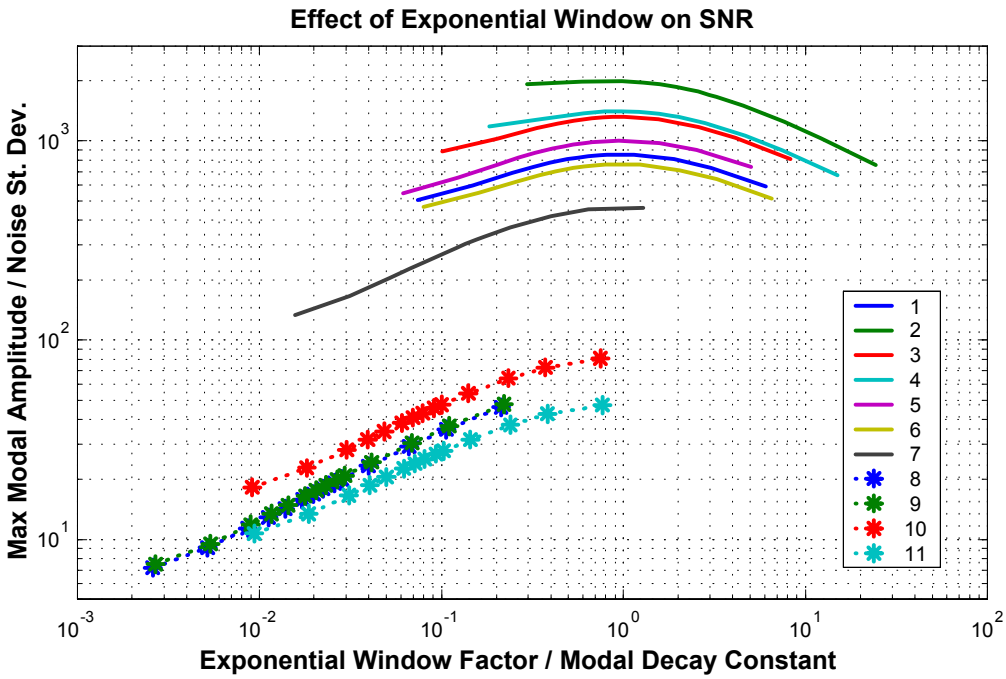

Figure 23: MIMO frame data: Signal to Noise Ratio versus Normalized Exponential Factor for Modes 1-11.

domain the noise was white and normally distributed, with the real and imaginary parts having approximately the same standard deviation (i.e. the standard deviation was computed by considering the real or imaginary part over all frequencies.) The noise level in the frequency domain was defined as the average of the standard deviation of the real and imaginary parts of the frequency domain noise profile. The signal level for each mode was represented by the maximum magnitude of the frequency response in the vicinity of the mode, averaged over all FRFs. Hence, the signal to noise ratio for each mode was different, even though the noise had the same amplitude at all frequencies. The vertical axis in Figure 23 corresponds to the signal level divided by the noise level using these definitions.

Figure 23 reveals that all modes behaved in approximately the same manner, their signal to noise ratios obtaining a maximum value when the exponential factor for the window was equal to the modal decay constant. This corresponds approximately to the rule of thumb given by Fladung and Rost [26]. This could explain why the scatter errors for modes 1-7 increased in Figures 21 and 22 when exponential factors larger than the modal decay

constant were used. Furthermore, one might have expected the error in the damping estimates to increase when large exponential factors are used because the damping of the system becomes and increasingly smaller portion of the damping identified by AMI when processing the windowed data. This would tend to magnify any errors in modal parameter estimation, the damping estimate being affected most dramatically.

The results presented in this section demonstrate that an exponential window can reduce the effect of measurement noise. It has been shown that when the noise is Gaussian with constant amplitude in time, it is reduced most significantly when the exponential factor of the window is approximately equal to the modal decay constant. The most significant effect of reducing the noise is to decrease bias errors in the estimate of the modal damping ratio. These results can be significant in many applications. For example, electrical noise and quantization error can often be well approximated as additive, Gaussian noise with constant amplitude in time. In such cases these results could be quite useful.

3.2 Application II: Simply-Supported Plate:

The closest modes in the frequency band processed for the frame problem, modes 8 and 9, were separated by 85% of their mean half-power bandwidth and were localized in their displacement patterns. As a result, either one mode or the other tended to be excited in a single FRF, and the SISO-AMI algorithm successfully identified both modes. Systems that have globally active modes with close natural frequencies present a different challenge because a given drive point is likely to excite both modes. As a result, the SISO approach is not likely to succeed in identifying the parameters of modes with globally active mode shapes and close natural frequencies. This section describes the application of MIMO-AMI to noise-contaminated synthetic FRF data for a simply-supported rectangular plate. The analytical solution for a simply-supported Euler plate yields the natural frequencies and mode functions of the plate. For simplicity, each mode was assigned a modal damping ratio of 0.02. The aspect ratio of the plate, a/b, was chosen to be 1.001, resulting in three pairs of very close modes in the frequency band of interest whose natural frequencies

were separated by 3%, 4% and 2% of their average half-power bandwidths. The SIMO-AMI algorithm fails to correctly detect these pairs of close frequencies. Using the Hybrid, MIMO-AMI approach, the frequency responses were processed semi-automatically, as will be described subsequently.

A nine by nine grid of uniformly distributed measurement points was assigned to the face of the plate, resulting in 81 total output locations. The analytical modal parameters were used to derive the velocity impulse response of the plate for excitation at three different locations. (The velocity response was used to mimic an experiment in which a laser pulse is used to excite the plate and a laser Doppler vibrometer is used to measure the plate's vibration.) For a plate having side lengths a and b in the x and y directions respectively, the drive points coordinates $[x, y]$ were, $[0.2a, 0.2b]$, $[0.3a, 0.7b]$ and $[0.6a, 0.7b]$. These drive points were chosen to ensure excitation of the first eight modes of the structure. Frequency was non-dimensionalized such that $\omega_{\text{nd}} = \omega a^2\sqrt{\rho h/D}$, where D is the flexural rigidity of the plate. The analytical mode functions are $\sin(n\pi x/a)\sin(m\pi y/b)$ where n and m are integers. The modes for indices n and $m \leq 5$ were used to generate the impulse response of the plate, resulting in 25 modes being included in the impulse response. This resulted in all modes having natural frequencies below $\omega_{\text{nd}} = 365$ being present in the response. Normally distributed Gaussian noise, scaled to have a standard deviation equal to 2% of the maximum in each response point, was added to the velocity impulse responses. The length of the time window was chosen to result in the most slowly decaying mode reducing to 10^{-5} of it's initial amplitude according to:

$$T_{\max} = \ln\left(10^{-5}\right) / \max(\text{Re}(\lambda)) = 29.133. \tag{46}$$

The sample increment $\triangle t = 0.003556$ and the number of samples $N_t = 8192$ were chosen assure that the Nyquist frequency was higher than the highest natural frequency of the system. After transferring the impulse response to the frequency domain, the analysis focused on a band of frequencies in which the lowest 8 modes of the plate were active. Figure 24 shows the response measured at the third drive point with excitation applied at the first, which typifies all FRFs. Figure 25 shows a composite FRF formed from all 243

FRFs.

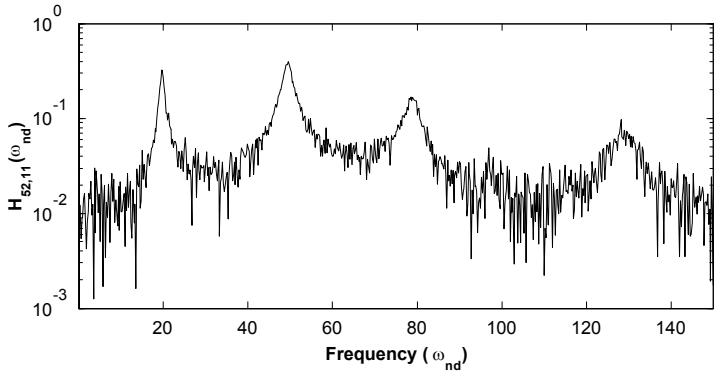

Figure 24: Plate data. FRF for the response at the third drive point with excitation applied at the first drive point.

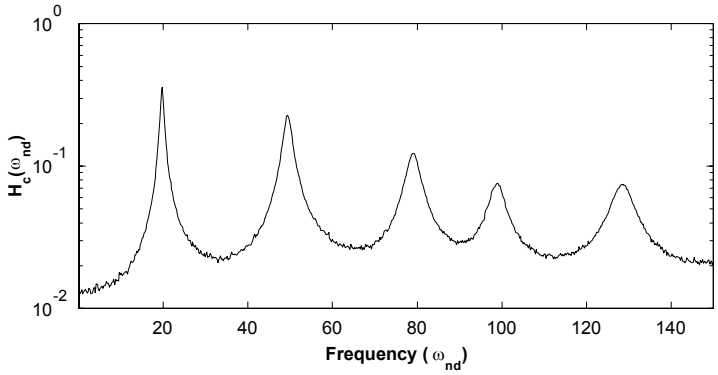

Figure 25: Plate data: Composite FRF

3.2.1 pLSCF Results

Because of the large number of output points used in the response, the memory and processing time required to accurately process this data with SSI exceeded available resource. For this reason, the FRFs were processed by the polyreference Least Squares Complex Frequency Domain (pLSCF) algorithm (See [73], [36] and [56]. The pLSCF algorithm is called the Polymax® algorithm in the LMS software package.) for comparison with AMI. The algorithm used here was written in Matlab by the author based on the information presented in the cited references. The pLSCF algorithm was tested on noise-free FRFs for the

plate response and found to give very accurate results, (i.e. errors on the order of 10^{-7} percent for the natural frequencies and 10^{-5} percent for damping ratios.) The pLSCF algorithm is a very fast algorithm capable of quickly processing data from a large number of sensors. It has received considerable attention because of its speed and because it tends to yield unambiguous stabilization diagrams. In [73] Van Der Auweraer *et al* presented an FFT technique to speed up creation of the normal equations, but that procedure was not used here. Doing so might reduce the processing time of the algorithm, but should not affect the final results.

A stabilization diagram created from the eigenvalues identified by pLSCF is shown in Figure 26. As expected, the algorithm returned a number of unstable modes (i.e. $\mathrm{Re}\{\lambda\} > 0$), and all of the stable modes in the frequency band of analysis appeared near the true natural frequencies. For convenience, dashed vertical lines are shown at the natural frequencies of the true modes of the system. The first four modes of the system, corresponding to the three left-most peaks in Figure 26 are identified reliably for model orders greater than 40. A higher model order is needed before the higher frequency modes stabilize, and a considerable number of spurious modes are identified before all of these modes are consistently identified. A magnified view would show pairs of close modes near $\omega_{\mathrm{nd}} = 50, 100$ and 130. As an example, a view focusing on the modes near $\omega_{\mathrm{nd}} = 100$ is shown in Figure 27. At model orders $69 - 90$, only two stable modes are found, indicating that the pLSCF algorithm has correctly determined the mode multiplicity in this frequency band. The scatter in the natural frequencies from one model order to the next is on the order of the separation between the frequencies. The scatter relative to the modal separation for the modes near $\omega_{\mathrm{nd}} = 130$ was worse than this, whereas that of the modes near $\omega_{\mathrm{nd}} = 50$ was less than their frequency separation. Clearly the accuracy obtained when using the pLSCF algorithm depends strongly on the model order, Figure 27 suggesting that the most accurate results are found for model orders greater than 69. The range of natural frequencies and damping ratios found by the pLSCF algorithm for model orders ranging from 69 to 90 is shown in Table 5. Higher model orders were also investigated, yet there was no significant improvement in the results. For example, when the data was analyzed with a maximum

model order of 120, similar levels of scatter were obtained, and the mode multiplicity at 100 and 130 rad/s was not correctly identified unless the model order exceeded 93. Hence, it appeared that no matter what maximum model order was used, reasonable results were only obtained for the 20-30 highest model orders.

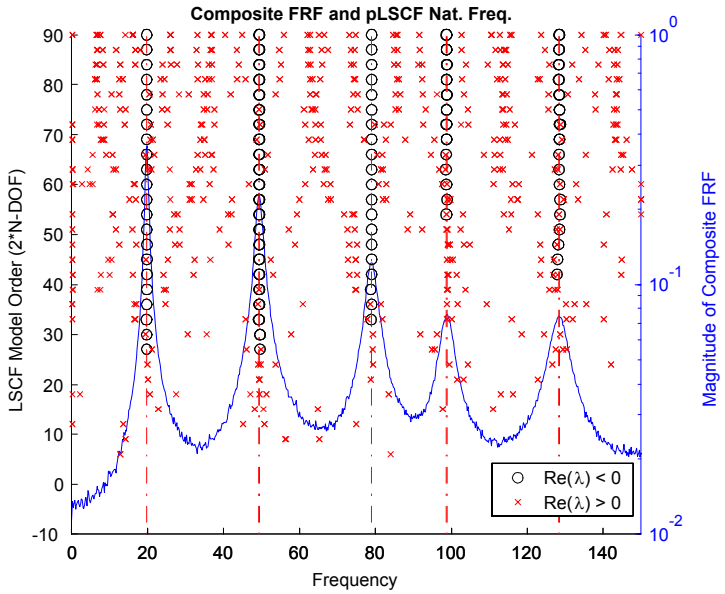

Figure 26: Plate data: Stabilization diagram for LSCF algorithm.

3.2.2 Hybrid, MIMO-AMI Results

AMI was also applied to the plate data. As for the frame system, a peak selection factor of $\alpha = 0.5$ was used. The subtraction process was automated for this analysis by attempting an MDOF fit at each peak for which the full-rank residue matrix resulted in a reduction factor greater than 3.0 and the rank-one residue resulted in a reduction factor less than 3.0. If these conditions were met, the number of modes fit at the peak was given by the number of singular value ratios greater than 0.25. All modes or sets of modes with reduction factors greater than 3.0 were retained. Subtraction halted when the full-rank residue matrix yielded a reduction factor less than 3.0. This approach resulted in five subtraction steps being performed, each of which obliterated one of the peaks in the composite FRF. At each peak containing a pair of close modes, the second singular value ratio was greater than 0.5, while the third singular value ratio was below 0.1, suggesting that a two mode fit was appropriate.

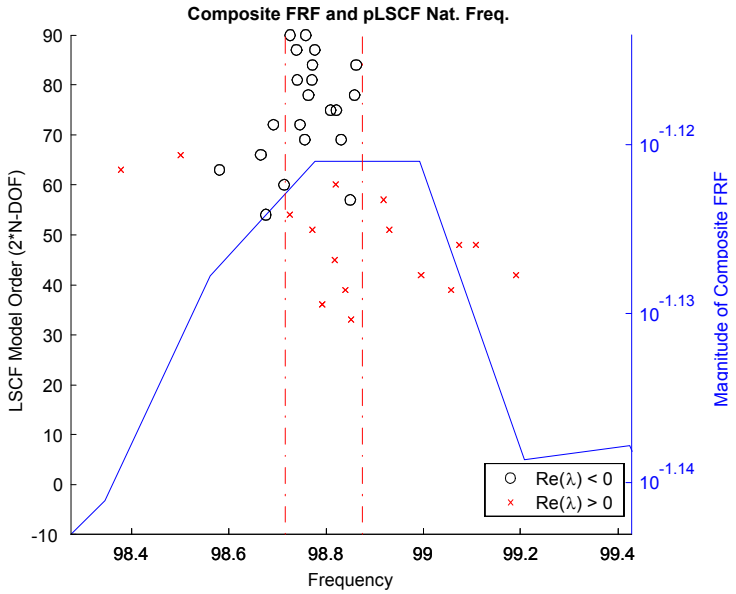

Figure 27: Plate data: Zoom view of stabilization diagram showing two close modes. The dashed (red) vertical lines show the true natural frequencies.

The subtraction phase resulted in initial estimates of the properties of eight modes, which is the number contained in the frequency band that was processed. Subtraction of these eight modes from the data left no coherent peaks. Five iterations in mode isolation phase were performed. In the last iteration the maximum change in either eigenvalues or residues was less than 0.001%. After mode isolation, the reconstructed FRFs for each individual mode, when viewed on a composite Nyquist plot, were found to agree more closely with the data than the comparable data at the conclusion of the mode subtraction phase. A similar comparison using a composite magnitude plot showed no noticeable change. Figure 28 shows magnitude composite plots of the noisy FRFs, AMI's reconstructed FRFs after the mode isolation phase, and a magnitude composite of the difference between the two. Table 5 compares the analytical natural frequencies and damping ratios with those found by AMI. The average errors in the natural frequencies and damping ratios found by AMI were respectively 0.006 % and 2 %.

Figures 29 through 33 show contour plots of the imaginary parts of the mode vectors found by AMI for each mode. Because a modal damping model was used, the real parts of each mode vector should be zero. The norm of the real parts of the mode vectors identified

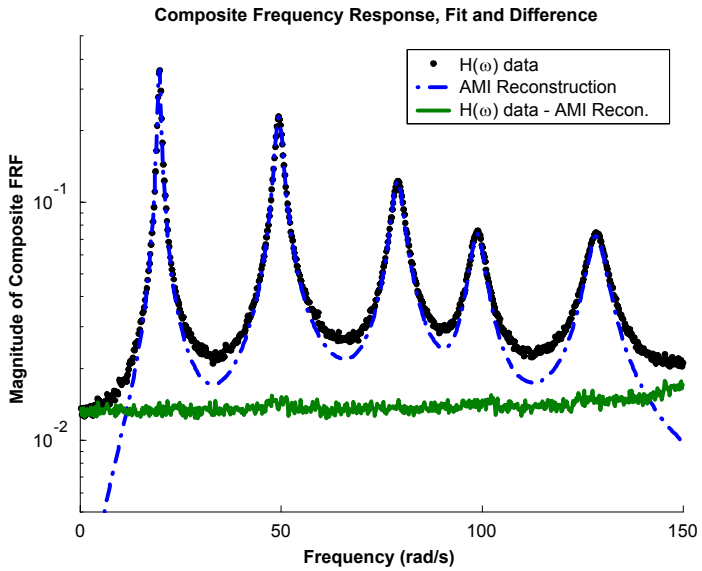

Figure 28: Plate data: Magnitude composites of the noisy FRF data, MIMO-AMI's reconstruction and the difference between the two.

by AMI divided by the norm of their imaginary parts gives a measure of the relative size of the real parts. For the distinct modes 1 and 3, the ratios were on the order of 1e-4, while the pairs of close modes gave ratios ranging from 0.01 to 0.13. Aside from these spurious real parts, the mode shapes shown in Figures 29 through 33 compare very well with the analytical ones, the analytical shapes being made up of various numbers of half sines in the x and y directions. Some distortions are visible, most notably in Figure 30 where the nodal lines for modes 2 and 3 are rotated slightly.

Table 5: Actual, AMI, and pLSCF Eigenvalues for First 8 Modes of Simply Supported Plate. *Range of values for pLSCF show the variation in each parameter for model orders from 69 to 90.

	Actual		**MIMO-AMI**		**pLSCF***	
Mode	ω_r	ζ_r	ω_r	ζ_r	ω_r	ζ_r
1	19.759	0.02	19.758	0.0199	19.756 - 19.762	0.0185 - 0.0189
2	49.3678	0.02	49.369	0.0202	49.349 - 49.373	0.0171 - 0.0183
3	49.427	0.02	49.421	0.0200	49.417 - 49.425	0.0185 - 0.0191
4	79.0358	0.02	79.029	0.0194	79.015 - 79.035	0.0172 - 0.0187
5	98.716	0.02	98.705	0.0191	98.692 - 98.809	0.00329 - 0.0160
6	98.874	0.02	98.855	0.0194	98.758 - 98.861	0.000426 - 0.0128
7	128.384	0.02	128.366	0.0195	128.22 - 128.52	0.00171 - 0.0171
8	128.483	0.02	128.508	0.0196	128.38 - 129.66	0.00279 - 0.0170

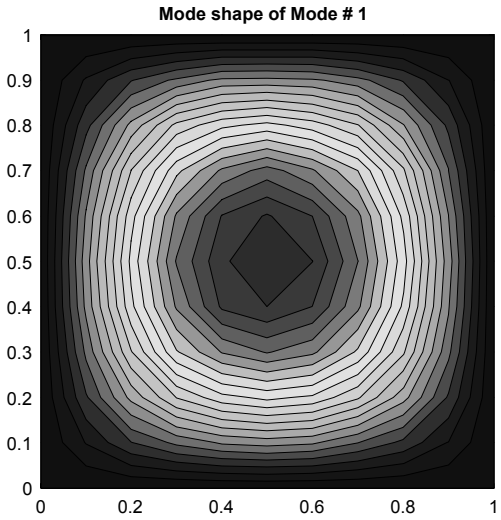

Figure 29: MIMO-AMI: Contour plot of the imaginary part of the first mode vector.

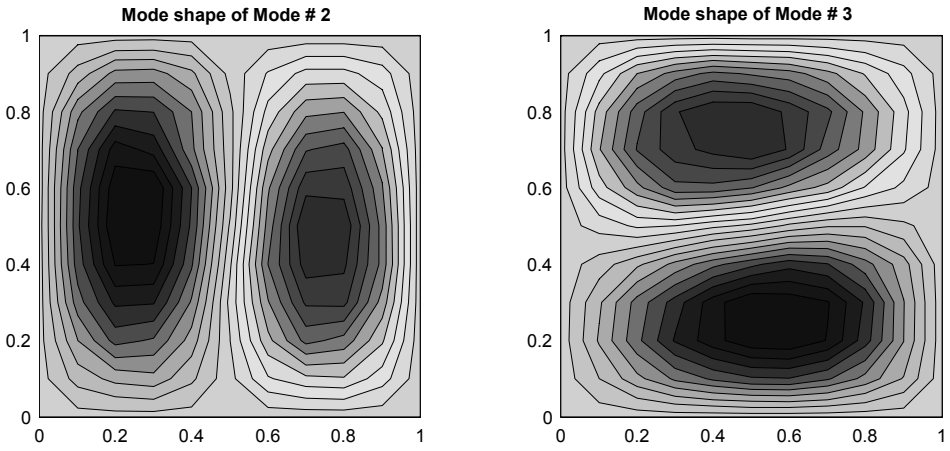

Figure 30: MIMO-AMI: Contour plot of the imaginary part of mode vectors two and three.

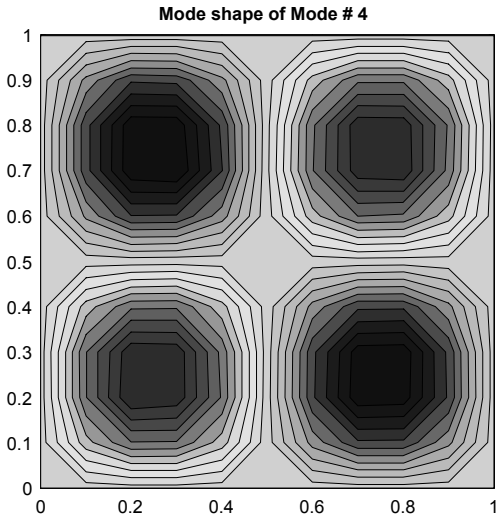

Figure 31: MIMO-AMI: Contour plot of the imaginary part of the fourth mode vector.

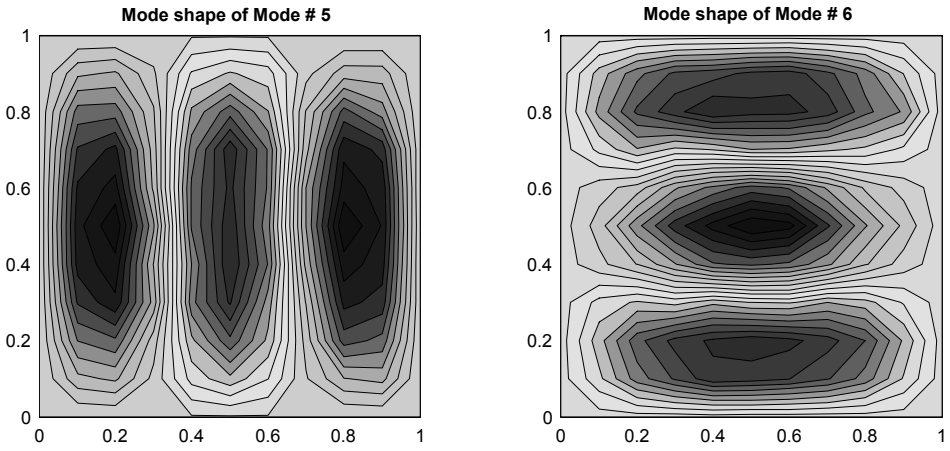

Figure 32: MIMO-AMI: Contour plot of the imaginary part of mode vectors five and six.

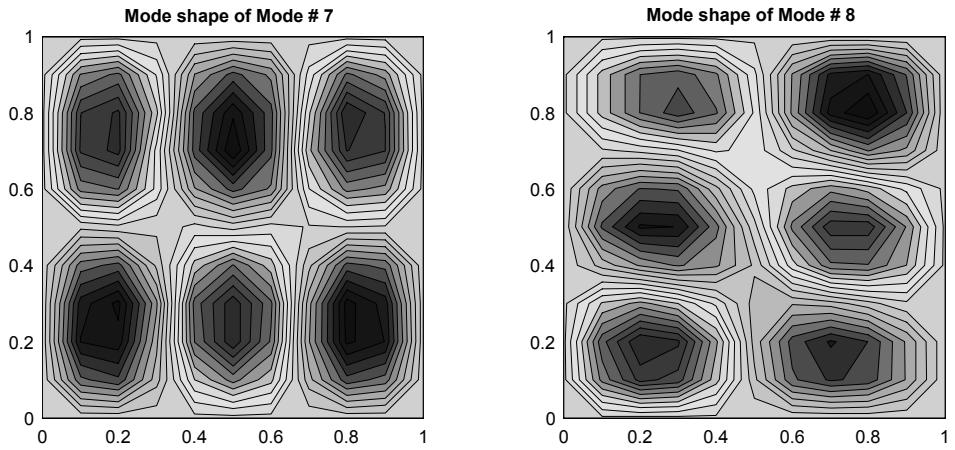

Figure 33: MIMO-AMI: Contour plot of the imaginary part of mode vectors seven and eight.

3.2.3 Discussion of Results

This test problem illustrated the performance of the MIMO-AMI and pLSCF algorithms on a data set with a relatively large number of FRFs. The individual FRFs for the rectangular plate were quite noisy, and would have been difficult to process using a SISO algorithm. However, because of the large amount of redundant information available in the total set of FRFs, global processing resulted in accurate estimates of the modal parameters. The pLSCF algorithm was shown to quickly identify the modes of the structure and accurately identify the number of modes dominant at each peak, although the scatter in the natural frequencies that pLSCF identified was larger than the separation between the analytical natural frequencies. While such small differences might not be of interest in all applications, they could be important in demanding applications, such as damage detection or inverse problems. Also, with the pLSCF algorithm there was no clear way of determining a priori which model order might result in the most accurate estimates of the modal parameters. Table 5 shows that relatively large errors were possible, depending on which model order was used.

In the results presented previously, the pLSCF algorithm was applied with a maximum model order of 90. It was noted that a range of maximum model orders were attempted,

each of which gave similar results. As the maximum model order increased, the minimum model order at which modes 5-8 were reliably identified also increased. Hence, the best results were always obtained by at the highest 20-30 model orders on the stabilization diagram. This might be explained by the fact that the pLSCF algorithm varies only the order of the denominator polynomial when forming the stabilization diagram. The order of the numerator polynomial kept constant, equal to the maximum order of the denominator polynomial. Apparently the best results are obtained when the numerator and denominator polynomials are of roughly the same order.

One can see in Table 5 that the pLSCF algorithm has consistently underestimated the damping ratios of the modes of the plate. In [15], Cauberghe *et al* discuss this difficulty claiming that, stated simply, it is a result of designing the pLSCF algorithm to yield clear stabilization diagrams. They suggest the use of an iterative maximum-likelihood version of the pLSCF algorithm [14] in cases where the experimental data is very noisy. Considering the relatively high noise in the data, this maximum-likelihood version of the pLSCF algorithm might have performed better for on the plate data, however an implementation of it was not available to the author.

This test problem involved a rectangular plate whose aspect ratio was very close to unity. If an aspect ratio of one were used, the pairs of closely spaced modes would have repeated frequencies and any linear combination of their mode vectors would also be a mode vector. In other words, the individual mode vectors would not be distinct. The aspect ratio was chosen to be sufficiently different from unity for the modes to retain their individuality, yet close enough to unity to make the identification of the character of the individual modes quite difficult. In a separate analysis not presented here, AMI was applied to synthesized data for a plate with an aspect ratio of unity. AMI correctly identified the mode multiplicity at each peak for this data set, and the resulting mode vectors were recognizable as linear combinations of the products of sines, as expected for a simply supported square plate.

3.3 Conclusions and Discussion of Results

The global SIMO and hybrid MIMO extensions to AMI were tested on two analytical systems in this chapter. The global nature of both algorithms facilitated processing data sets containing many FRFs (30 FRFs for the frame in Section 3.1 and 243 for the plate in Section 3.2,) quickly and with minimal user interaction. It is significant to note that either data set would have been very difficult to process using a SISO algorithm, because several modes had contributions that did not stand out above the noise in many of the FRFs. As a result some modes would have been missed or poorly approximated in many of the FRFs, and it would have been difficult to merge the eigenvalues found from each FRF to obtain a global set. For example, it was difficult to decide when to stop looking for modes when using the SISO AMI algorithm on the Frame data in [3]. In many of the FRFs one would come to a juncture in which one or more very noisy modal contributions appeared to be present in the data, although they might be difficult or impossible to extract from the data because they were dominated by noise. On the other hand, when using the global algorithm it was relatively easy to decide when to stop looking for modes; all modal contributions had been removed so the data appeared to be completely incoherent. When using the global algorithm, the natural frequencies and damping ratios of the structure were estimated globally, so there was no need to combine the results from different FRFs to obtain a global set. In all of these applications, the composite magnitude and composite Nyquist plots were found to be helpful in assessing the quality of the agreement between the measured and reconstructed FRFs for each mode identified, and in assuring that the proper number of modes was found in each frequency band.

The Hybrid identification approach employed in the MIMO-AMI algorithm, which consists of treating groups of modes with very close natural frequencies simultaneously in AMI, was validated here using the frame and plate data sets. In the case of the Frame data, careful application of the global, SIMO algorithm resulted in good estimates of the parameters of a pair of modes with close natural frequencies, without using the hybrid approach. The difficulties involved were discussed in Section 3.1.1. On the other hand, the close modes were robustly detected and their parameters accurately estimated using the hybrid,

MIMO algorithm. For the plate data, the parameters of three pairs of modes with close natural frequencies could not be estimated using the global, SIMO algorithm. The results of applying SIMO-AMI to data from the plate, were not reported here. However, the SIMO algorithm would fail to distinguish these close modes and instead identify three modes whose parameters were a linear combination of the parameters of each pair of close modes. It was shown in Section 2.1 that the hybrid, MIMO-AMI algorithm accurately identifies these modes, even in the presence of substantial noise.

Two metrics, the Reduction Factor RF and the ratio SR of the singular values of the residue matrix, were introduced to assist in making decisions when AMI was applied to the frame and plate data sets. These were used to determine the number of modes to be fit at each peak in the initial stage of AMI, in which modal contributions are subtracted from the data. Based on these metrics, the subtraction phase was performed automatically when AMI was applied to the plate data, though some intervention was required to process the FRFs for the frame system. The values for these parameters used in the preceding sections to automate the subtraction process work well for extracting the dominant modes from data for a variety of systems, though additional research is needed before all operations can be automated for an arbitrary system. Nevertheless, the modal properties of both test systems were accurately identified using MIMO-AMI with little user interaction. There was no need for a stabilization diagram. Furthermore, the number of modes in the frequency band was identified as part of the algorithm's operation. Also, the AMI algorithm was able to globally process all available FRFs very quickly because it uses low order fits restricted to data near the resonant peaks.

CHAPTER IV

EXPERIMENTAL APPLICATION: Z24 HIGHWAY BRIDGE

In this chapter, vibration data from the Z24 bridge in Switzerland is used to evaluate the performance of the global SIMO and hybrid MIMO implementations of AMI. The data analyzed in this chapter is available for download from the Katholieke Universiteit Leuven web-site *http://www.kuleuven.ac.be/bwm/IMAC/*. The analysis of two distinct data sets is presented in this chapter. The first section presents application of SIMO-AMI to impulse response data. The impulse response of the bridge was approximated by dropping a large mass onto the bridge and recording the decaying response of the bridge. The second section applies the hybrid MIMO-AMI algorithm to vibration data collected in shaker excited tests. A number of researchers analyzed these data sets and presented their results at the 19th International Modal Analysis Conference, see [25], [45], [48], [71], [70] and [80]. The results obtained by these researchers will be compared with those obtained by AMI. In his thesis [54], Peeters presents a detailed description of the bridge and data sets, as well as a good bibliography of other information regarding the Z24 bridge.

4.1 SIMO-AMI Applied to Drop Test Data

4.1.1 Data Description & Signal Processing

The data analyzed in this section is the result of dropping a large mass (approximately 100 kg) onto the bridge a number of times and recording the response with accelerometers. Because of the size of the bridge, the response was measured in nine setups with up to 15 sensors in each, with three sensors common to all setups. There were a total of 99 responses at 75 different locations. In most of the setups the mass was dropped four times.

The raw time histories containing the response to between two and four impulses were provided by KUL. These had to be converted to FRFs for processing with AMI. Because the excitation approximates an impulse, the (unscaled) FRFs can be approximated by the FFT of the response. The time series were broken into segments representing individual

impulse responses by triggering the signal from node 2 in the vertical direction (one of the reference sensors), resulting in a set of (usually) four impulse responses per time record. Node 2 was active in the response and near the excitation, and hence provided a good signal for the trigger. The individual impulse responses for each sensor were then truncated or zero padded to a length of 1024 samples. The FFTs for each 1024 length response found with a rectangular window were then averaged. This was performed for each setup resulting in a total of 99 frequency responses that were processed globally by AMI.

Globally processing all of the frequency responses allowed for all available information to be used when estimating the modal parameters. Because three sensors were common to each of nine setups, nine repetitions of the measurements for these sensors were available. These were retained as if they had been distinct measurement channels, so that the mode shapes could be 'glued' together in the following manner. If the frequency responses due to the drop excitation are assumed to be flat within the bandwidth of each mode, then the residues obtained for each mode would be proportional to the true residues, the unknown scaling being a function of the magnitude and phase of the impulse excitation. Because the triggering was not perfect, this scaling was different for different measurement setups, (though consistent for all responses of a given setup.) This was evidenced by the fact that if the FRFs for the non-reference sensors were processed globally, the resulting mode shapes had visibly inconsistent magnitude and phase from patch to patch. With the reference sensors retained as individual measurement channels, the residues found at the reference sensors in each setup could be used to find a scale factor for all residues of the same setup, resulting in consistently scaled mode shapes.

4.1.2 Analysis with AMI-SIMO

Initial tests on the Z24 data using the same peak selection factor $\alpha = 0.707$ used for the frame data in Chapter 3, Section 3.1.1 led to two difficulties. First, visual inspection of the peak data selected by the algorithm showed that often more than one peak was included in the frequency band, causing the SDOF fitting algorithm to give erroneous results. Second, a pair of modes was identified whose fitting bands overlapped significantly, resulting in

divergence of their modal parameters in the mode isolation stage. These problems could have been corrected by manually adjusting the fitting bands. However, use of a peak selection factor of 0.8 allowed for semi-automatic processing of the data. Furthermore, use of more data around the peaks did not appear to give a better fit for any of the modes. One extra numerator term (see eq. (17)) was used in all fits to account for out of band effects. Figures 34 and 35 describe the composite FRF and fit for eight subtraction steps. A composite Nyquist plot is shown to the right for each subtraction step.

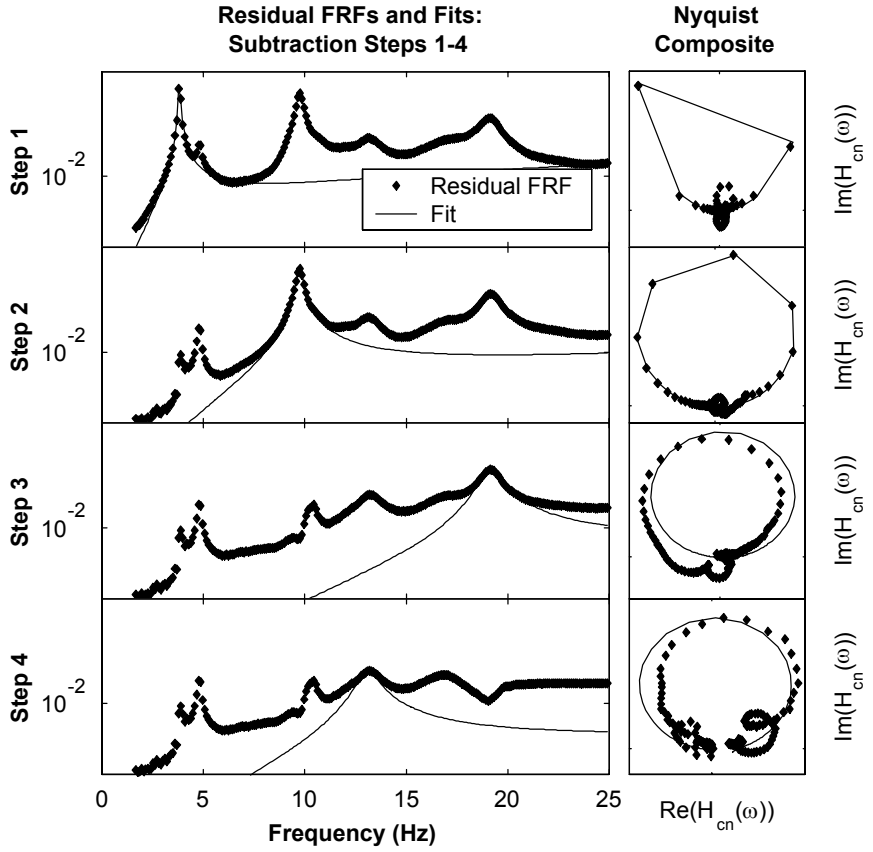

Figure 34: AMI Subtraction steps 1-4 for Z24 Bridge Data. LEFT: Composite residual FRF (.) and fit (-). RIGHT: Nyquist composite plots of residual FRF data (.) and fit (-).

When subtraction step eight is reached, data at the high frequency end of the frequency band becomes dominant. Visual inspection of this data suggests that it is due to out of band modes. For this reason, the high frequency data was nullified in the residual for subtraction step eight (shown lighter in Figure 35,) causing the peak near 12 Hz to come

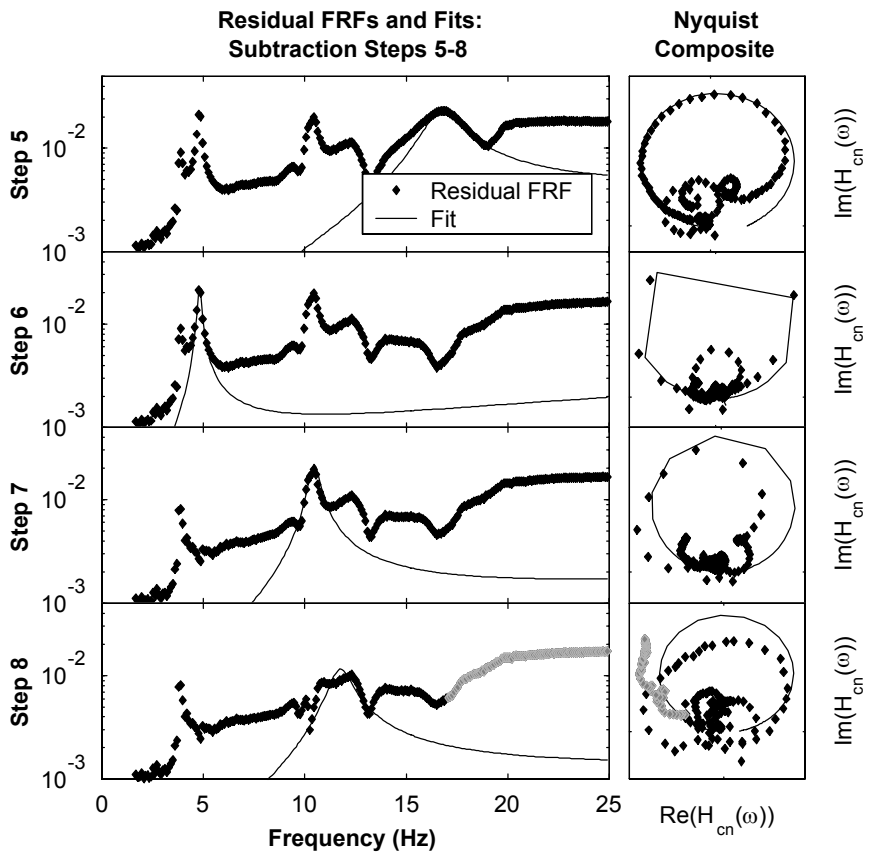

Figure 35: AMI Subtraction steps 5-8 for Z24 Bridge Data. LEFT: Composite residual FRF (.) and fit (-). RIGHT: Nyquist composite plots of residual FRF data (.) and fit (-). Data shown in gray in bottom panes was ignored in step eight.

into dominance. After step eight, peaks due to fit errors in previously identified modes become dominant in the data. Attempting a fit in any of these regions results either in a nonphysical mode ($\zeta < 0$) or a mode with an eigenvalue that is very similar to that of a previously identified mode. For this reason, subtraction was halted with eight modes identified. After mode isolation and refinement the residual, formed by subtracting the contributions of all identified modes, was searched again for evidence of any additional modes, but none were found.

AMI next proceeded to mode isolation, converging after 29 iterations. The synthesized composite FRF after mode isolation and refinement, shown in Figure 36, agrees quite well with the composite FRF of the data. Individual reconstructed FRFs also agreed well with the FRF data.

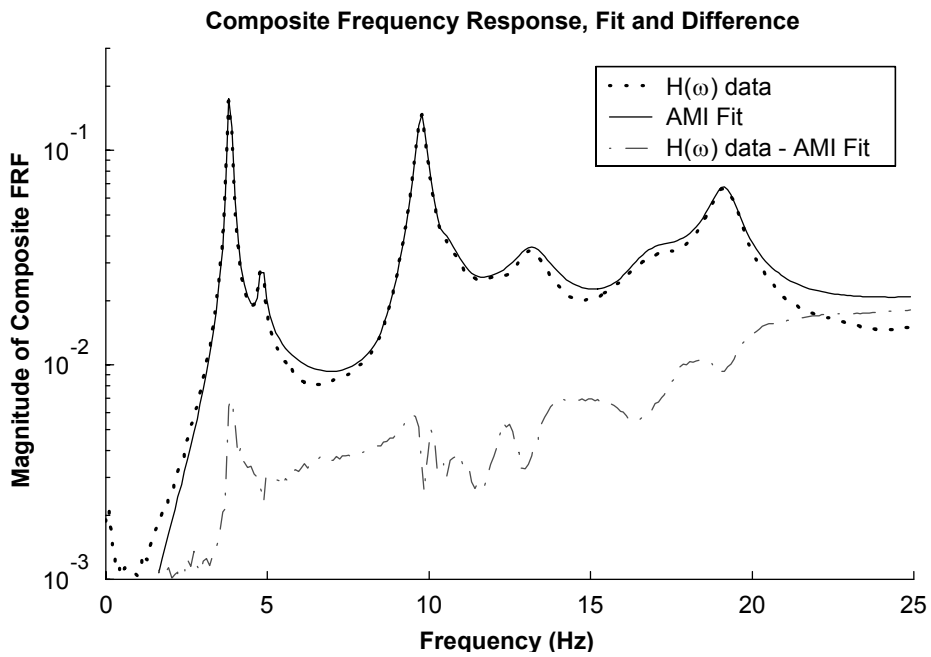

Figure 36: AMI results for Z24 bridge. Composite magnitude FRFs of data (.), AMI reconstruction (-) and the difference (-.).

Figures 34 and 35 show that during subtraction, the agreement between the residual FRFs and the synthesized FRFs is only fair for some of the identified modes. However, the composite Nyquist plot does show a circular arc indicative of a true mode, so the modes were retained. After mode isolation, composites of the synthesized FRFs for individual modes were compared to composites of the isolation residual FRFs. (The isolation residual is the data fit in the mode isolation stage, defined in eq. (34) as the original FRF data minus the contributions of all identified modes except for the mode in focus.) Before mode isolation and refinement, the Nyquist composite plots for many of the modes showed only fair agreement with their corresponding isolation residuals. These plots are not presented here, yet they were very similar to the Nyquist composite plots of the synthesized FRF and the *subtraction* residual presented in the right columns of Figures 34 and 35. After mode isolation and refinement, the agreement between the Nyquist composite of the isolation residual and the Nyquist composite of the synthesized FRF was excellent for all of the modes except for modes 4 and 5. Consequently, one would expect the modal parameters for modes 4 and 5 to be less accurate than those of the other modes. Further experimentation

Table 6: Natural frequencies for Z24 bridge drop test data from various researchers. *Values found using a peak selection factor of 0.9 and zero extra numerator terms.

	Natural Frequency (Hz), (σ Hz)				
Mode	AMI-SIMO	Marchesiello *et al* [48] SSI	Fasana [25] ARMAV	Luscher [45] FDD2	Schwarz & Richardson [70]
1	3.845	3.86 (0.01)	3.74	3.85	3.850 (0.002)
2	4.822	4.82 (0.01)	4.93	4.80	4.816 (0.027)
3	9.750	9.76 (0.05)	9.63	9.73	9.747 (0.006)
4	10.467 10.427*	10.43 (0.11)	-	-	-
5	11.616 12.188*	12.35 (0.12)	12.3	-	-
6	13.178	13.25 (0.09)	13.3	13.05	13.232 (0.196)
7	16.735	17.25 (0.31)	17.3	-	17.284
8	19.188	19.15 (0.08)	19.2	19.19	19.242 (0.019)

revealed that the quality of fit for modes 4 and 5 increased greatly if a peak selection factor of $\alpha = 0.9$ and zero extra numerator terms (see eq. (17)) were used for these modes, while using $\alpha = 0.8$ and one extra numerator term for all of the other modes. The natural frequencies and damping ratios found by AMI using $\alpha = 0.8$ and one extra numerator term for all modes are presented in Tables 6 and 7. These results represent the best results the authors could obtain using the SIMO-AMI algorithm operating in a semi-automatic fashion. The results found for modes 4 and 5 when using $\alpha = 0.9$ and zero extra numerator terms are also shown, marked with an asterix (*). These latter results are preferred as they resulted in a greatly improved fit for modes 4 and 5.

The natural frequencies and damping ratios reported by Marchesiello *et al* [48], Luscher *et al* [45], Schwarz and Richardson [71] [70] and Fasana *et al* [25] are also presented in Tables 6 and 7. Some of the aforementioned researchers presented the results of analyzing other data sets taken from the bridge, though only the results for the drop tests data are shown in Tables 6 and 7. Marchesiello *et al* processed the bridge data using an SSI algorithm very similar to that used on the frame data in Chapter 3. They processed the data globally setup by setup, so that no more than 15 responses were processed simultaneously. The natural frequencies and damping ratios shown in Tables 6 and 7 for Marchesiello *et al* are apparently the average of those obtained in nine trials. The associated standard deviation is shown

Table 7: Damping Ratios for Z24 bridge drop test data from various researchers. *Values found using a peak selection factor of 0.9 and zero extra numerator terms.

	Damping Ratio (%), (σ %)				
Mode	AMI-SIMO	Marchesiello *et al* [48] SSI	Fasana [25] ARMAV	Luscher [45] FDD2	Schwarz & Richardson [70]
1	0.923	0.9 (0.14)	1.5	0.96	0.96 (0.00)
2	1.76	1.69 (0.25)	1.8	2.76	1.21 (0.08)
3	1.68	1.54 (0.31)	2.1	1.79	1.56 (0.04)
4	2.53 2.51*	2.53 (0.86)	-	-	-
5	8.45 3.68*	3.08 (1.02)	2.2	-	-
6	4.59	3.93 (0.37)	3.2	5.24	2.34 (0.88)
7	5.65	3.94 (0.56)	2.9	-	3.95
8	2.60	2.10 (0.53)	2.8	3.15	2.25 (0.12)

in parenthesis. Fasana *et al* analyzed the data using the Ibrahim Time Domain algorithm and the Auto Regressive Moving Average Vector ARMAV algorithm. Fasana *et al* also processed the data setup by setup, though they further subdivided the data, breaking the frequency band into 2-4 segments to limit the number of modes in each analysis band. They reported that the ARMAV algorithm was preferred as it was able to identify mode 5, which was missed by the ITD algorithm. Luscher *et al* used the Frequency Domain Decomposition (FDD) algorithm and the Eigensystem Realization Algorithm (ERA) to process the drop test data, reporting that better results were obtained by the FDD algorithm. The results presented in Tables 6 and 7 for Luscher *et al* are the result of the FDD algorithm applied globally to the data from all setups, denoted the 'FDD2' results in [45]. Schwarz and Richardson applied a rational fraction polynomial curve fit to 'ODS FRFs' created from the response data to find the natural frequencies, damping ratios and mode shapes from the drop-test data. These ODS FRFs were created by combining the magnitude of the autospectrum of each sensor with the phase from the cross spectra between each sensor and a reference sensor, resulting in three sets of ODS FRFs. The set of ODS FRFs for all outputs and each reference were then curve fit independently. The natural frequencies and damping ratios in Tables 6 and 7 are the averages of those found from the three sets of ODS FRFs. The standard deviation is shown in parenthesis for all modes identified in at

least two sets of ODS FRFs.

The values found by SIMO-AMI agree well with those published by other researchers, except for mode 7, which shows some discrepancy. The natural frequency of the seventh mode identified by AMI is considerably lower than that identified by the other researchers, and the damping ratio identified by AMI for this mode is considerably higher than that found by the other researchers. Modes 4 and 5 were missed by Luscher *et al* and Schwarz and Richardson. Fasana *et al* also missed modes 4 and 5 when using the ITD algorithm, (the results of the ITD algorithm are not reproduced in Tables 6 and 7. Only the results of the ARMAV algorithm, which they preferred, are included here.) The ARMAV algorithm enabled them to identify all of the modes in Tables 6 and 7 except for mode 4. Marchesiello *et al* found a mode at 19.78 Hz, having a mode shape similar to that for mode 8, which was not identified by any of the other researchers. Both Marchesiello *et al* and Schwarz and Richardson found modes near 26 Hz, which were just outside the frequency band analyzed by AMI.

Wire-frame plots of SIMO-AMI's mode shapes are shown in Figures 37 through 44. In order to plot the mode shapes, the real displacement response in each mode was found at the instant when it is an overall maximum. This was accomplished by multiplying each mode shape $\{\psi\}$ by $e^{i\theta}$, with θ found to maximize the realness of the the product $\{\psi\}\, e^{i\theta}$, and then plotting the real part of $\{\psi\}\, e^{i\theta}$, (solid lines in Figures 37 through 44). The imaginary part of $\{\psi\}\, e^{i\theta}$ is also shown in Figures 37 through 44 by a dash-dot line. Inspection of Figures 37 through 44 reveals that the imaginary parts are generally much smaller, indicating that most of the modes had good modal phase collinearity [1]. However, one can see that the imaginary parts are quite significant for modes 4, 5 and 7. Considering that these modes are not very heavily damped, the complexity of their mode vectors is likely due to signal processing errors (i.e. leakage, etc...), or errors in the identification. Visual comparison of the mode shapes in Figures 37 through 44 with those presented by other researchers found them to be in good agreement, with the exception of modes 5 and 7 for which the agreement was fair.

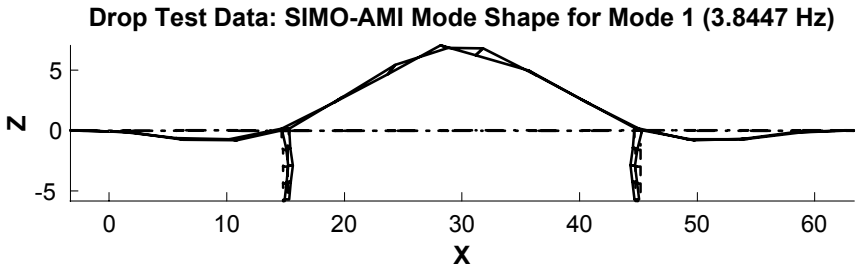

Figure 37: SIMO-AMI mode shape of Mode 1.

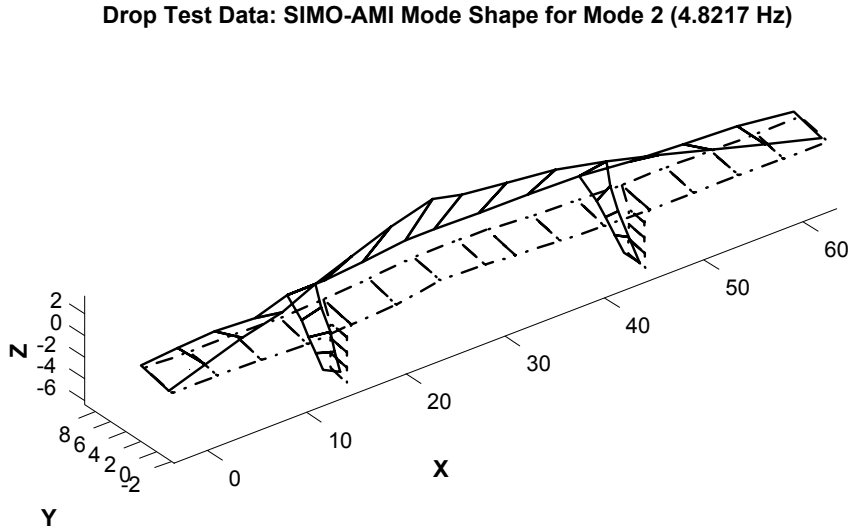

Figure 38: SIMO-AMI mode shape of Mode 2.

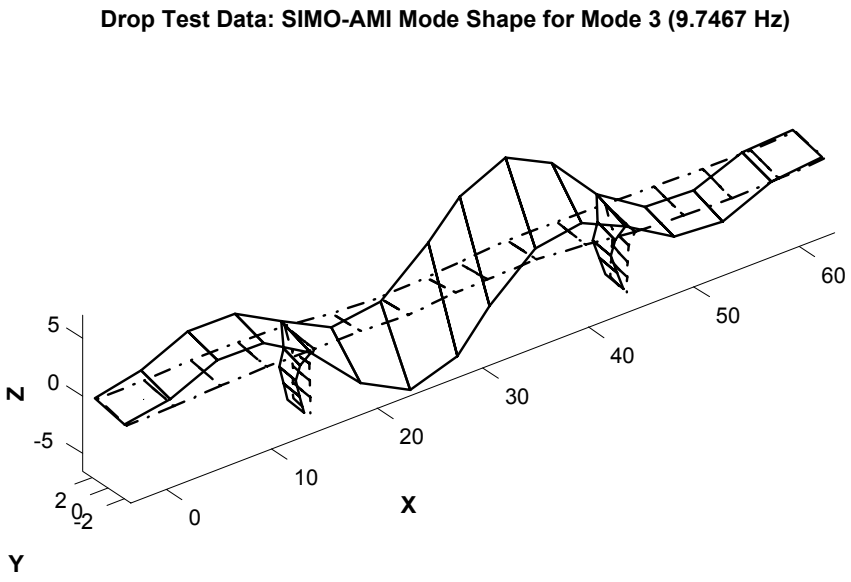

Figure 39: SIMO-AMI mode shape of Mode 3.

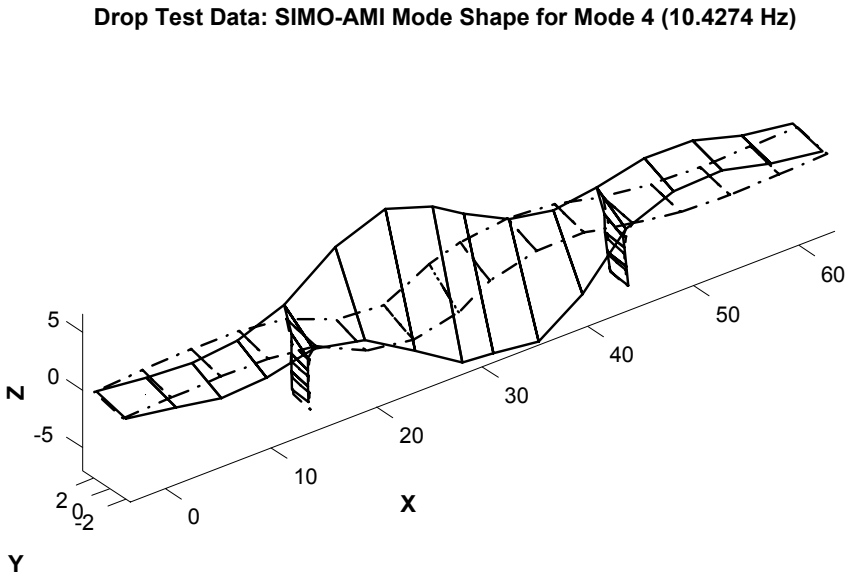

Figure 40: SIMO-AMI mode shape of Mode 4.

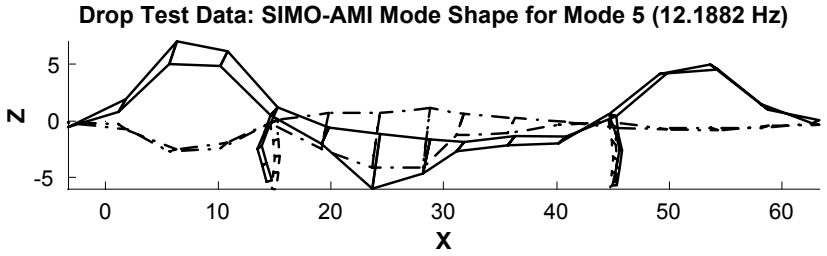

Figure 41: SIMO-AMI mode shape of Mode 5.

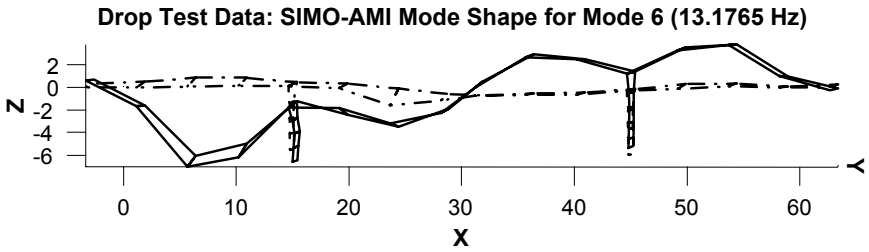

Figure 42: SIMO-AMI mode shape of Mode 6.

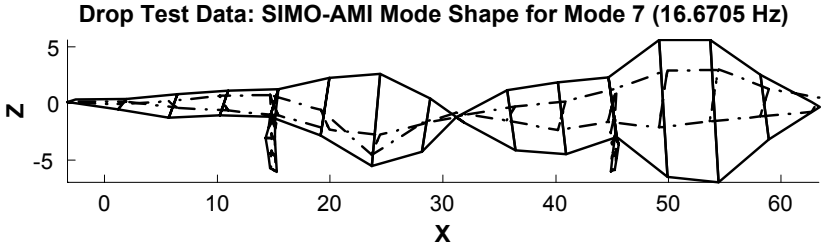

Figure 43: SIMO-AMI mode shape of Mode 7.

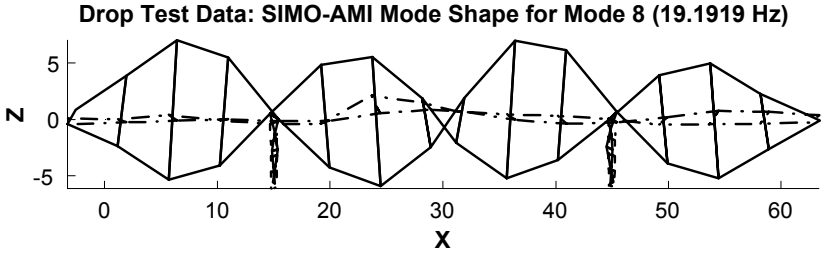

Figure 44: SIMO-AMI mode shape of Mode 8.

4.2 MIMO-AMI Applied to Shaker Excited Data

4.2.1 Data Description & Signal Processing

The Z24 bridge was also tested using two shakers driven by random noise, with one shaker located at the mid-span of the bridge and another at a side-span. Because of the size of the bridge, the response was once again measured in nine setups of up to 15 sensors each, with three response sensors and the two force sensors common to all setups. In each setup, 65,536 samples were collected for each channel with a sampling frequency of 100 Hz. The two shakers were driven with uncorrellated random noise, band-limited to 3-30 Hz. The noise sequence used to excite the bridge was optimized to minimize the crest factor of the excitation, or the ratio of the peak amplitude to RMS amplitude in the time domain [60].

The time histories of the force inputs and acceleration responses for each setup were provided by researchers from KU Leuven. It was necessary to process these time histories in order to estimate MIMO FRFs for the bridge, which could then be processed by AMI. Towards this end, the H_1 estimator was applied to the time histories [1] [60]. The data for each setup was divided into 20 blocks of length 4096 samples to which a Hanning window was applied. This resulted in an estimate of the cross spectrum matrix (between the response channels included in the setup and the two force channels) and the auto spectrum matrix (for the force channels), each at 2049 frequency lines. The number of averages used resulted in each record overlapping the previous by approximately 21%. Conforming to standard practice, the H_1 estimate of the FRF was then found by post multiplying the cross spectrum matrix with the inverse of the auto (force) spectrum matrix at each frequency line. The same procedure, as well as the windowing and averaging parameters, were used by Schwarz and Richardson [71]. Because three sensors were common to all measurement setups, nine estimates of the FRFs for these sensors were available. These were averaged resulting in an FRF data set with 75 total outputs and two inputs that was processed globally by AMI.

4.2.2 MIMO-AMI Subtraction Phase

Figure 45 describes the first subtraction step for the Hybrid MIMO-AMI algorithm. The

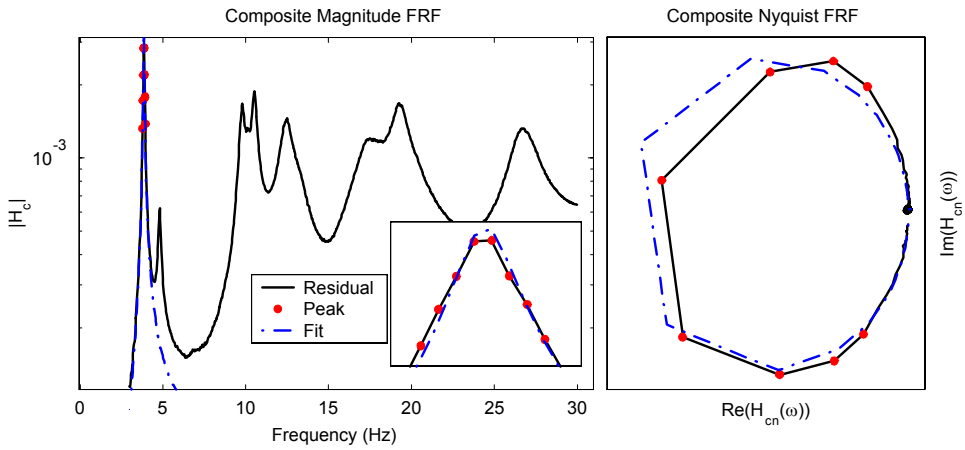

Figure 45: AMI Subtraction Step #1 (single mode fit) for Z24 data. LEFT: Composite Magnitude plots of the residual FRF data (solid) with the peak data highlighted (red dots) and the SDOF fit to the peak (dash-dot). RIGHT: Composite Nyquist plots of the residual (solid) and fit (dash-dot).

pane on the left shows the composite magnitude FRF of the Z24 data and a composite magnitude FRF of the fit to the mode found by the SDOF, common-denominator algorithm in the first subtraction step. The frequency points around the peak selected for the fit using the criteria in eq. (27) are marked with circles (red). A zoom view is also included in the lower-right corner of the pane highlighting the peak data. The pane on the right displays composite Nyquist FRFs of the data and SDOF fit, both of which were created using the rank-one residue matrix, found by SVD processing the residue matrix returned by the SDOF algorithm (see eqn. (30).)

Figure 45 shows imperfect agreement between the FRF data and the fit, suggesting that a higher order fit might be warranted. However, the second singular value ratio of the residue matrix returned by the common-denominator algorithm corresponds to $SR_2 = 0.0058$. The smallness of this value suggests that a second mode is not present at this peak, so an MDOF fit is not warranted. Experience has shown that it usually is good practice to proceed to identify modes in other frequency intervals when one encounters an uncertain situation such as this. In many cases the discrepancies between the data and the reconstructed FRF are reduced or eliminated after mode isolation. If the discrepancies persist, one can return to the uncertain frequency interval and search for additional modes after mode isolation. For

these reasons, a single mode was accepted and subtracted from the FRF data in this step. After removing the fit mode, the data within the frequency band used for finding this mode's parameters was disregarded in all subsequent subtraction steps (assigned a value of zero) to avoid returning to this location until completion of the mode subtraction phase. Note that the disregarded data is not plotted in Figures 46 through 52. After mode isolation, a search for additional modes using the full data set was performed, as described in the following subsection.

After the mode found in the first step was removed, the highest peak in the composite magnitude FRF was near 10 Hz. The peak data and resulting SDOF, common-denominator fit are shown in Figure 46. Visual inspection of the composite magnitude plot clearly

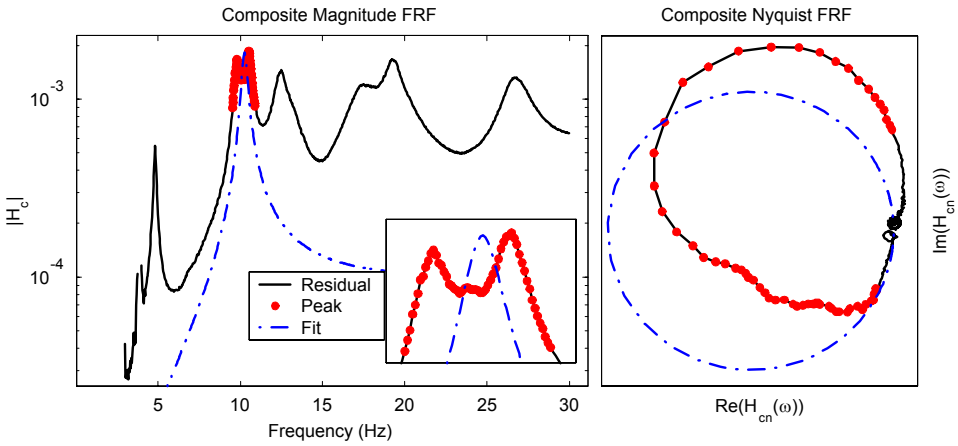

Figure 46: AMI Subtraction Step #2a (single mode fit) for Z24 data. LEFT: Composite Magnitude plots of the residual FRF data (solid) with the peak data highlighted (red dots) and the SDOF fit to the peak (dash-dot). RIGHT: Composite Nyquist plots of the residual (solid) and fit (dash-dot).

indicates the presence of at least two modes in this frequency band, which is confirmed by the second singular value ratio being $SR_2 = 0.51$. The result of attempting a two-DOF fit using the MDOF, frequency domain, SSI algorithm is illustrated in Figure 47. In analogy to Figures 45 and 46, the pane on the left shows composite magnitude FRFs of the residual data and the FRF reconstructed using both modes returned by the MDOF algorithm. On the right, two composite Nyquist plots are shown describing the quality of fit of each of the two modes identified in this step. The two modes identified in this peak data set were sorted

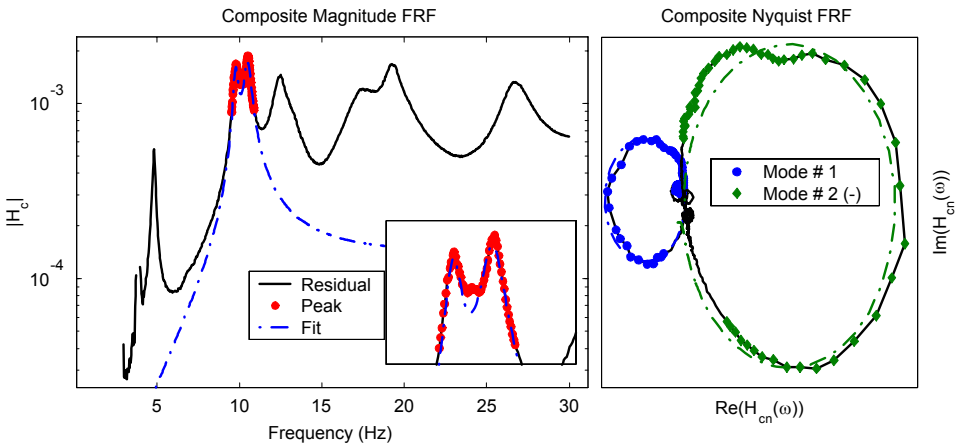

Figure 47: AMI Subtraction Step #2b (two mode fit) for Z24 data. LEFT: Composite Magnitude plots of the residual FRF data (solid) with the peak data highlighted (red dots) and the MDOF fit to the peak (dash-dot). RIGHT: Composite Nyquist plots of the isolation residual (solid) and reconstructed FRF (dash-dot) for each mode.

by ascending natural frequency and have been designated mode 1 and mode 2 in this figure. (The mode numbering in each of these figures refers solely to the modes associated with that particular subtraction step.) A Nyquist composite of the isolation residual FRF data (see eq. 34) is compared to a Nyquist composite of the FRF reconstructed for each mode, where the composite for each modal comparison is obtained using the rank-one residue matrix for that mode. Note that the Nyquist composite of the fit FRF and the isolation residual for the second mode where both multiplied by -1 prior to plotting in order to distinguish them visually from those for the first mode. When multiple modes were identified in any of the subsequent subtraction steps, the Nyquist composites for even numbered modes were multiplied by -1 for plotting purposes only. Both the magnitude composite and Nyquist composite plots in Figure 47 show good overall agreement between the data and the fit modes. However, the presence of an additional mode is suggested by the poor agreement between the two peaks in the magnitude composite plot and the irregularity of the Nyquist composite for mode 2. Only two drive points were used in collecting the FRF data, so a third singular value ratio is not available to use as an aide in determining the mode multiplicity in this frequency band. The recourse is to either disregard the differences between the data and fit, or try a three-DOF fit. The result of attempting a three-DOF

fit in the frequency band is shown in Figure 48. Modes 1 and 2 fit the residual FRF more

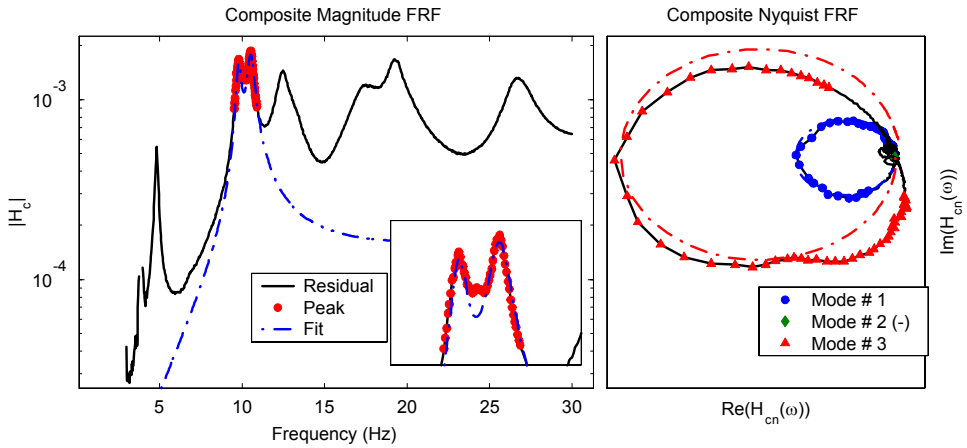

Figure 48: AMI Subtraction Step #2c (three mode fit) for Z24 data. LEFT: Composite Magnitude plots of the residual FRF data (solid) with the peak data highlighted (red dots) and the MDOF fit to the peak (dash-dot). RIGHT: Composite Nyquist plots of the isolation residual (solid) and reconstructed FRF (dash-dot) for each mode.

poorly than in Figure 47. The third identified mode has a very small damping ratio and does not contribute noticeably to the composite magnitude FRF. This mode is not visible in the composite Nyquist plot in Figure 48 because the norm of its residue matrix is much smaller than those for modes 1 and 2, though a zoom view reveals poor agreement with the data. For these reasons, the results of attempting to fit three modes to the peak were disregarded, and the two modes found using a 2-DOF fit were retained and subtracted from the data.

The third subtraction step focused on the double peak near 18 Hz. As was the case in the previous step, it was clear that at least two modes were present at this peak. The SDOF fit, for which the second singular value ratio is $SR_2 = 0.52$, is shown in Figure 49. A 2-DOF fit was attempted as shown in Figure 50. Composite Nyquist plots for the two resulting modes agree fairly well with the data, although the composite magnitude FRF shows that the second mode underestimates the data uniformly. This suggests that the second peak might be due to more than one mode. Furthermore, subtracting the fit 2-DOF FRF from the FRF data shows a residual of considerable magnitude in this region (not shown). For these reasons, three modes were fit to the peak data as shown in Figure

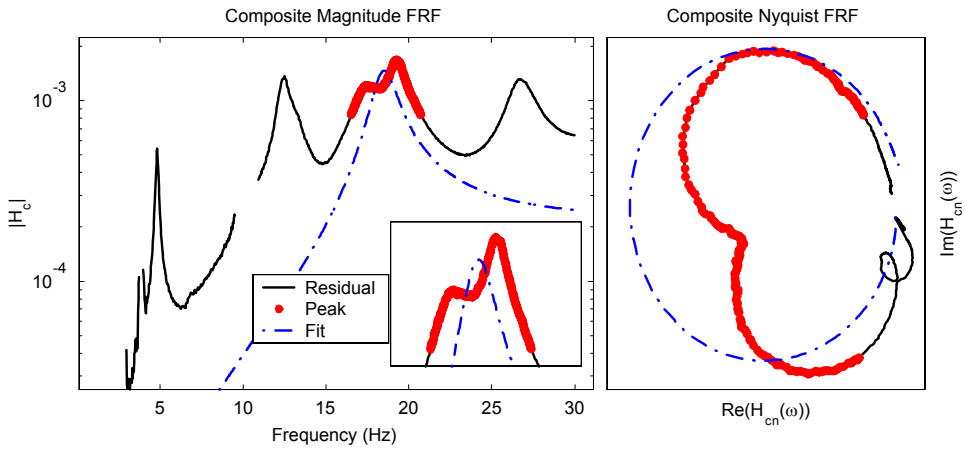

Figure 49: AMI Subtraction Step #3a (single mode fit) for Z24 data. LEFT: Composite Magnitude plots of the residual FRF data (solid) with the peak data highlighted (red dots) and the SDOF fit to the peak (dash-dot). RIGHT: Composite Nyquist plots of the residual (solid) and fit (dash-dot).

51. Two modes were identified near 19 Hz, both showing good agreement between the

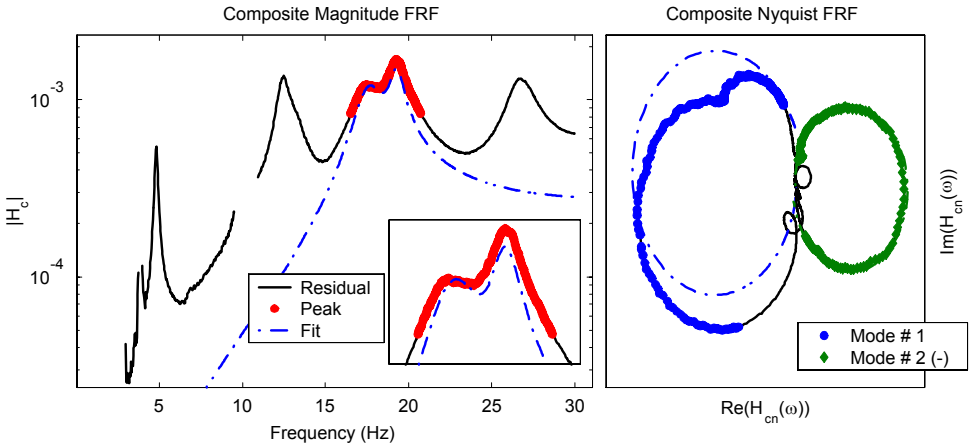

Figure 50: AMI Subtraction Step #3b (two mode fit) for Z24 data. LEFT: Composite Magnitude plots of the residual FRF data (solid) with the peak data highlighted (red dots) and the MDOF fit to the peak (dash-dot). RIGHT: Composite Nyquist plots of the isolation residual (solid) and reconstructed FRF (dash-dot) for each mode.

Nyquist composite of the data and their reconstructed FRFs. The composite magnitude FRF of the reconstruction using these three modes also shows good agreement with the data, so a higher order fit is not warranted.

The remaining peaks were processed using logic similar to that described for the first

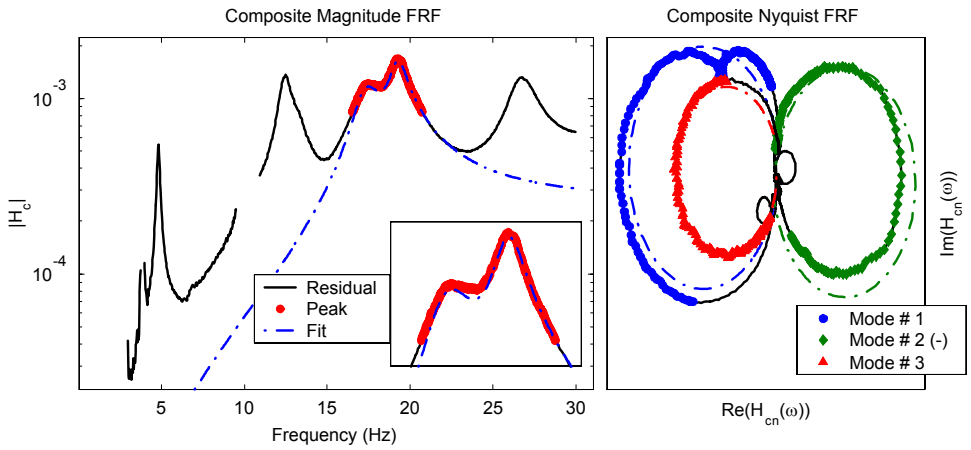

Figure 51: AMI Subtraction Step #3c (three mode fit) for Z24 data. LEFT: Composite Magnitude plots of the residual FRF data (solid) with the peak data highlighted (red dots) and the MDOF fit to the peak (dash-dot). RIGHT: Composite Nyquist plots of the isolation residual (solid) and reconstructed FRF (dash-dot) for each mode.

three subtraction steps. In steps four and five, two modes were identified at each of the peaks near 12 and 25 Hz, indicated by singular value ratios of $SR_2 = 0.085$ and 0.31 respectively. Despite the relatively small singular value ratio for the pair of modes near 12 Hz, visual inspection of the composite plots provided motivation for searching for an additional mode at this location. The sixth subtraction step is shown in Figure 52, in which an SDOF fit to the data near 5 Hz resulted in a good fit with a singular value ratio $SR_2 = 0.030$. Consequently, this mode was accepted and subtracted from the FRF data, resulting in a total of eleven modes identified. The composite magnitude FRF of the residual, formed by subtracting the contributions of these eleven modes, exhibited no peaks other than those to which previously identified modes had been fit, so the subtraction phase ended with eleven identified modes.

4.2.3 MIMO-AMI Isolation Phase

Mode isolation halted after four iterations, at which point the maximum change in any eigenvalue or any element of the residue matrices was less than 0.001%. The composite residual FRF, formed by subtracting the contributions of all identified modes, is shown in Figure 53. The maximum amplitude of the composite of the residual is almost an order of

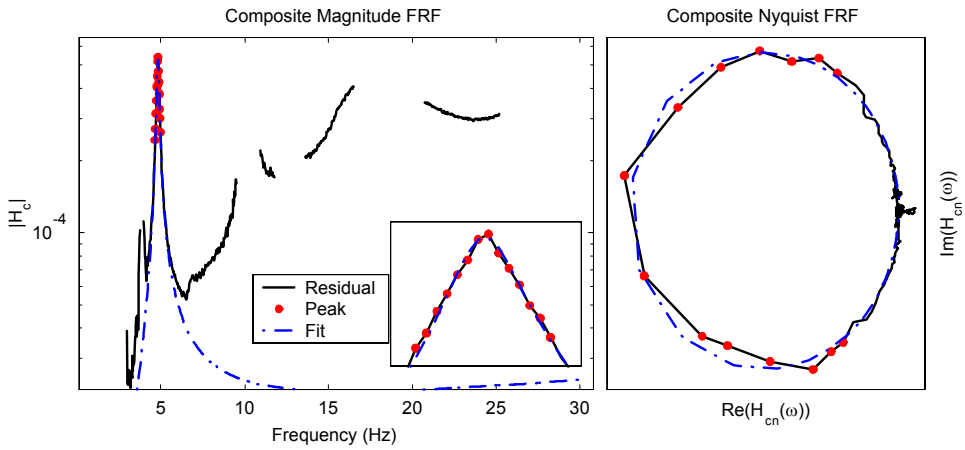

Figure 52: AMI Subtraction Step #6 (single mode fit) for Z24 data. LEFT: Composite Magnitude plots of the residual FRF data (solid) with the peak data highlighted (red dots) and the SDOF fit to the peak (dash-dot). RIGHT: Composite Nyquist plots of the residual (solid) and fit (dash-dot).

magnitude less than the composite of the original data. Small peaks remain in the vicinity

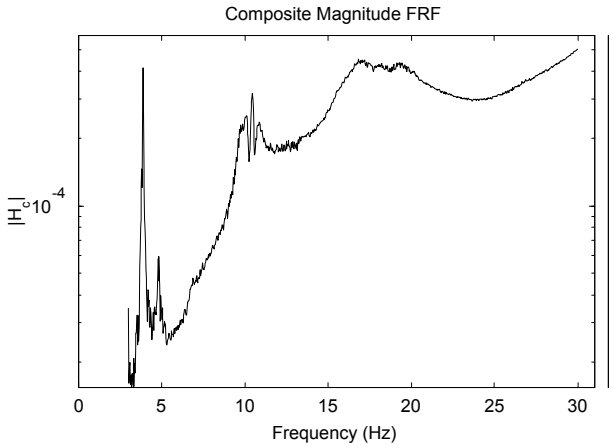

Figure 53: Magnitude composite of the residual FRF data after mode isolation.

of 4, 5, 10, and 18 Hz, each corresponding to a frequency region already processed by AMI. In general, data remaining above the noise floor in the vicinity of a previously identified modes suggests the presence of either additional modes in the frequency band or systematic errors in the data. In order to verify that no more modes could be extracted in each of these frequency bands, each was searched for additional modes by restoring the contributions of the modes previously identified in the band and then augmenting the order of the fit. An

example of this is shown in Figure 54 where four modes are fit to the peak near 18 Hz, at which three modes had been previously identified. The fourth identified mode contributes

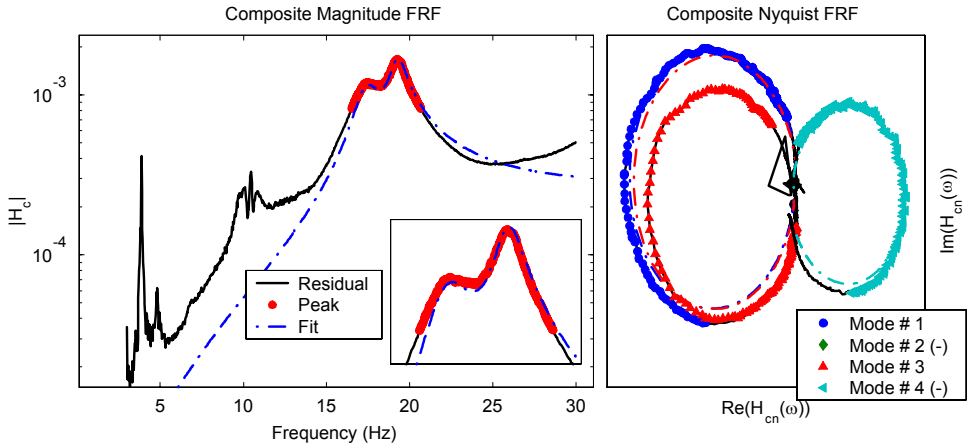

Figure 54: AMI Subtraction Step #7b (four mode fit) for Z24 data. LEFT: Composite Magnitude plots of the residual FRF data (solid) with the peak data highlighted (red dots) and the MDOF fit to the peak (dash-dot). RIGHT: Composite Nyquist plots of the isolation residual (solid) and reconstructed FRF (dash-dot) for each mode.

negligibly to the response, suggesting that only three modes are active in this frequency band. These three modes were retained, and the other peaks were then searched for more modes. Attempting a 2-DOF fit at the peak near 4 Hz even though the singular value ratio was small resulted in no better agreement than that shown in Figure 45, confirming that it was appropriate to identify a single mode in this region. No additional modes were found at any of the remaining peaks, so the subtraction process terminated with eleven modes identified.

Figure 55 shows composite Nyquist FRFs for modes 7-9 after mode isolation. Composite Nyquist plots for these modes before mode isolation were shown in the right pane of Figure 51. Comparison of Figures 55 and 51 illustrates the improvement in the agreement obtained as a result of mode isolation. The agreement in Figure 55 was typical of all of the identified modes except mode 11. Mode 11 was identified concurrently with mode 10 in the frequency band near 25 Hz. Figure 56 shows composite Nyquist plots for modes 10 and 11 after mode isolation and refinement. The scale of the plots illustrates the relative amplitude of the two modes. The contribution of mode 11 is about 20 times smaller than that of mode 10. This

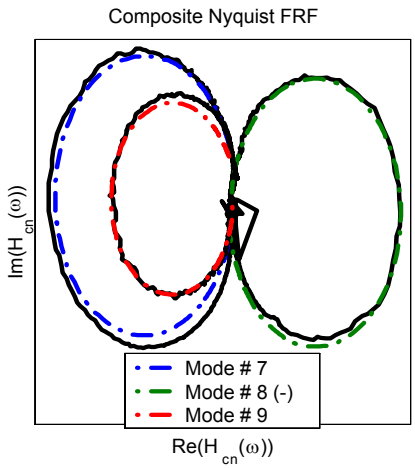

Figure 55: Composite Nyquist plots of the isolated FRFs and the reconstructed FRFs for modes 7, 8 and 9 after mode isolation and refinement.

is also evidenced by the fact that mode 11 has a smaller residue vector and larger damping ratio than mode 10. The relative unimportance of mode 11 to the response leads one to question the validity of this mode, though there were a number of reasons for retaining it. First, the singular value ratio at this peak was $SR_2 = 0.32$, suggesting that a second mode was present. (This information should be interpreted with caution, because the upward trend in the composite magnitude plot in this region suggests that out of band modes might be contributing to the rank of the FRF matrix at this location.) Second, the composite magnitude FRF of the subtraction residual showed a coherent peak in this frequency band when only one mode was subtracted. This peak was completely obliterated when two modes were accepted in the frequency band. In an alternate trial not reported here, MIMO-AMI was applied to the Z24 data for frequencies from 3 to 45 Hz. Even though the excitation to the bridge was band limited to 3-30 Hz, it was possible to extract modes from the FRFs above 30 Hz, however it was difficult to make sense of the associated mode shapes because of the coarseness of the spatial measurements. In this trial, mode 11 was identified once again, and even better agreement was found between the fit and reconstructed FRF for mode 11 once the contributions of some of the modes above 30 Hz were removed from the data set.

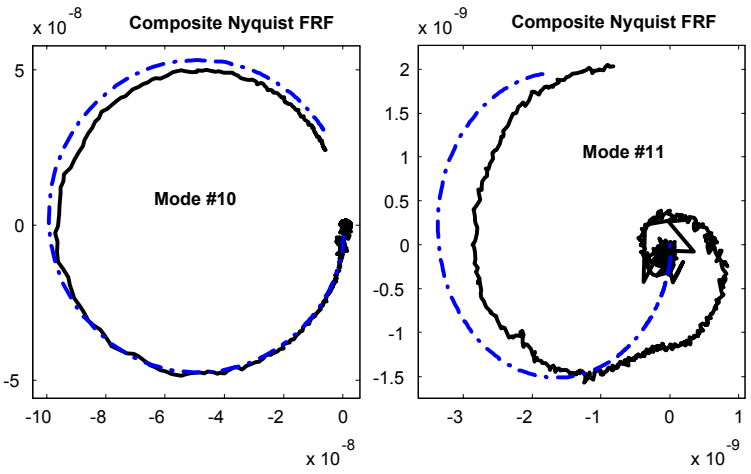

Figure 56: Composite Nyquist plots of the isolated FRFs and the reconstructed FRFs for modes 10 and 11 after mode isolation and refinement.

Figure 57 shows a composite FRF of the Z24 bridge data, a composite of AMI's reconstructed FRFs and a composite of the difference between the two. The fit agrees well with the data, with the most notable discrepancies in the previously mentioned frequency bands. The natural frequencies found by AMI after mode isolation are shown in Tables 8 and 9. The natural frequencies and damping ratios reported by Marchesiello *et al* [48], Luscher *et al* [45] and Schwarz and Richardson [70] [71] are also presented in Tables 8 and 9. Some of the aforementioned researchers presented the results of analyzing other data sets taken from the bridge, though only the results for the shaker-excited data sets are shown here. The results of the shaker and drop excited tests will be compared in Section 4.3. Marchesiello *et al* [48] processed the bridge data using a covariance driven SSI algorithm, as described in the previous section for the drop-excited tests. Luscher *et al* used the Frequency Domain Decomposition (FDD) algorithm, which also was described in the previous section. Schwarz and Richardson reported that they used a rational fraction polynomial algorithm [65] [66] to find the natural frequencies and damping ratios of the bridge, although the algorithm described in the references they cited is called the frequency domain direct system parameter identification (FDPI) algorithm by other researchers [2] [56]. They did not comment on the details of the identification, such as whether a stabilization diagram was used, or how the number of modes active in the frequency band was determined. In

Table 8: Natural frequencies for Z24 bridge drop test data from various researchers. Standard Deviations are shown in parenthesis for non-global methods.

Natural Frequency: Hz, (σ Hz)				
Mode	**MIMO-AMI**	**Marchesiello *et al* [48]**	**Luscher *et al* FDD2 [45]**	**Schwarz & Richardson [70]**
1	3.873	3.85 (0.01)	3.85	3.888
2	4.825	4.83 (0.02)	4.81	4.803
3	9.772	9.74 (0.02)	9.72	9.777
4	10.488	10.46 (0.05)	-	10.487
5	12.416	12.31 (0.07)	12.62	12.401
6	13.204	13.31 (0.17)	-	-
7	17.344	17.25 (0.18)	-	17.332
8	19.273	19.24 (0.12)	-	19.244
9	19.542	20.24 (0.16)	19.56	-
10	26.656	26.46 (0.07)	26.65	26.668
11	28.122	-	-	-

Table 9: Damping Ratios for Z24 bridge drop test data from various researchers. Standard deviation reported in parenthesis for non-global methods.

Damping Ratio: %, (σ %)				
Mode	**MIMO-AMI**	**Marchesiello *et al* [48]**	**Luscher *et al* FDD2 [45]**	**Schwarz & Richardson [70]**
1	0.9594	1.15 (0.23)	1.08	1.209
2	1.715	1.70 (0.17)	2.19	1.548
3	1.515	1.70 (0.13)	2.13	1.563
4	2.114	1.79 (0.23)	-	1.096
5	3.079	2.75 (0.89)	5.60	2.793
6	4.015	3.61 (1.25)	-	-
7	4.617	3.26 (2.48)	-	4.699
8	2.639	2.32 (0.30)	-	2.638
9	5.795	1.97 (1.24)	4.67	-
10	3.122	2.57 (0.44)	5.15	3.142
11	6.762	-	-	-

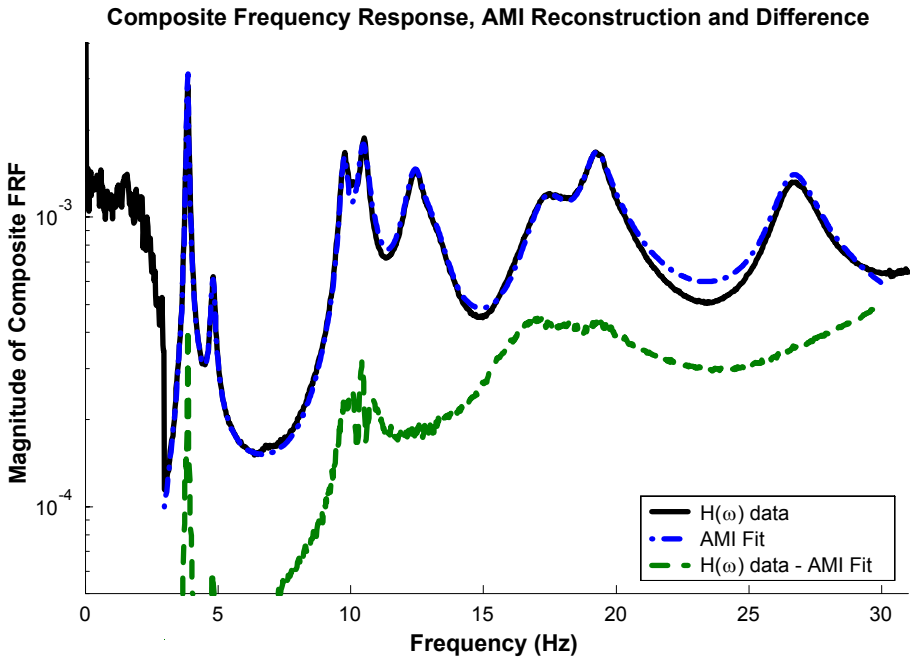

Figure 57: Magnitude composite FRFs of the Z24 data, AMI's reconstruction and the difference between the two.

a separate paper [71], Schwarz and Richardson reported identifying the sixth mode using a 'peak cursor,' however, this mode was not included in the results published in [70].

The results for most of the modes are comparable between the different groups of researchers, each of which used a different algorithm. Marchesiello *et al* found an additional mode at 7.9 Hz when processing the shaker data set. However, they attributed it to coloring of the input spectrum, so it was not included in Tables 8 and 9. Luscher *et al* failed to identify a number of modes found by the other researchers. Only AMI has identified the 11th mode, which is near the high frequency limit of the excitation spectrum.

The mode shapes are displayed in Figures 58 through 68. Complex mode vectors were obtained from AMI in accord with the state space description in eq. (7). These were plotted using the same approach described previously for the SIMO mode vectors, in which each mode shape $\{\psi\}$ was multiplied by $e^{i\theta}$, with θ found to maximize the realness of the the product $\{\psi\}\, e^{i\theta}$. The real (solid) and imaginary (dashed) parts of $\{\psi\}\, e^{i\theta}$ are shown in Figures 58 through 68. The imaginary parts were generally much smaller, indicating that most of the modes had good modal phase collinearity [1]. Modes 7, 9 and 11 were an

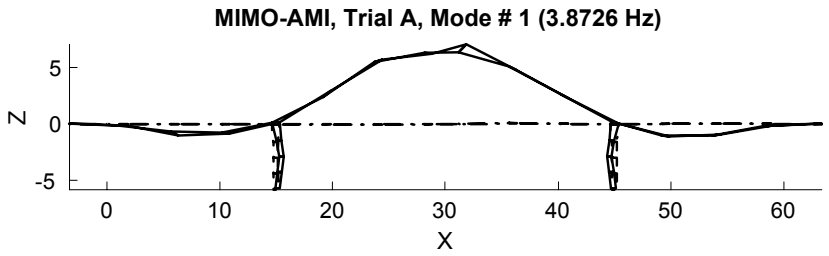

Figure 58: MIMO-AMI mode shape of Mode 1.

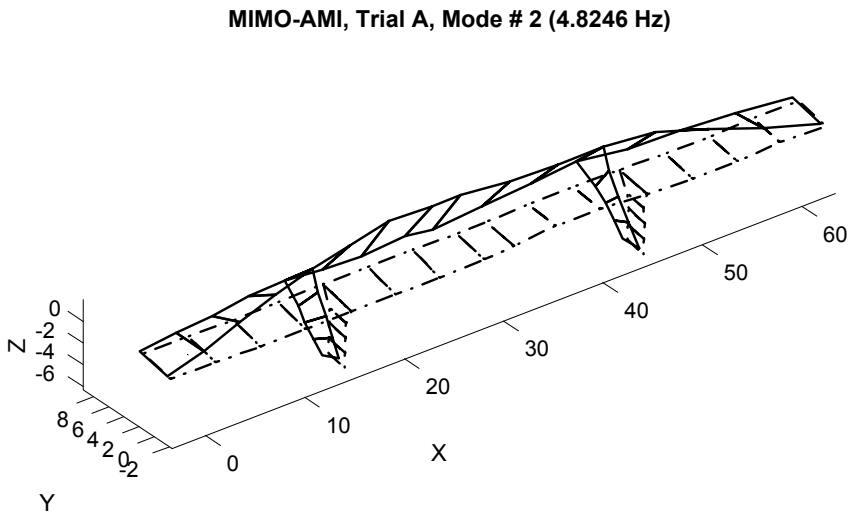

Figure 59: MIMO-AMI mode shape of Mode 2.

exception, having larger imaginary parts.

Modes 1, 5, 6, 9 and 11 consist primarily of bending of the bridge in the vertical direction. The motion of the piers and the number of half-sines along the length of the bridge both increase with mode number. Modes 3 and 4 primarily exhibit bending in the side span with torsion and bending in the main span. These modes appear very similar, yet careful inspection reveals that the two side spans have a different phase relative to the center span. Mode 2 shows coupled torsion and side-to-side sway. Modes 7, 8, and 10 are primarily torsional modes having respectively four, five and six nodes along the length of the bridge.

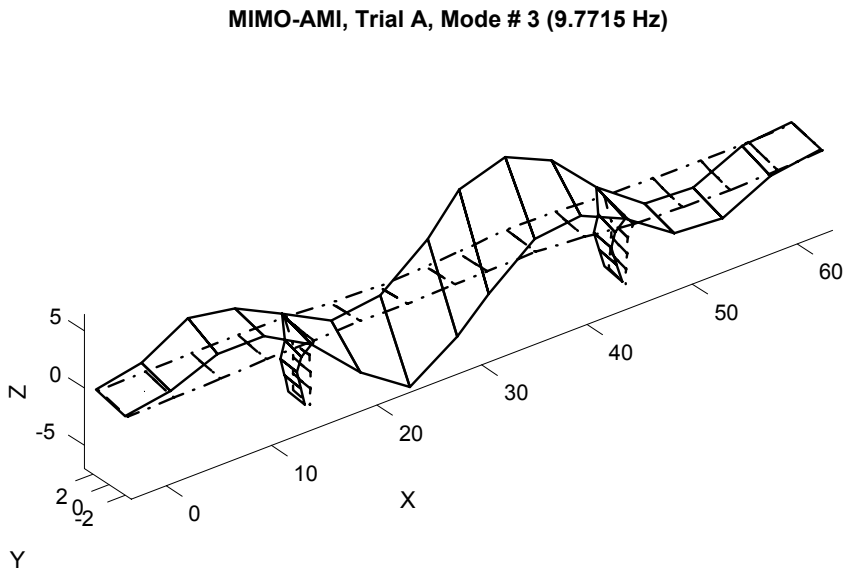

Figure 60: MIMO-AMI mode shape of Mode 3.

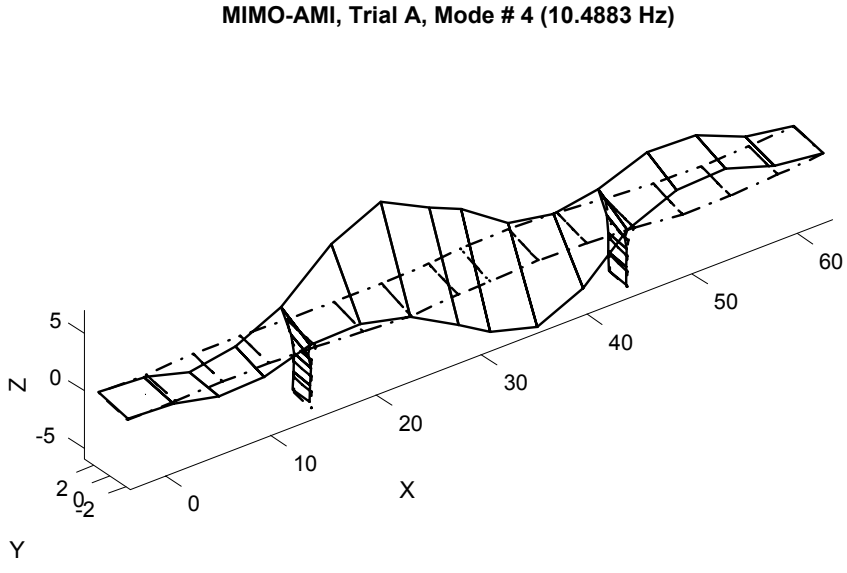

Figure 61: MIMO-AMI mode shape of Mode 4.

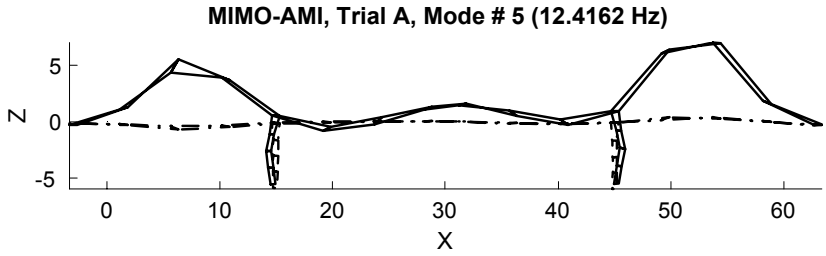

Figure 62: MIMO-AMI mode shape of Mode 5.

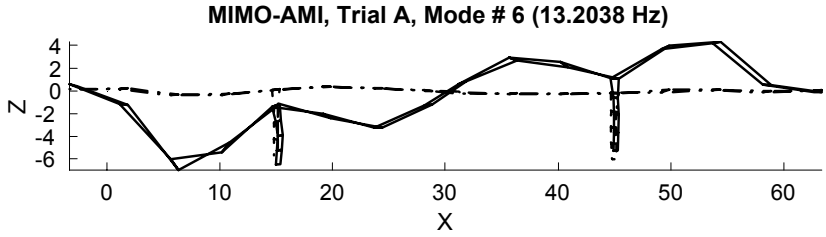

Figure 63: MIMO-AMI mode shape of Mode 6.

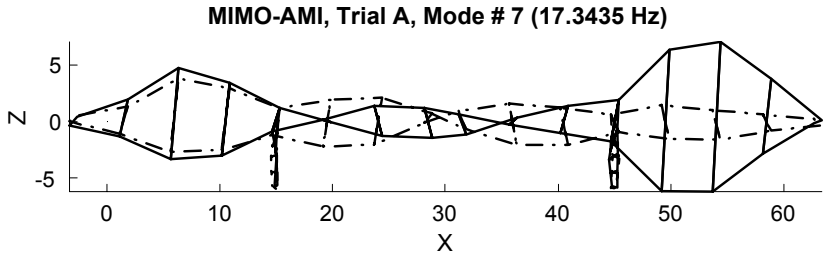

Figure 64: MIMO-AMI mode shape of Mode 7.

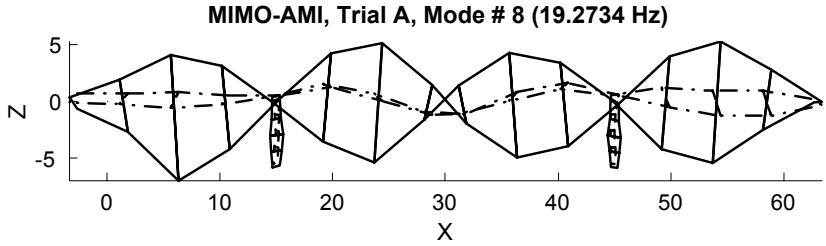

Figure 65: MIMO-AMI mode shape of Mode 8.

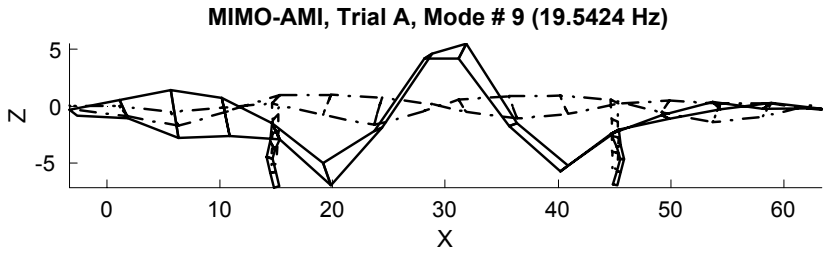

Figure 66: MIMO-AMI mode shape of Mode 9.

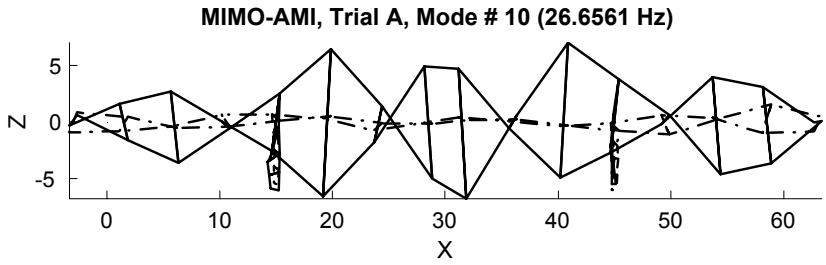

Figure 67: MIMO-AMI mode shape of Mode 10.

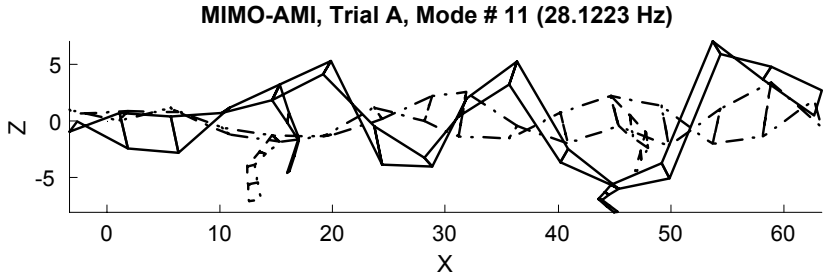

Figure 68: MIMO-AMI mode shape of Mode 11.

4.2.4 Discussion of MIMO-AMI Results

Data from the Z24 highway bridge was processed using a hybrid, MIMO implementation of the Algorithm of Mode Isolation (AMI). Modes were successively identified and subtracted from the experimental data until no additional regions were found in which a reasonable fit could be obtained. The outcome was that AMI found the lowest eleven modes of the bridge without recourse to a stabilization diagram. Particular attention was devoted to identifying modes whose natural frequencies differ by much less than their bandwidths. A metric reflecting the rank of the FRF matrix in a frequency band around a resonance peak provides a guideline for the user regarding the number of modes needed to fit that peak. In some cases, fits of increasing order were attempted, and the agreement between the data and reconstructed FRFs for the modes fit was evaluated, in order to determine the number of modes that resulted in the best results without including modes of dubious validity. The composite magnitude FRF and the composite Nyquist FRF, defined herein, were found to be extremely helpful in comparing the experimental FRFs with reconstructed FRFs for the identified modes.

The natural frequencies and mode shapes of the Z24 bridge that were identified by AMI were found to be comparable to those presented by other researchers. Several of these researchers [25], [48], [54] processed individual patches of the experimental data independently in order to limit the computational burden, resulting in an analysis that was not truly global. The AMI algorithm was able to globally process all of the FRFs of the system without requiring excessive computer resources. Furthermore, the AMI algorithm resulted in the identification of an eleventh mode at the upper frequency limit of the FRF data. Though weakly excited, a composite Nyquist plot for this mode showed good agreement. Furthermore, this mode's shape is similar to what might be expected for the next highest bending mode of the bridge based on simple theory.

In the subtraction phase of the AMI algorithm, two regions were encountered in which two peaks were clearly visible in the composite magnitude FRF. Modes 3 and 4 were identified in one of these regions, modes 7 through 9 in the other. In each case the procedure used to automatically select the frequency band surrounding a peak in the composite FRF

(described in Chapter 2, see eq. (27),) selected a band in which two close peaks were visible. As a result, the modes in each of these frequency bands were identified simultaneously using the MDOF algorithm. The modes identified at these peaks were separated by more than their average half-power bandwidths (with the exception of modes 8 and 9, whose half power bandwidths overlap,) and hence most of these modes could have been treated individually This might have been preferred because it lessens the order of the parameter identification used in each frequency band. In an alternate trial, denoted "trial B" hereafter, these modes were treated individually in the following manner. Trial and error revealed that using a peak selection parameter of 0.7 during the subtraction phase resulted in modes 3 and 4 being identified and subtracted from the data separately, and mode 7 being identified and subtracted separately from modes 8 and 9. Once the modes had been subtracted from the data, the original peak selection parameter of 0.5 was used for mode isolation. Figure 69 displays composite magnitude plots of the data, AMI's reconstruction and the difference between the two for this trial. The magnitude composite FRF of the difference between the

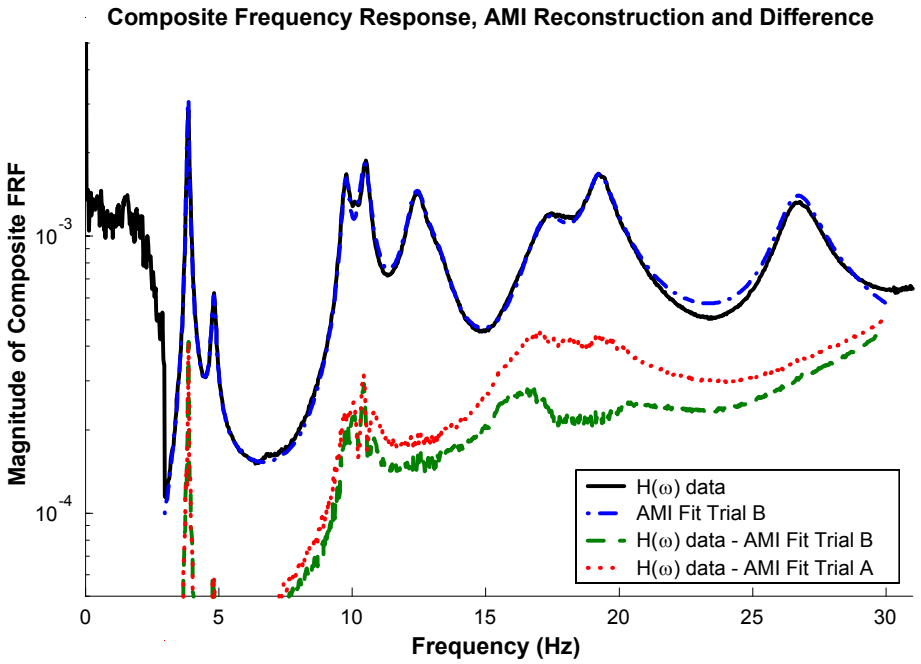

Figure 69: Magnitude composite FRFs of the Z24 data, AMI's reconstruction and the difference between the two using a modified peak selection scheme. The dotted red line shows the result using the standard approach.

data and AMI's reconstruction for the original trial (see Figure 57) is also shown, denoted "trial A." The measured and reconstructed FRFs in the vicinity of modes 7 through 9 agree more closely using the alternate approach (trial B). The seventh natural frequency and damping ratio found in trial B were 17.196 Hz and 0.0475 respectively. Only the mode shapes for the seventh and ninth modes differed significantly from those found in trial A; these are shown in Figures 70 and 71 respectively.

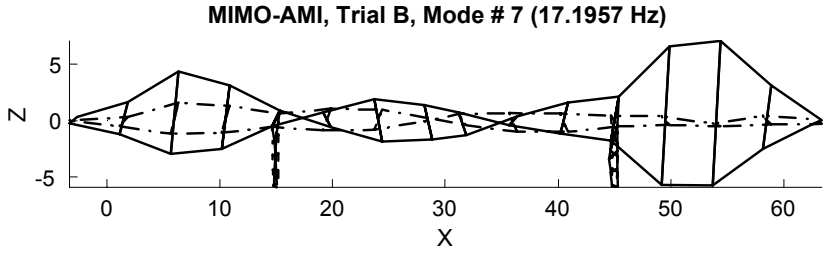

Figure 70: MIMO-AMI mode shape of Mode 7, Trial B.

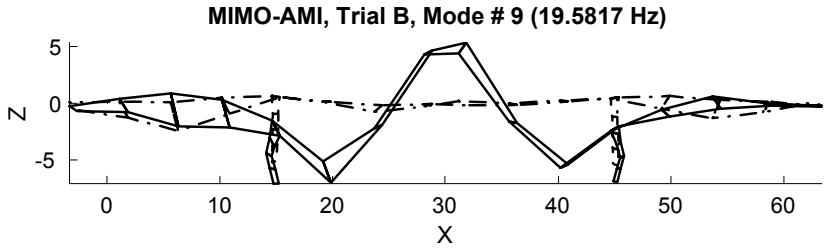

Figure 71: MIMO-AMI mode shape of Mode 9, Trial B.

Comparison with Figures 64 and 66 reveals that the mode vectors found in trial B had better modal phase collinearity, (i.e. the norm of the imaginary part of $\{\psi\}\, e^{i\theta}$ was much smaller,) however the real part of the mode shapes were visually similar to those found in trial A.

4.3 Comparison of SIMO and MIMO Results

Comparison of Tables 6 and 7 with Tables 8 and 9 reveals that similar results were obtained by AMI for the SIMO, drop excited test and the MIMO, shaker excited test. The relevant values from each of these tables have been collected in Table 10. The natural frequencies

Table 10: Comparison of SIMO- and MIMO- AMI Natural Frequencies and Damping Ratios for Z24 Bridge Data. *Values found using alternate peak selection parameters in the AMI algorithm, as described in Section 4.1.

	Natural Frequency (Hz)		Damping Ratio (%)	
Mode	**MIMO-AMI**	**SIMO-AMI**	**MIMO-AMI**	**SIMO-AMI**
1	3.8726	3.845	0.9594	0.923
2	4.8246	4.822	1.715	1.76
3	9.7715	9.750	1.515	1.68
4	10.488	10.427*	2.114	2.51*
5	12.416	12.188*	3.079	3.68*
6	13.204	13.178	4.015	4.59
7	17.344	16.735	4.617	5.65
8	19.273	19.188	2.639	2.60
9	19.542	-	5.795	-
10	26.656	-	3.122	-
11	28.122	-	6.762	-

and damping ratios for the first eight modes compare well between the two tests, with the exception of the seventh mode. SIMO-AMI was not able to identify modes 9-11 from the drop weight excited data set. This was a consequence of weak excitation of these modes in the SIMO data and the fact that a pair of heavily coupled modes near 32-35 Hz dominated the response in the vicinity of modes 10-11. These modes could not be treated using SIMO-AMI because their natural frequencies were very close relative to their half power bandwidths. The only recourse was to restrict the analysis band to exclude the modes above 25 Hz. On the other hand, MIMO-AMI was able to process the data for all excited frequencies because it uses a hybrid approach to identify groups of modes with very close natural frequencies simultaneously.

The mode vectors found from the SIMO and MIMO datasets are quite similar, as can be seen by comparing the SIMO-AMI mode vectors in Figures 37 through 44 with the MIMO-AMI mode vectors in Figures 58 through 65. However, there are some significant differences between the mode vectors, especially in their modal phase collinearity. These differences might be attributable to the process used to glue the mode vectors together, which was described in Section 4.1.1. The MAC values between the mode vectors identified by MIMO-AMI and the mode vectors identified by SIMO-AMI are shown in Table 11. Note that it was necessary to glue the SIMO-AMI mode vectors together before they could be

Table 11: MAC Matrix between MIMO and glued-SIMO mode vectors

SIMO MIMO	**1**	**2**	**3**	**4**	**5**	**6**	**7**	**8**
1	**0.99**	0.01	0.00	0.05	0.28	0.03	0.11	0.01
2	0.00	**0.97**	0.02	0.06	0.00	0.00	0.00	0.00
3	0.00	0.02	**0.98**	0.11	0.04	0.01	0.02	0.00
4	0.00	0.06	0.04	**0.87**	0.05	0.00	0.01	0.00
5	0.00	0.00	0.02	0.00	**0.48**	0.00	0.00	0.01
6	0.00	0.00	0.01	0.00	0.03	**0.94**	0.01	0.00
7	0.00	0.00	0.00	0.01	0.01	0.01	**0.50**	0.01
8	0.00	0.00	0.00	0.00	0.03	0.00	0.04	**0.93**
9	0.03	0.01	0.00	0.01	0.01	0.00	0.02	0.04
10	0.00	0.02	0.02	0.02	0.00	0.00	0.01	0.00
11	0.00	0.00	0.01	0.01	0.01	0.01	0.01	0.01

compared with the MIMO-AMI mode vectors. The MAC values indicate that the mode vectors found from the SIMO and MIMO datasets are quite similar, with most of the modes having MAC values above 0.9. The worst correlation occurs for modes 5 and 7. Both of these modes were relatively weakly excited in the SIMO dataset. A modified approach employing considerable expertise was required to extract a reasonable estimate of mode 5's parameters from the SIMO dataset, as described in Section 4.1.

Marchesiello *et al* [48] and Schwarz and Richardson [70] also presented MAC values comparing the mode vectors they obtained from the drop weight data to those obtained from the shaker data. The MAC values between each mode from the shaker test and the mode that most corresponded in the drop weight test are reproduced in Table 12. The corresponding values for AMI are also shown in Table 12. Schwarz and Richardson obtained three estimates of each mode vector when processing the drop weight data and compared each of these to the shaker mode vectors. The values shown in Table are the range of MAC values obtained for each mode. They did not report MAC values for all of the modes identified. Schwarz and Richardson also reported MAC values for an alternate trial in which they exponentially windowed the drop test data prior to processing. The range of MAC values obtained in this trial are shown in parenthesis in Table 12. AMI's MAC values are comparable to those obtained by Marchesiello *et al*, and are somewhat higher than those obtained by Schwarz and Richardson.

Table 12: MAC values between the mode vectors found in SIMO and MIMO tests for various researchers.

Mode	AMI	Marchesiello *et al* [48]	Schwarz & Richardson [70]
1	0.99	1.00	0.978-0.994 (0.977-0.994)
2	0.97	1.00	0.507-0.680 (0.749-0.910)
3	0.98	0.93	0.909-0.927 (0.911-0.946)
4	0.87	0.41	-
5	0.48	0.65	0.117-0.134 (not provided)
6	0.94	0.79	-
7	0.50	0.42	-
8	0.93	0.93	0.825-0.834 (0.839-0.904)
9	-	0.50	-
10	-	0.46	-

In [43], Kramer *et al* discuss the differences in cost and labor associated with the shaker and drop weight tests on the Z24 bridge. The shaker excited tests were estimated to cost about $503,500, compared to $168,900 for the drop weight tests. This did not include the costs of the manual labor associated with equipment setup and data collection. Kramer *et al* estimated that 20 man-days of labor were required to mobilize and demobilize the equipment for the shaker excited tests, compared to two man-days for the drop weight tests. Installation and de-installation of the shaker related equipment also took considerably longer than the drop weight equipment. Considering the relatively good results found from the drop test data, such an approach might be quite attractive in many applications. On the other hand, many more modes were identifiable from the MIMO data set, and with much greater confidence because the rank of the FRF matrix in the vicinity of each mode could be considered. Finally, one should note that the mode vectors found from the drop-excited tests could not be scaled because the input force was not measured, whereas scaled mode vectors could be found from the MIMO tests. Parloo *et al* [53] and Brinker *et al* [10] discuss schemes for determining the scaling of mode vectors found in output only modal tests by adding mass to a structure and re-testing it.

CHAPTER V

CONCLUSIONS & RECOMMENDATIONS

This thesis presented global SIMO and global, hybrid MIMO implementations of AMI. The performance of these extensions of AMI was demonstrated on analytical data, and on experimentally measured data from a highway bridge. These evaluations showed that AMI blends single-degree-of-freedom (SDOF) and multi-degree-of-freedom (MDOF) parameter identification, offering a significant alternative to conventional methods. The AMI algorithm was shown to be capable of processing large numbers of FRFs, typical of modal tests of complex structures, in a time efficient manner. In chapters 3 and 4 composite magnitude and composite Nyquist FRFs were used to aide in visualizing these large datasets, and evaluating how well the identified model matched the experimental data. Tests on noise-contaminated analytical data in Chapter 3 suggest that the accuracy of AMI rivals that of other modern algorithms. AMI was applied to experimental data in Chapter 4 and AMI's results were compared with those presented by other groups of researchers. The modal parameters found by the AMI algorithm compared favorably with those presented by other experts in experimental modal analysis, further confirming the value of the algorithm.

A number of areas for future research have been identified in the course of this work. The success of some damage detection or condition monitoring systems depends on accurately identifying a system's modal parameters, especially when small defects must be identified. Furthermore, the identification algorithm often must perform quickly and automatically to result in a practical monitoring system. For example, SIMO-AMI was applied to vibration data from computer chips in [23]. SIMO-AMI was able to identify a few of the modes of the system automatically, some of which changed significantly when the chips were damaged. In contrast, the author and Erdahl also attempted to apply the SSI algorithm [77] to the same data, yet it required excessive computational resources, and a great deal of user interaction was needed to interpret the resulting stabilization diagrams. AMI may offer

similar advantages in other damage detection or condition monitoring systems. However, it will probably be important to further enhance the robustness and automatability of the AMI algorithm for some applications.

In Chapter 4, AMI was applied to data from a highway bridge that was excited using both the conventional shaker approach, and by dropping a large mass on the bridge and recording its free response. It was noted that AMI found similar results when processing the drop-excited tests as compared to the shaker-excited tests, yet the shaker excited tests were significantly more expensive [43]. The primary drawbacks of the drop-excited tests were that some of the modes were not well excited, and hence not identified or poorly identified, and that a singular value ratio was not available to aide in detecting modes with close natural frequencies. Both of these difficulties could be remedied by simply performing the drop tests twice, exciting the structure in two different locations. This is exactly what was done in Chapter 3 for both of the analytical tests. Such an approach could yield accurate modal parameters at a fraction of the cost of conventional shaker-excited testing. Furthermore, if noisy data is encountered, the results of the exponential windowing study in Chapter 3 might be applied to reduce the effect of ambient noise.

It was noted in Chapter 4 that the mode vectors found from the drop-excited tests could not be scaled because the input force was not measured, whereas scaled mode vectors could be found from the MIMO tests. It also could be possible to obtain scaled mode vectors using an impulse test approach. For example, the input force could be measured by dropping the mass onto an instrumented pad. Another alternative would be to apply the recent sensitivity based method for scaling mode vectors (see [10] or [53] for example.) In this method, the unscaled mode vectors are obtained in a preliminary test, following which known masses are added to the structure. The shift in the structure's natural frequencies is then noted and used to compute the unknown scale factor for each mode. Parloo *et al* demonstrated the application of this method to a bridge in [53].

This work has highlighted the fact that AMI is a concept independent of the fitting algorithms used in the identification process. In some applications, other fitting algorithms might be preferred to deal with specific classes of noise or measurement errors. For example,

the Maximum Likelihood algorithm [13] [14] [35] has been shown to perform well in the presence of substantial measurement noise, when an estimate of the covariance matrix of the noise is available. Perhaps the computational efficiency of the Maximum Likelihood algorithm could be improved by applying it in SDOF form in AMI. Also, one might modify the fitting algorithms so that AMI could be applied to the spectra of the response in output-only modal analysis, or to the complex mode indicator function derived from the spectra. Applied in this way, AMI would provide a simple yet powerful extension to Frequency Domain Decomposition [1] [45] [80], which is perhaps the most commonly applied operational modal analysis algorithm.

Another extension to AMI might address the weakness of the SIMO-AMI algorithm when close modes are present. The hybrid, MIMO algorithm was shown to be effective in identifying modes with close natural frequencies, however the simple hybrid approach was not particularly effective when applied to SIMO or SISO data for systems with close natural frequencies. Perhaps a variant of the frequency domain subspace algorithm, or some other algorithm MDOF algorithm could be found which would improve the performance of SIMO-AMI on SISO or SIMO data sets. Some minor implementation issues could also be improved, such as the algorithm used to select the frequency interval around each peak used for parameter identification (see eq. (27),) or the criteria for automating the subtraction phase of AMI.

REFERENCES

[1] Allemang, R. J., *Vibrations Course Notes*. Cincinnati: http://www.sdrl.uc.edu/, 1999.

[2] Allemang, R. J. and Brown, D. L., "A unified matrix polynomial approach to modal identification," *Journal of Sound and Vibration*, vol. 211, pp. 301–322, 1998.

[3] Allen, M. S. and Ginsberg, J. H., "A linear least-squares version of the Algorithm of Mode Isolation for identifying modal properties. part II: Application and assessment," *Journal of the Acoustical Society of America (JASA)*, vol. 116, no. 2, pp. 908–915, 2004.

[4] Allen, M. S. and Ginsberg, J. H., "SIMO extension of the Algorithm of Mode Isolation," in *IMAC 22 - XXII International Modal Analysis Conference*, (Dearborn, Michigan), 2004.

[5] Allen, M. S. and Ginsberg, J. H., "Global, hybrid, MIMO implementation of the Algorithm of Mode Isolation," in *23rd International Modal Analysis Conference (IMAC XXIII)*, (Orlando, Florida), 2005.

[6] Allen, M. S. and Ginsberg, J. H., "A global, single-input-multi-output (simo) implementation of the Algorithm of Mode Isolation and applications to analytical and experimental data," *Mechanical Systems and Signal Processing*, vol. Submitted, 2005.

[7] Balmes, E., "Integration of existing methods and user knowledge in a MIMO identification algorithm for structures with high modal densities," in *11th International Modal Analysis Conference (IMAC XI)*, (Kissimmee, Florida), pp. 613–619, 1993.

[8] Balmes, E., "Frequency domain identification of structural dynamics using the pole/residue parametrization," in *International Modal Analysis Conference (IMAC)*, 1996.

[9] Brewer, J. W., "Kronecker products and matrix calculus in system theory," *IEEE Transactions on Circuits and Systems*, vol. CAS-25, no. 9, pp. 772–781, 1978.

[10] Brincker, R., Rodrigues, J., and Andersen, P., "Scaling the mode shapes of a building model by mass changes," in *22nd International Modal Analysis Conference (IMAC XXII)*, (Dearborn, Michigan), 2004.

[11] Brown, D. L. and Halvorsen, W. G., "Impulse technique for structural frequency response testing," *Sound and Vibration*, Nov. 1977, p. 21, 1977.

[12] Cafeo, J. A. and Trethewey, M. W., "Impulse test truncation and exponential window effects on spectral and modal parameters," in *8th International Modal Analysis Conference (IMAC VIII)*, (Kissimmee, Florida), pp. 234–240, 1990.

[13] Cauberghe, B., Guillame, P., Verboven, P., and Parloo, E., "Identification of modal parameters including unmeasured forces and transient effects," *Journal of Sound and Vibration*, vol. 265, pp. 609–625, 2003.

[14] Cauberghe, B., Guillame, P., Verboven, P., Parloo, E., and Vanlanduit, S., "A poly-reference implementation of the maximum likelihood complex frequency-domain estimator and some industrial applications," in *22nd International Modal Analysis Conference (IMAC XXII)*, (Dearborn, Michigan), 2004.

[15] Cauberghe, B., Guillame, P., Verboven, P., Vanlanduit, S., and Parloo, E., "On the influence of the parameter constraint on the stability of the poles and the discrimination capabilities of the stabilisation diagrams," *Mechanical Systems and Signal Processing*, in press, 2005.

[16] Chen, P.-T. and Ginsberg, J. H., "On the relationship between veering of eigenvalue loci and parameter sensitivity of eigenfunctions," *Journal of Vibration and Acoustics*, vol. 114, pp. 141–148, 1992.

[17] Clark, R. L., Wicks, A. L., and Becker, W. J., "Effects of an exponential window on the damping coefficient," in *7th International Modal Analysis Conference (IMAC VII)*, (Las Vegas, Nevada), 1989.

[18] Cock, K. D., Peeters, B., Vecchio, A., Moor, B. D., and Van Der Auweraer, H., "Subspace system identification for mechanical engineering," in *Proceedings of ISMA2002 - International Conference on Noise and Vibration Engineering*, vol. III, (Leuven, Belgium), pp. 1333–1352, 2002.

[19] Doebling, S. W., Alvin, K. F., and Peterson, L. D., "Limitations of state-space system identification algorithms for structures with high modal density," in *12th International Modal Analysis Conference (IMAC-12)*, (Honolulu, Hawaii), pp. 633–640, 1994.

[20] Drexel, M. V. and Ginsberg, J. H., "Modal parameter identification using state space mode isolation," in *19th International Modal Analysis Conference (IMAC-19)*, (Orlando, FL), 2001.

[21] Drexel, M. V. and Ginsberg, J. H., "Mode isolation: A new algorithm for modal parameter identification," *Journal of the Acoustical Society of America (JASA)*, vol. 110, no. 3, pp. 1371–1378, 2001.

[22] Drexel, M. V., Ginsberg, J. H., and Zaki, B. R., "State space implementation of the algorithm of mode isolation," *Journal of Vibration and Acoustics*, vol. 125, no. April, pp. 205–213, 2003.

[23] Erdahl, D. S., *Microelectronic Device Inspection System Implementation and Modeling for Flip Chips and Multi-Layer Chip Capacitors*. Ph.D., Georgia Institute of Technology, 2005.

[24] Ewins, D. J., *Modal Testing: Theory, Practice and Application*. Baldock, England: Research Studies Press, 2000.

[25] Fasana, A., Garibaldi, L., Giorcelli, E., and Sabia, D., "Z24 bridge dynamic data analysis by time domain methods," in *International Modal Analysis Conference (IMAC XIX)*, (Kissimmee, Florida), 2001.

[26] Fladung, W. and Rost, R., "Application and correction of the exponential window for frequency response functions," *Mechanical Systems and Signal Processing*, vol. 11, no. 1, pp. 23–36, 1997.

[27] Fladung, W. and Rost, R., "Cause and effect of applying the exponential window to an impact force signal," in *14th International Modal Analysis Conference (IMAC XIV)*, (Dearborn, Michigan), pp. 1553–1559, 1996.

[28] Formenti, D. and Richardson, M., "Parameter estimation from frequency response measurements using rational fraction polynomials (twenty years of progress)," in *20th International Modal Analysis Conference (IMAC-20)*, (Los Angeles, CA), pp. 373–382, 2002.

[29] Ginsberg, J. H., *Mechanical and Structural Vibrations*. New York: John Wiley and Sons, first ed., 2001.

[30] Ginsberg, J. H. and Allen, M. S., "Recent improvements of the algorithm of mode isolation," in *Proceedings of IMECE'03, ASME International Mechanical Engineering Congress and Exposition, NCA*, (Washington, DC), 2003.

[31] Ginsberg, J. H. and Allen, M. S., "A linear least-squares version of the Algorithm of Mode Isolation for identifying modal properties. part I: Conceptual development," *Journal of the Acoustical Society of America (JASA)*, vol. 116, no. 2, pp. 900–907, 2004.

[32] Ginsberg, J. H., Allen, M. S., Ferri, A., and Moloney, C., "A general linear least squares sdof algorithm for identifying eigenvalues and residues," in *21st International Modal Analysis Conference (IMAC-21)*, (Orlando, Florida), 2003.

[33] Goethals, I. and Moor, B. D., "Model reduction and energy analysis as a tool to detect spurious modes," in *Proceedings of ISMA2002 - International Conference on Noise and Vibration Engineering*, vol. III, (Leuven, Belgium), pp. 1307–1314, 2002.

[34] Guillame, P., Peeters, B., Cauberghe, B., and Verboven, P., "Identification of highly damped systems and its application to vibro-acoustic modeling," in *International Modal Analysis Conference (IMAC XXII)*, (Dearborne, Michigan), 2004.

[35] Guillame, P., Verboven, P., and Vanlaunduit, S., "Frequency-domain maximum likelihood identification of modal parameters with confidence intervals," in *International Seminar on Modal Analysis (ISMA-23)*, (Leuven, Belgium), 1998.

[36] Guillame, P., Verboven, P., Vanlaunduit, S., Van Der Auweraer, H., and Peeters, B., "A poly-reference implementation of the least-squares complex frequency-domain estimator," in *International Modal Analysis Conference (IMAC XXI)*, (Kissimmee, Florida), 2003.

[37] Heylen, W., Lammens, S., and Sas, P., *Modal Analysis Theory and Testing*. Leuven, Belgium: Katholieke Universiteit Leuven, 2000.

[38] Huang, C.-H. and Ma, C.-C., "Vibration of cracked circular plates at resonance frequencies," *Journal of Sound and Vibration*, vol. 236, no. 4, pp. 637–656, 2000.

[39] Hung, C. F. and Ko, W., "Identification of modal parameters from measured output data using vector backward autoregressive model," *Journal of Sound and Vibration*, vol. 256, no. 2, pp. 249–270, 2002.

[40] Joh, Y.-D. and Lee, C.-W., "Excitation methods and modal parameter identification in complex modal testing of rotating machinery," *International Journal of Analytical and Experimental Modal Analysis*, vol. 8, no. 3, pp. 179–203, 1993.

[41] Kirshenboim, J., "SIM - modal identification by simultaneous mode fitting," tech. rep., Imperial College, August 1979.

[42] Kramer, C., de Smet, C. A. M., and G., d. R., "Z24 bridge damage detection tests," in *17th International Modal Analysis Conference (IMAC XVII)*, (Kissimmee, Florida), 1999.

[43] Kramer, C., de Smet, C. A. M., and Peeters, B., "Comparison of ambient and forced vibration testing of civil engineering structures," in *17th International Modal Analysis Conference (IMAC XVII)*, (Kissimmee, Florida), 1999.

[44] Lauwagie, T., Sol, H., Heylen, W., and Roebben, G., "Determination of the in-plane elastic properties of the different layers of laminated plates by means of vibration testing and model updating," *Journal of Sound and Vibration*, vol. 274, pp. 529–546, 2004.

[45] Luscher, D. J., Brownjohn, J. M. W., Sohn, H., and Farrar, C. R., "Modal parameter extraction of Z24 bridge data," in *19th International Modal Analysis Conference*, (Kissimmee, Florida), 2001.

[46] Mahmoud, M. A., Zaid, M. A., and Harashani, S. A., "Numerical frequency analysis of uniform beams with a transverse crack," *Communications in Numerical Methods in Engineering*, vol. 15, pp. 709–715, 1999.

[47] Maia, S., Silva, J. M. M., He, J., Lieven, N. A., Lin, R. M., Skingle, G. W., To, W. M., and Urgueira, A. P. V., *Theoretical and Experimental Modal Analysis*. Taunto, Somerset, England: Research Studies Press Ltd., 1997.

[48] Marchesiello, S., Piombo, B., and Sorrentino, S., "Application of the cva-br method to the z24 bridge vibration data," in *19th International Modal Analysis Conference*, (Kissimmee, Florida), 2001.

[49] Mayes, R. L., Dorrell, L. R., and Klenke, S. E., "Applications of the automated SMAC modal parameter extraction package," in *18th International Modal Analysis Conference (IMAC XVIII)*, (San Antonio, Texas), 2000.

[50] Mayes, R. L. and Johansen, D. D., "A modal parameter extraction algorithm using best-fit reciprocal vectors," in *16th International Modal Analysis Conference (IMAC XVI)*, (Santa Barbara, California), 1998.

[51] Mayes, R. L. and Klenke, S. E., "The SMAC modal parameter extraction package," in *17th International Modal Analysis Conference*, (Kissimmee, Florida), pp. 812–818, 1999.

[52] Mayes, R. L. and Klenke, S. E., "Automation and other extensions of the SMAC modal parameter extraction package," in *18th International Modal Analysis Conference (IMAC XVIII)*, (San Antonio, Texas), 2000.

[53] Parloo, E., Cauberghe, B., Benedettini, F., Alaggio, R., and Guillame, P., "Sensitivity-based operational mode shape normalization: Application to a bridge," in *22nd International Modal Analysis Conference (IMAC XXII)*, (Dearborn, Michigan), 2004.

[54] Peeters, B., *System Identification and Damage Detection in Civil Engineering*. Ph.D., Katholeike Universiteit Leuven, 2000.

[55] Peeters, B. and De Roeck, G., "Reference based stochastic subspace identification for output-only modal analysis," *Mechanical Systems and Signal Processing*, vol. 13, no. 6, pp. 855–878, 1999.

[56] Peeters, B., Guillame, P., Van Der Auweraer, H., Cauberghe, B., Verboven, P., and Leuridan, J., "Automotive and aerospace applications of the polymax modal parameter estimation method," in *International Modal Analysis Conference (IMAC XXII)*, (Dearborne, Michigan), 2004.

[57] Peeters, B. and Roeck, G. D., "Stochastic system identification for operational modal analysis: A review," *Journal of Dynamic Systems, Measurement, and Control*, vol. 123, 2001.

[58] Pierre, C., Tang, D. M., and Dowell, E. H., "Localized vibrations of disordered multi-span beams: theory and experiment," *AIAA*, vol. 25, pp. 1249–1257, 1987.

[59] Pintelon, R., Guillame, P., Rolain, Y., Shoukens, J., and Van hamme, H., "Parametric identification of transfer functions in the frequency domain–a survey," *IEEE Transactions on Automatic Control*, vol. 39, no. 11, pp. 2245–2260, 1994.

[60] Pintelon, R. and Schoukens, J., *System Identification: a frequency domain approach*. Piscataway, NJ: IEEE Press, 2001.

[61] Press, W. H., Teukolsky, S. A., Vetterling, W. T., and Flannery, B. P., *Numerical Recipes in Fortran*. New York: Cambridge University Press, second edition ed., 1992.

[62] Qi, G. Z., Chen, H. M., Tsai, K. H., and Yang, J. C. S., "Structural dynamic model identification through neural network," in *12th International Modal Analysis Conference (IMAC XII)*, (Honolulu, Hawaii), pp. 1167–1172, 1994.

[63] Rades, M., "A comparison of some mode indicator functions," *Mechanical Systems and Signal Processing*, vol. 8, no. 4, pp. 459–474, 1994.

[64] Rades, M. and Ewins, D. J., "Mifs and macs in modal analysis," in *20th International Modal Analysis Conference (IMAC-20)*, (Los Angeles, CA), pp. 771–778, 2002.

[65] Richardson, M., "Global frequency and damping estimates from frequency response measurements," in *4th International Modal Analysis Conference (IMAC IV)*, (Los Angeles, California), 1986.

[66] Richardson, M. and Formenti, D., "Parameter estimation from frequency response measurements using rational fraction polynomials," in *1st International Modal Analysis Conference (IMAC I)*, (Orlando, Florida), 1982.

[67] Richardson, M. H. and Formenti, D. L., "Global curve fitting of frequency response measurements using the rational fraction polynomial method," in *3rd International Modal Analysis Conference*, (Orlando, Fl), pp. 390–397, SEM, 1985.

[68] Robb, D. A., "Users guide to program modent," tech. rep., Department of Mechanical Engineering, Imperial College of Science and Technology.

[69] Sanathanan, C. K. and Koerner, J., "Transfer function synthesis as a ratio of two complex polynomials," *IEEE Transactions on Automatic Control*, vol. AC-9, no. 1, pp. 56–58, 1963.

[70] Schwarz, B. and Richardson, M., "Modal parameter estimation from ambient response data," in *19th International Modal Analysis Conference (IMAC XIX)*, (Kissimmee, Florida), 2001.

[71] Schwarz, B. and Richardson, M., "Post-processing ambient and forced response bridge data to obtain modal parameters," in *19th International Modal Analysis Conference*, (Kissimmee, Florida), 2001.

[72] Taber, R. C., Brown, D. L., Vold, H., and Rocklin, G. T., "Exponential window for burst random excitation," in *3rd International Modal Analysis Conference (IMAC III)*, (Orlando, Florida), pp. 989–995, 1985.

[73] Van Der Auweraer, H., Guillame, P., Verboven, P., and Vanlaunduit, S., "Application of a fast-stabilizing frequency domain parameter estimation method," *Journal of Dynamic Systems, Measurement, and Control*, vol. 123, pp. 651–658, 2001.

[74] Van Der Auweraer, H. and Leuridan, J., "Multiple input orthogonal polynomial parameter estimation," *Mechanical Systems and Signal Processing*, vol. 1, no. 3, pp. 259–272, 1987.

[75] Van Der Auweraer, H., Leurs, W., Mas, P., and Hermans, L., "Modal parameter estimation from inconsistent data sets," in *18th International Modal Analysis Conference (IMAC-18)*, (San Antonio, Texas), pp. 763–771, 2000.

[76] Van Overschee, P. and De Moor, B., "Continuous-time frequency domain subspace system identification," *Signal Processing*, vol. 52, pp. 179–194, 1996.

[77] Van Overschee, P. and De Moor, B., *Subspace Identification for Linear Systems: Theory-Implementation-Applications*. Boston: Kluwer Academic Publishers, 1996.

[78] Verboven, P., Guillaume, P., Parloo, E., and Overmeire, M. V., "Autonomous structural health monitoring–part 1:modal parameter estimation and tracking," *Mechanical Systems and Signal Processing*, vol. 16, no. 4, pp. 637–657, 2002.

[79] Verboven, P., Parloo, E., Guillaume, P., and Overmeire, M. V., "Autonomous modal parameter estimation based on a statistical frequency domain maximum likelihood approach," in *19th International Modal Analysis Conference (IMAC-19)*, (Kissimmee, Florida), pp. 1511–1517, 2001.

[80] Womack, K. and Hodson, J., "System identification of the z24 swiss bridge," in *19th International Modal Analysis Conference*, (Kissimmee, Florida), 2001.

[81] Yin, H. and Duhamel, D., "Subtraction technique and finite difference formulas for modal parameter estimation," *Mechanical Systems and Signal Processing*, vol. 18, p. 1497Ű1503, 2004.

[82] Zaki, B. R., *A Modified Approach to Improve the Robustness of the Algorithm of Mode Isolation*. Masters, Georgia Institute of Technology, 2002.

VITA

Matthew Scott Allen was born in Provo, Utah in the United States of America on September 11, 1976. His parents, Ruel Jay Allen and Marilyn Dorothy Stone have five children, of which Matt is the third. The Allen family moved to Stockton, California in 1980, where Matt was raised and attended high school. Following high school, Matt attended Brigham Young University where he majored in Mechanical Engineering. After his first year at BYU, Matt took two years off of school to serve a mission for the Church of Jesus Christ of Latter-day Saints. Matt was called to serve in Guatemala, and lived in Guatemala City for all but eight months of his mission, the rest of which was spent in small cities to the north-east of the Capital. Upon returning, Matt finished his undergraduate degree in Mechanical Engineering at Brigham Young University and then went on to study at the Georgia Institute of Technology. On June 17, 1999 Matt married Melissa Spencer in Salt Lake City, Utah. Their first child, Andrew Ruel Allen was born on November 18, 2000 followed by Ivy Victoria Allen on May 5, 2003.